UNIVERSITY OF ROCHESTER
LABORATORY FOR LASER ENERGETICS

Volume 151
April–June 2017
DOE/NA/1944-1347

LLE Review

Quarterly Report

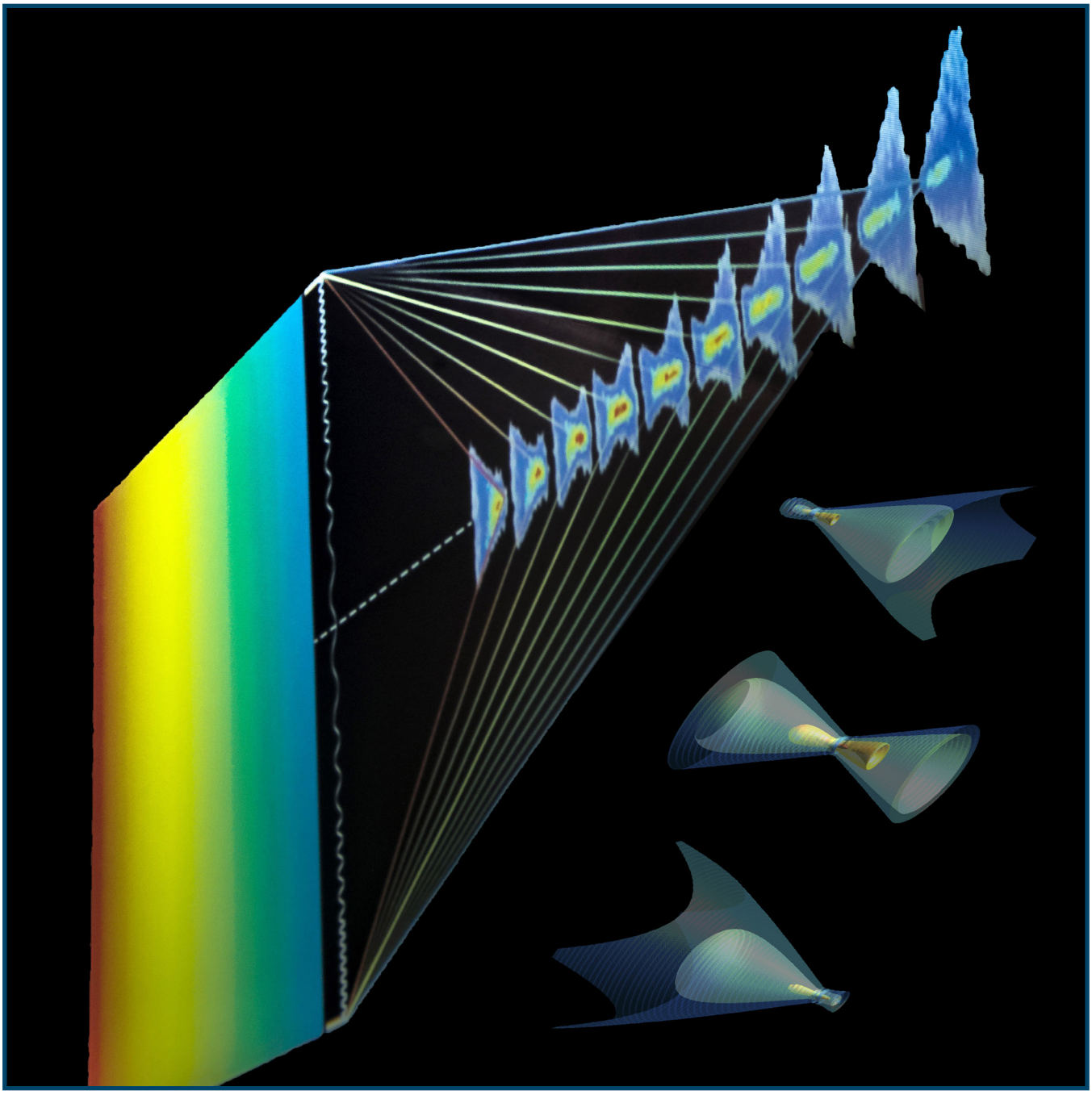

About the Cover:

The cover photo shows a schematic of the chromatic focusing system coupled to a spectrally chirped laser pulse used to generate the "flying focus," which is presented in the lead article (p. 115). Measurements of the temporal evolution of the intensity at various longitudinal locations along the focus are shown. Calculations of the flying focus using the Fresnel equation for the corresponding measurements were used to plot intensity isocontours. Evolution of the focal spot is shown here with the light propagating from left to right. Each image is separated by 10 ps. The top image represents the laser beam first reaching focus at the right edge of the system. The gray line connects the point of maximum intensity on each image, which demonstrates the counter-propagating focus moving at 1/3 the speed of light. The spatiotemporal control enabled by the flying focus is currently being investigated at LLE and could be the enabling technology for several laser-plasma devices.

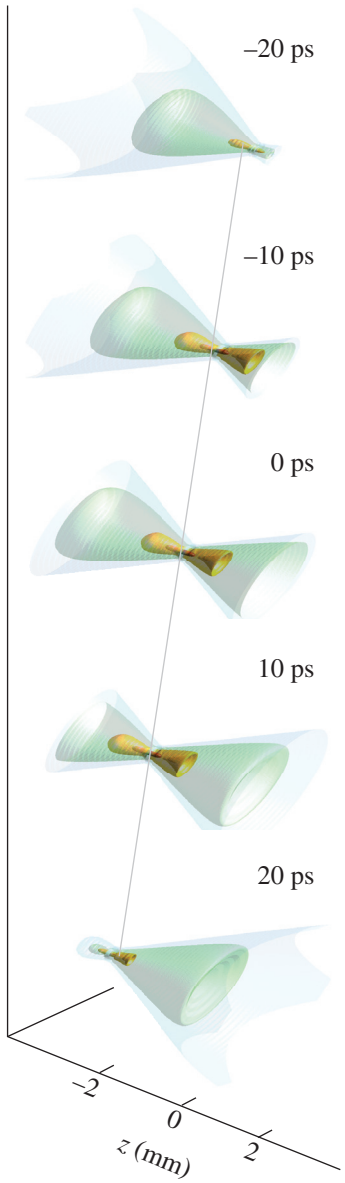

This report was prepared as an account of work conducted by the Laboratory for Laser Energetics and sponsored by New York State Energy Research and Development Authority, the University of Rochester, the U.S. Department of Energy, and other agencies. Neither the above named sponsors nor any of their employees makes any warranty, expressed or implied, or assumes any legal liability or responsibility for the accuracy, completeness, or usefulness of any information, apparatus, product, or process disclosed, or represents that its use would not infringe privately owned rights. Reference herein to any specific commercial product, process, or service by trade name, mark, manufacturer, or otherwise, does not necessarily constitute or imply its endorsement, recommendation, or favoring by the United States Government or any agency thereof or any other sponsor. Results reported in the LLE Review should not be taken as necessarily final results as they represent active research. The views and opinions of authors expressed herein do not necessarily state or reflect those of any of the above sponsoring entities.

The work described in this volume includes current research at the Laboratory for Laser Energetics, which is supported by New York State Energy Research and Development Authority, the University of Rochester, the U.S. Department of Energy Office of Inertial Confinement Fusion under Cooperative Agreement No. DE-NA0001944, and other agencies.

For questions or comments, contact Richard W. Kidder, Editor, Laboratory for Laser Energetics, 250 East River Road, Rochester, NY 14623-1299, (585) 275-7730.

Printed in the United States of America
Available from
National Technical Information Services
U.S. Department of Commerce
5285 Port Royal Road
Springfield, VA 22161
www.ntis.gov

Worldwide-Web Home Page: http://www.lle.rochester.edu/

UNIVERSITY OF ROCHESTER
LABORATORY FOR LASER ENERGETICS

Volume 151
April–June 2017
DE/NA/1944-1347

LLE Review

Quarterly Report

UR LLE

Contents

In Brief

This volume of the LLE Review, covering April–June 2017, features "Flying Focus: Spatiotemporal Control of the Laser Focus" by D. H. Froula, D. Turnbull, A. Davies, T. J. Kessler, D. Haberberger, S.-W. Bahk, I. A. Begishev, R. Boni, S. Bucht, J. Katz, J. L. Shaw, and J. Palastro. The article (p. 115) presents an avenue for novel control over laser–plasma interactions that removes the need for long-focal-length systems or guiding structures to maintain high intensities over long distances, and decouples the velocity of the focal spot from the group velocity of the light. This advanced focusing scheme called a "flying focus" enables a small-diameter laser focus to propagate nearly 100× its Rayleigh length. Providing unprecedented spatiotemporal control over the laser focal volume allows the laser focus to co- or counter-propagate along its axis at any velocity.

Additional highlights of recent research presented in this issue include the following:

- D. Turnbull, T. J. Kessler, D. Haberberger, J. L. Shaw, A. Davies, S. Bucht, and D. H. Froula propose a new laser-amplifier scheme utilizing stimulated Raman scattering in plasma in conjunction with a "flying focus"—a chromatic focusing system combined with a chirped pump beam that provides spatiotemporal control over the pump focal spot (p. 122). Simulations show that this enables optimization of the plasma temperature and mitigates many of the issues that are known to have impacted previous Raman amplification experiments, in particular the growth of precursors.

- R. K. Follett, D. H. Edgell, D. H. Froula, V. N. Goncharov, I. V. Igumenshchev, J. G. Shaw, and J. F. Myatt compared the impact of beam speckle and polarization smoothing on cross-beam energy transfer (CBET) using the 3-D wave-based laser–plasma interaction code *LPSE* and ray-based models (p. 128). The results indicate that ray-based models underpredict CBET when the assumption of spatially averaged longitudinal incoherence across the CBET interaction region is violated. A model for CBET between linearly polarized speckled beams is presented that uses ray tracing to solve for the real speckle pattern of the unperturbed laser beams within the eikonal approximation that gives excellent agreement with wave-based calculations, which suggest that the impact of beam speckle on laser absorption calculations in inertial confinement fusion implosions is small (<1%).

- M. J. Rosenberg, A. A. Solodov, J. F. Myatt, W. Seka, R. W. Short, R. Epstein, S. P. Regan, and E. M. Campbell (LLE); P. Michel, M. Hohenberger, T. Chapman, C. Goyon, J. E. Ralph, M. A. Barrios, and J. D. Moody (LLNL); and J. W. Bates (NRL) report that planar laser–plasma interaction (LPI) experiments at the National Ignition Facility (NIF) have for the first time allowed access to the regimes of electron density scale length (500 to 700 μm), electron temperature (3 to 5 keV), and laser intensity (6 to 16 $\times$ 10^{14} W/cm^2) that are relevant to direct-drive inertial confinement fusion ignition (p. 140). Scattered-light data on the NIF show that the near-quarter-critical LPI physics is dominated by stimulated Raman scattering rather than by two-plasmon decay. These results have significant implications for the mitigation of LPI hot-electron preheat in direct-drive–ignition designs.

- W. Grimble, F. J. Marshall, and E. Lambrides demonstrate an effective method for determining the offsets of the cryogenic implosion cores generated in OMEGA's inertial confinement fusion experiments (p. 146). The method utilizes images taken by the gated microscopic x-ray imaging diagnostic module. The cryogenic shot images are cross correlated onto images of their respective pulse-shape setup shot images. A true offset is then determined to be the average of the offsets calculated in the images, with the difference between those offsets being taken as the error. Initial offset results using this method indicate that the determined core offsets follow the core offsets at t_0 with some scatter.

- D. T. Michel, I. V. Igumenshchev, A. K. Davis, D. H. Edgell, D. H. Froula, D. W. Jacobs-Perkins, V. N. Goncharov, S. P. Regan, A. Shvydky, and E. M. Campbell investigate tomographic x-ray images of targets imploded in the direct-drive configuration on the 60-beam OMEGA laser to measure their 3-D drive asymmetry in target modes $\ell = 1$, 2, and 3 at a convergence ratio of ~3 (p. 152). Laser configurations were varied linearly with the corresponding modes. This made it possible to use the linear evolutions to determine the residual target mode amplitudes that remain when the laser beam energies are balanced and the laser mode amplitude compensations are obtained. The analysis provides a means to determine the residual target modes and the laser modes that compensate them that agree with 3-D simulations, which predicts significant enhancements in fusion performance.

- M. D. Wittman, M. J. Bonino, D. H. Edgell, C. Fella, and D. R. Harding discuss thermal contractions anomalies seen in glow-discharge polymer (GDP) capsules with a layer of an equimolar mixture of deuterium and tritium (DT) on their interior, compared to GDP with only deuterium and polystyrene capsules permeated with only DT (p. 159). Thermal contraction of the GDP-mixture capsules from cooling do not exhibit expected contraction and retain their room-temperature diameter after cooling. It is speculated that the highly cross-linked GDP shell is under compressive stress after fabrication and experiences bond breakage when exposed to high-density DT during permeation and some of this compressive stress is relieved during bond cleavage, causing the capsule's wall to swell, which counteracts contraction during cooling.

Richard W. Kidder
Editor

Flying Focus: Spatiotemporal Control of the Laser Focus

Introduction

The controlled coupling of a laser to a plasma has the potential to address grand scientific challenges including reaching the Schwinger limit,[1] developing compact free-electron lasers,[2] extending colliders to TeV energies,[3–5] and generating novel light sources.[6] Currently, many such applications have limited flexibility and poor control over the laser focal volume. In conventional near-diffraction–limited systems, both the minimum focal-spot size ($w_0 \simeq f^{\#}\lambda$) and longitudinal focusing range ($Z_R \simeq f^{\#2}\lambda$) are linked by the ratio of the focal length to twice the beam radius ($f^{\#} = f/2R$). As a result, these systems require large laser spots to extend their focusing range or waveguides[7–11] to maintain small spots over long distances. At low energies, manipulation of the spatial phase overcame this limitation,[12,13] but a long focal range introduced in this way does not possess dynamic properties. Pulse-front tilt was recently used to introduce a time-dependent rotation of the local wavefront in a scheme called "attosecond lighthouse,"[14] but it lacked the long longitudinal focusing range.

"Flying focus" is an advanced focusing scheme, where a chromatic focusing system combined with chirped laser pulses enables a small-diameter laser focus to propagate nearly 100× its Rayleigh length while decoupling the speed at which the peak intensity propagates from its group velocity. This unprecedented spatiotemporal control over the laser's focal volume allows the laser focus to co- or counter-propagate along its axis at any velocity. Experiments validating the concept measured subluminal (–0.09c) to superluminal (39c) focal-spot velocities, generating a nearly constant peak intensity over 4.5 mm. The flying focus allows simple, compact systems to exert novel control over laser–plasma interactions and presents opportunities to overcome current fundamental limitations in laser-plasma amplifiers,[15–18] laser-wakefield accelerators,[19–22] photon accelerators,[23] and high-order frequency conversion.[24,25]

Figure 151.1 shows a schematic of the configuration that generates a flying focus. A diffractive lens with a radially varying groove density $G = r/(\lambda_0 f_0)$ is used to produce a chromatic focus, where f_0 is the focal length of the system at the central wavelength λ_0 and r is the distance from the optical axis. With this lens, the longest wavelength (λ_r) focuses a length $L \simeq f_0(\Delta\lambda/\lambda_0)$ before the shortest wavelength ($\lambda_b = \lambda_r - \Delta\lambda$). By introducing a laser pulse with a temporally varying wavelength, the focus will move at a velocity given by $v(z) = \mathrm{d}z/\mathrm{d}t$, where d$z$ is the distance between two focused colors spectrally separated

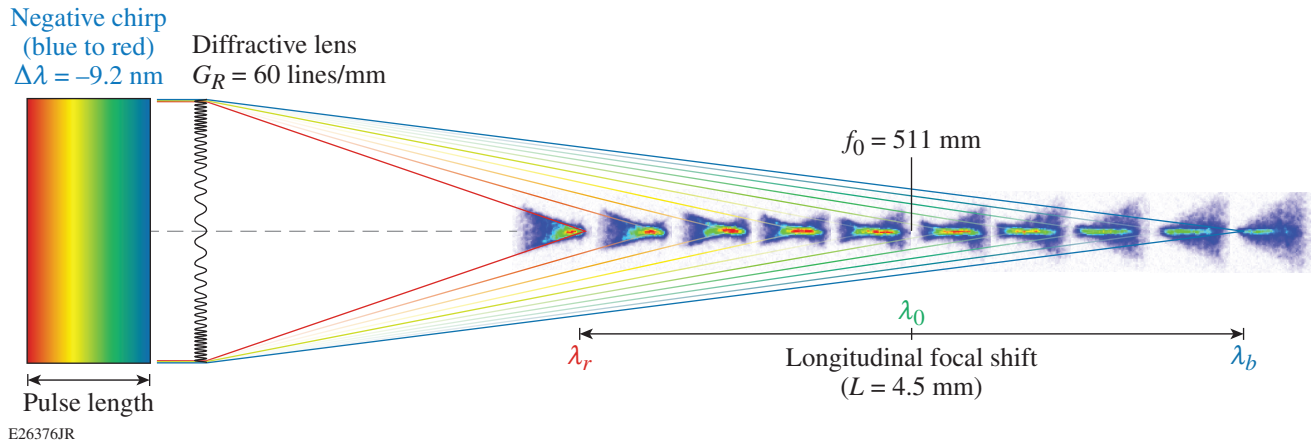

Figure 151.1
A schematic of the chromatic focusing system coupled to a spectrally chirped laser pulse. Measurements of the temporal evolution of the intensity at various longitudinal locations along the focus are shown. A negatively chirped pulse is shown where the colors change in time from blue to red.

by $\delta\lambda$; $dt = d\tau + dz/c$ is the time it takes for the two colors to reach their respective foci; $d\tau$ is the time between the two colors ($\delta\lambda$) within the chirped laser pulse, and c is the speed of light. By changing the chirp of the laser beam, the time to reach focus for successive colors is varied to provide control of the focal velocity. In general, the velocity of the focus is given by

$$v(z)/c = \left[1 + \left(\frac{d\lambda}{d\tau}\right)^{-1}\left(\frac{dz}{d\lambda}\right)^{-1}\frac{1}{c}\right]^{-1}, \quad (1)$$

where $dz/d\lambda \simeq -f_0/\lambda_0$ is the longitudinal dispersion provided by the diffractive lens and $\tau = t - z/c$. For a desired longitudinal focal-spot trajectory $z(t)$, a laser chirp can be designed:

$$\lambda(\tau)/\lambda_0 = \left[1 - z(\tau)/f_0\right]^{-1} \approx \frac{z_0(\tau)}{f_0}. \quad (2)$$

For a trajectory with a constant velocity $z(t) = v_0 t$, a linear chirp is required: $\lambda(\tau) = \left(v_0\lambda_0/f_0\right)\tau + \lambda_{r,b}$, where $v_0 = L/T$, $\lambda_{r,b}$ is the initial wavelength, T is the chirped-pulse duration, and $|\tau| < T/2$.

Figure 151.2 shows the velocity of the flying focus [Eq. (1)] for a linearly chirped laser beam ($d\lambda/d\tau = \Delta\lambda/T$). When the wavelengths are arranged in time where the longest wavelength comes first (positive chirp), the focal spot propagates in the forward direction (i.e., away from the diffractive lens) at subliminal velocities. For a negatively chirped laser beam (i.e., when the shortest wavelength comes first), any focal-spot velocity is available. When the pulse duration of the laser is equal to the transit time of the light to propagate across the focal region ($T = L/c$), all of the colors focus simultaneously, generating a long line focus; from Eq. (1) this corresponds to an "infinite" focal velocity.

This article presents experiments that demonstrate the flying focus by measuring the temporal evolution of the focal-spot intensity at various longitudinal locations. From these measurements, the velocity of the focal spot was determined and compared with the theory. The following sections (1) describe the experimental setup where LLE's Multi-Terawatt (MTW) laser[26] was used to demonstrate the flying-focus concept; (2) present the main results where the laser pulse duration was varied to demonstrate unprecedented control of the focal volume; and (3) discuss the potential applications for the flying focus. In particular, we explore using the flying focus to accelerate an ionization wave at the group velocity of accelerating photons,

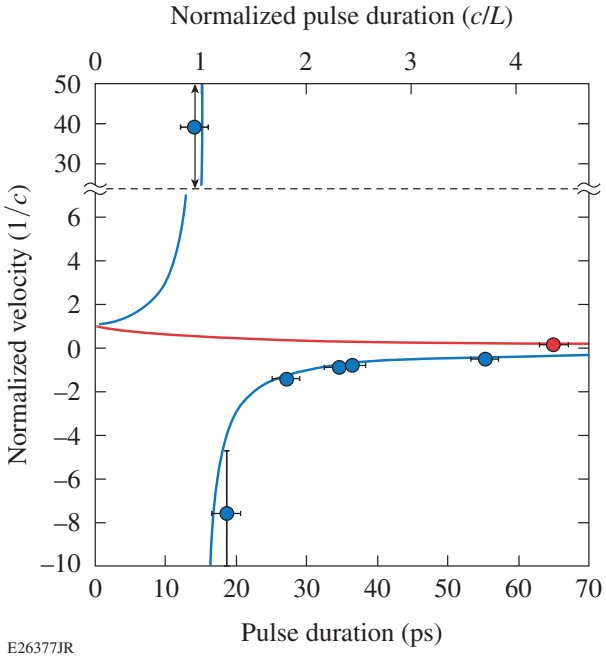

Figure 151.2
The measured (points, bottom axis) and calculated (curves, top axis) [Eq. (1): $v/c = (1 \pm cT/L)^{-1}$] focal-spot velocity plotted as a function of the pulse duration of the laser. The red (blue) symbols represent a positively (negatively) chirped laser pulse. For all but two of the data points, the error in the velocity measurements is smaller than the symbols (<2.5%). For the data point with a pulse duration of 14 ps (very close to the L/c), the error in the velocity measurement is large since the focal velocity is nearly 50× the speed of light.

which shows a potential path to generating a deep ultraviolet laser. In the final section, the concept and its potential impact are summarized.

Experimental Setup

MTW is a Nd:glass optical parametric chirped-pulse–amplification (OPCPA) laser with a central wavelength of $\lambda_0 = 1054$ nm. The bandwidth ($\Delta\lambda = 9.2$-nm full width at 0.1× maximum) was stretched to produce a 2.6-ns linear chirp, and a set of compressor gratings subsequently compressed the pulse to the desired chirped-pulse duration. Undercompression relative to the transform-limited pulse duration resulted in a positive linear chirp [$\lambda(\tau) = (\Delta\lambda/T)\tau + \lambda_r$] and overcompression resulted in a negative linear chirp [$\lambda(\tau) = -(\Delta\lambda/T)\tau + \lambda_b$]. A diffractive lens with a focal length of $f_0 = 511$ mm (at λ_0) generated an ~15-μm-diam focus with a longitudinal separation of $L \simeq 4.5$ mm between the extreme wavelengths. This focal region was nearly 100× the Rayleigh length ($Z_R = 0.05$ mm) of the $f/7$ system.

The velocity of the focus over the longitudinal separation was determined by measuring the radial intensity profile along

the laser beam's axis as a function of time. The experiments used a parallel-path configuration (Fig. 151.3), where the collimated laser beam (R = 3.5 cm) was split into two identical beams to form signal and reference paths that were then imaged onto a P510 Rochester optical streak system (ROSS) camera. Inside one of the parallel paths, the signal path was focused by the diffractive lens (f_0 = 550 mm) and the reference path was focused by an achromatic lens with an f_1 = 400-mm focal length. Both legs used achromatic lenses ($f_{r,s}$ = 400 mm) to collimate the light that was then recombined with a slight angle to separate the images at the detector plane. The beams were focused to the detector with a final achromatic lens (f_2 = 400 mm) that produced an image of the reference and signal focal regions. Modeling indicated that the optical system was

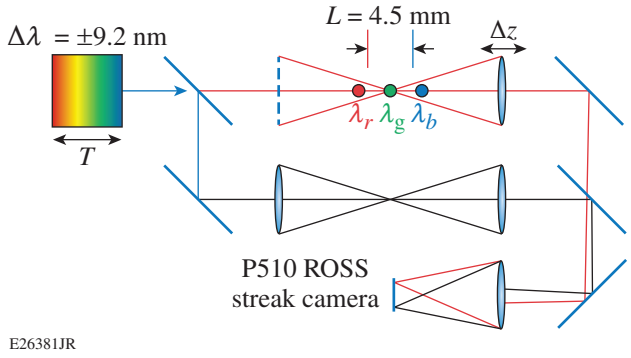

Figure 151.3
A schematic of the experimental setup. ROSS: Rochester optical streak system.

~3× diffraction limited (~15 μm) over the wavelength range of interest. The spatial resolution at the detector plane of the ROSS camera was ~50-μm full width at half maximum (FWHM). The reported pulse duration (T) was determined using the reference pulse measured on the ROSS camera. The impulse response of the streak camera was measured to be 7-ps FWHM.

The diameter of the signal pulse as a function of longitudinal position (z) along the longitudinal focal length was determined by moving the collection lens (f_s) over successive positions spanning slightly beyond the range of extreme focal positions. At each z position, several images were recorded by the streak camera and averaged to increase the signal-to-noise ratio. The reference pulse was used to remove jitter between images. Each composite image generated a measurement of the time between the reference pulse and the signal pulse (τ).

Figure 151.4 shows the results for a negatively chirped laser pulse with a duration of T = 36.4±1 ps. The images indicate that the focal spot counter-propagated at a velocity of –0.77c±2%. When measuring the focal spot at a position closest to the diffractive lens (z = –1.5 mm), the diameter of the flying focus was measured to evolve in time from a large spot size to a best-focus spot size over the pulse duration (i.e., the laser spot does not come to focus until the end of the laser pulse). This is in contrast with the measurements that image a position 3.0 mm farther from the diffractive lens (z = 1.5 mm). In this case, the focal-spot size was measured to start at its best focus

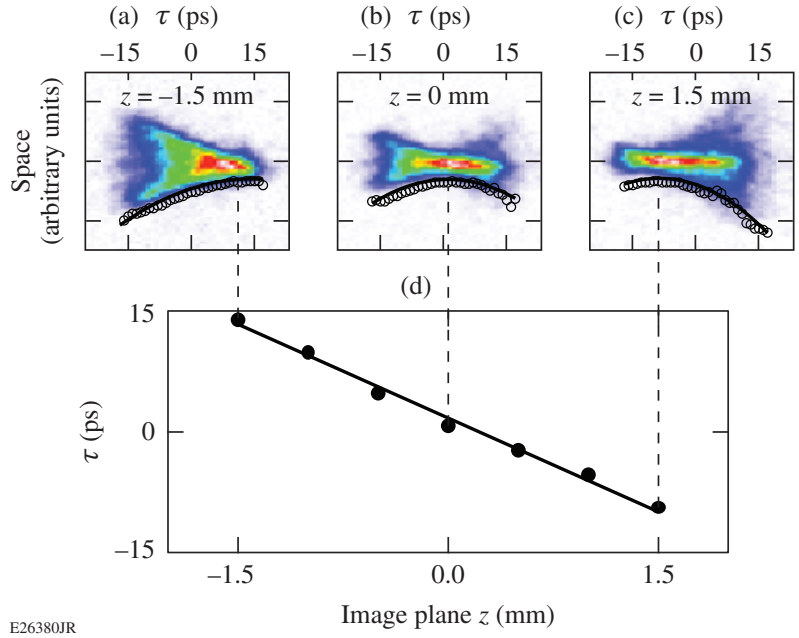

Figure 151.4
Three streak camera images recorded for a pulse duration of T = 36.4 ps, where the image plane was focused at (a) z = –1.5 mm, (b) z = 0 mm, and (c) z = 1.5 mm. Plotted over the image is the corresponding full width at 0.2× the peak-power spot size as a function of time. (d) The solid curve is a best fit to the data used to determine the time of minimum spot size (τ). The measured times (points) are shown for this data set. The best-fit line indicates a focal-spot velocity of v/c = –0.77±0.015.

and expand to a maximum diameter over the duration of the laser pulse (i.e., the laser spot starts at focus and expands until the end of the laser pulse).

The velocity of the focus $\{v = \Delta z/\Delta t = c\,[1 + (\Delta\tau/\Delta z)\,c]^{-1}\}$ was determined by measuring the time of minimum foci (τ) at each image plane (z). The slope of a best-fit line to the measured data [Fig. 151.4(b)] was used to determine $m = c\Delta\tau/\Delta z$. The error in the measurements shown in Fig. 151.2 is given by $\delta v/v = v\delta m$, where δm is the uncertainty in each fit.

Results

Figure 151.5 shows measurements of the flying focus generated by both a negatively and a positively chirped laser pulse. The initial frame of the negatively chirped pulse shows the laser beam entering the focal region, but before it has reached focus.

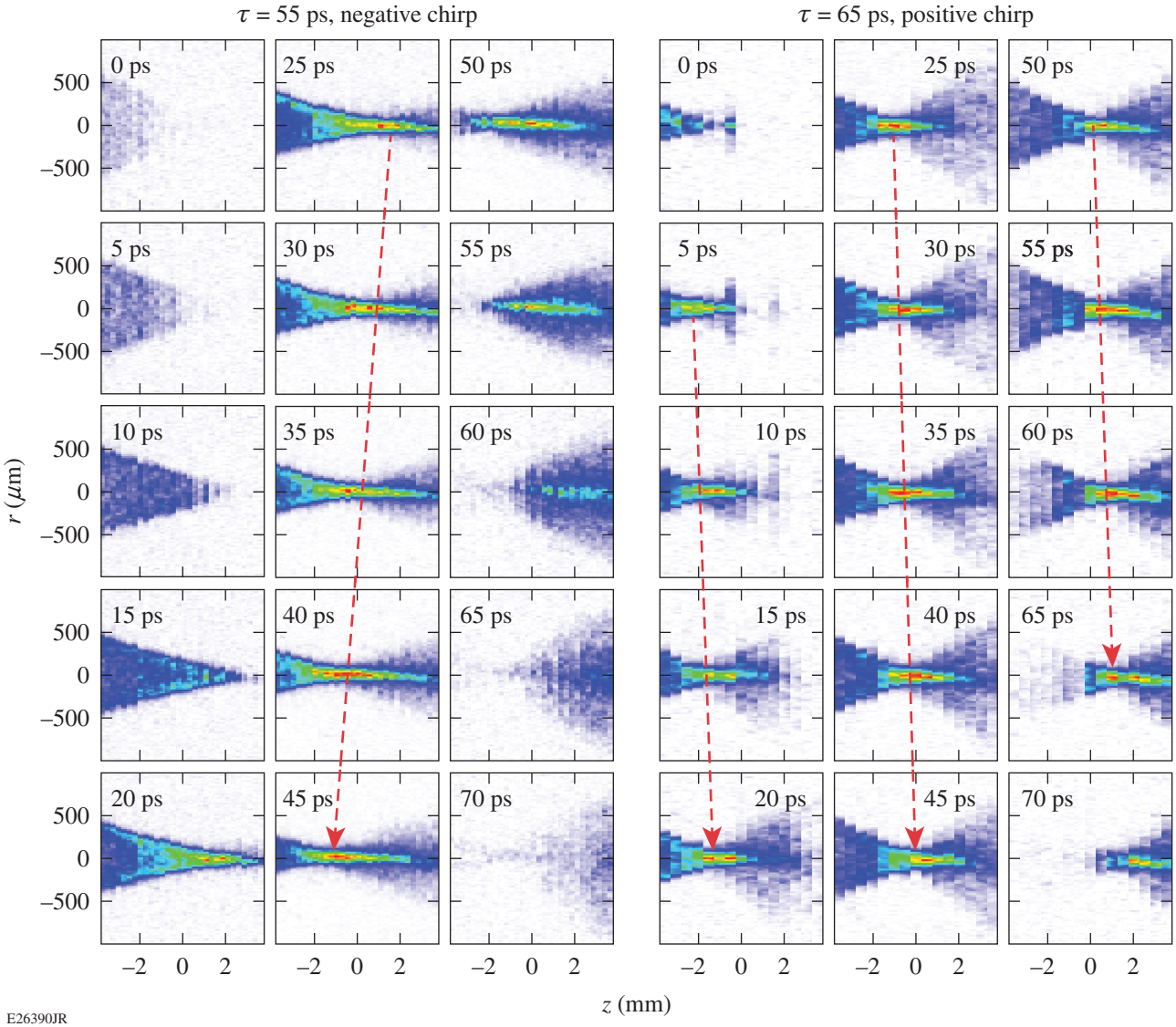

Figure 151.5
The evolution of the flying focus intensity measured for a negative (left) and positive (right) chirped pulse, each with a duration of $T \sim 60$ ps. In each case, the laser is shown propagating into the measurement window (top left) at 0 ps. In the positively chirped case, the laser comes into focus at the left edge of the window ($z \sim -2.5$ mm), in contrast to the negatively chirped case, where the pulse is far from focus. At $t = 25$ ps (top middle), the negatively chirped case shows that the laser has reached focus at the back of the window ($z \sim +2$ mm). Over the next few frames, the focus propagates ~ –2 mm in ~20 ps, corresponding to $-0.3c$, while over the same time, the positively chirped pulse moves forward slowly at ~ $+0.2c$.

Over the next 20 ps, the laser reaches a focus at the far end of the system ($z \sim 2$ mm). This is in contrast with the positively chirped pulse, where the laser comes into focus initially at the front of the measurement window ($z \sim -2$ mm). Comparing the middle row for each data set shows that the focal spots are propagating in opposite directions. For the negatively chirped pulse, the peak intensity moved back toward the lens by $\Delta z \sim 2$ mm over the ~20 ps corresponding to a velocity of $-0.3c$, while for the positively chirped pulse, the peak intensity moved forward by about the same distance in a comparable time corresponding to a velocity of about $+0.2c$. Figure 151.5 was constructed from temporal measurements of 30 longitudinal locations ranging from $z = -3.75$ mm to $z = +3.75$ mm. The measured images were sliced into temporal bins and recombined given their focal location and measured time (t).

The measured velocity of the focus as a function of the pulse duration of the laser compares well with the calculations using Eq. (1) (Fig. 151.2). The results show that when the laser pulse was negatively chirped with a duration of $T = 34.4$ ps, the focal spot counter-propagated at a velocity of $v = -0.87c \pm 2\%$. Reducing the pulse duration ($T = 18.6$ ps) resulted in a counter-propagating superluminal focus ($v = -7.6c \pm 20\%$). Extending the pulse duration to $T = 232$ ps slowed the focal spot propagating at $v/c \simeq -0.09 \pm 1\%$. When the pulse duration was just less than the transit time of the light to propagate across the focal region, the focus was measured to propagate at nearly 50× the speed of light. A positive chirp provides access to a range of forward-propagating subluminal velocities. The focal-spot velocity for a positively chirped laser pulse with a duration of $T = 65$ ps was measured to propagate at $v = 0.20c \pm 1\%$.

Figure 151.6 shows snapshots of the longitudinal intensity profiles calculated for three different negative chirp cases. They illustrate propagating backward at the speed of light [Fig. 151.6(a)], propagating instantaneously across the focal volume [Fig. 151.6(b)], and propagating forward faster than the speed of light [Fig. 151.6(c)]. They were calculated by assuming Gaussian optics, $I(z,t)/I_0 = \left[w_0/w(z,t)\right]^2$, where $w_0 \simeq 1/(2G_R)$ is the diffraction-limited spot size and

$$w(z,t) \simeq w_0 \sqrt{1 + \frac{f_0^2}{4Z_R^2}\left[\frac{z}{f_0} + \frac{\lambda_0}{\lambda(\tau)} - 1\right]^2} \qquad (3)$$

is the radius of the flying focus spot. The Rayleigh length for a diffractive lens is given by

$$Z_R \simeq f_0^2 \lambda_0 / 4R^2 \simeq 1/4G_R^2\lambda = 52\ \mu\text{m},$$

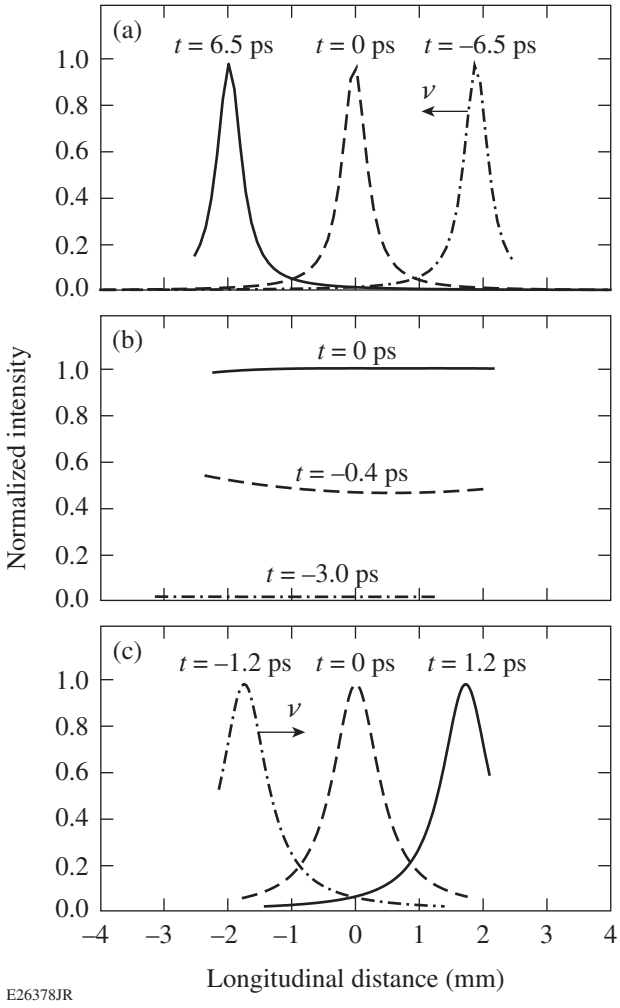

Figure 151.6
The instantaneous longitudinal intensity is plotted for a focus (a) counter-propagating at the speed of light ($T = 2L/c = 29.8$ ps, $\Delta\lambda = -9.2$ nm), (b) propagating at an "infinite" velocity ($T = L/c = 14.9$ ps, $\Delta\lambda = -9.2$ nm) and (c) co-propagating at 5× the speed of light ($T = 0.8\ L/c = 11.9$ ps, $\Delta\lambda = -9.2$ nm). Snapshots of the intensity profiles at early time (dotted–dashed curves), middle time (dashed curves), and late time (solid curves).

where G_R is the groove density at the radius of the laser beam (R). This is a reasonable approach to calculating the intensity profile provided that the pulse duration is much larger than the radial pulse front delay ($T > T_{\text{RPFD}} = 5$ ps).

The intensity of the flying focus across the longitudinal focal region is given by the spectral power, $I(z,t) = P(\lambda)/\pi\left[w(z,t)\right]^2$, which shows that the longitudinal intensity can be controlled by spectrally shaping the laser pulse. In the experiment, 1.6 nm of bandwidth was removed from the middle of a positively chirped spectrum, which demonstrated that the laser did not focus over the central region of the longitudinal focus. The measured laser

focus propagated subluminally (v/c = 0.16±1%) over the first ~2 mm and then did not focus again for ~26 ps, at which time the focus reappeared at $z \sim 2.8$ mm and propagated to the end of the longitudinal focal region.

Applications

For more-exotic applications, the velocity of the focus can be varied by using a nonlinear chirp and/or a nonlinear chromatic optical system. From Eq. (1), it is evident that the focal velocity could be made to accelerate, decelerate, or oscillate across the longitudinal focal region depending on the design of the nonlinear chirp. An example that demonstrates the impact of the flying focus is a photon accelerator. A photon accelerator frequency upshifts light using rapidly changing density $\left(\mathrm{d}n_\mathrm{e}/\mathrm{d}t\right)$ generated by, for example, an ionization wave. Prior photon accelerator concepts have been limited by phase slippage, where the upshifting laser beam accelerates out of the density gradient.[23] A flying focus using a nonlinear chirp could mitigate this by making the velocity of the ionization wave follow the group velocity of the upshifting beam:

$$\frac{\mathrm{d}z}{\mathrm{d}t} = v_\mathrm{g}(t) = c\sqrt{1-\omega_p^2/\omega(t)^2}, \tag{4}$$

where $\omega_p^2 = n_\mathrm{e}e^2/m_\mathrm{e}\epsilon_0$ and n_e is the maximum electron plasma density. In this case, the photons will be frequency upshifted[27] from an initial frequency ω_0':

$$\frac{\Delta\omega(t)}{\omega_0'} = \frac{\omega(t)-\omega_0'}{\omega_0'} = \sqrt{1+\left(\frac{\omega_p}{\omega_0'}\right)^2\frac{z(t)}{Z_\mathrm{R}}}-1, \tag{5}$$

where $z(t)$ is the trajectory of the ionization wave (i.e., the trajectory of the flying focus) and Z_R is an approximate width of the ionization wave that was assumed to be equal to the Rayleigh length of the flying focus.

Figure 151.7(a) shows the results from Eq. (5) where photons with an initial group velocity of $v_\mathrm{g} = 0.7c$ were accelerated to $v_\mathrm{g} = 0.99c$ over 4.5 mm (from $\lambda_0' = 1054$ nm to $\lambda' \simeq 160$ nm at $n_\mathrm{e} = 5\times10^{20}$ cm^{-3}). In a standard photon accelerator design where the ionization wave propagates at a constant velocity given by the initial group velocity of the seed photons, the accelerated photons would be limited to $v_\mathrm{g} = 0.9c$ (~550 nm). In this case, the accelerated photons overtake the ionization wave within the first 0.3 mm. The maximum photon energy in a photon accelerator driven by a flying focus is limited by the accelerator length, which is given by the total bandwidth in the laser [$L = f_0(\Delta\lambda/\lambda)$].

Figure 151.7(b) shows the corresponding nonlinear chirp that is required to follow the accelerating trajectory. There are two solutions that both require a negative chirp. The solutions depend on whether the pulse duration of the flying focus is greater than or less than the time it takes for light to transverse the accelerator ($T = L/v_\mathrm{g} \simeq 15$ ps). When the pulse duration is

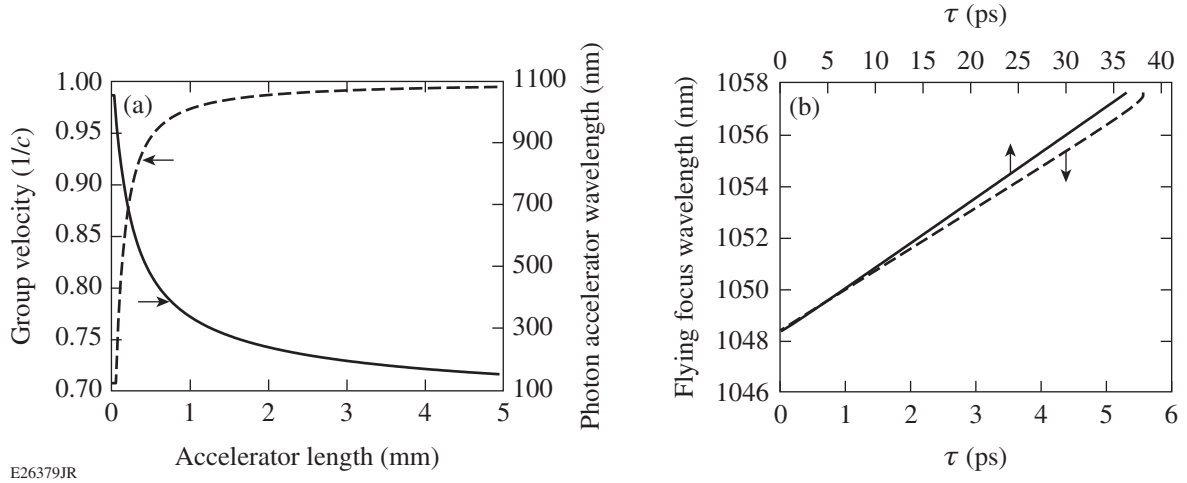

Figure 151.7

(a) The velocity of the accelerating photons (left axis, dashed curve) and their wavelength (right axis, solid curve) are plotted as functions of accelerator length for a system where the ionization wave is produced by an accelerating flying focus. The electron density was assumed to rise from vacuum to $n_\mathrm{e} = 5\times10^{20}$ cm^{-3} over the Rayleigh length of the flying focus (Z_R = 0.05 mm). (b) The nonlinear chirp is required for the flying focus to accelerate in phase with the frequency-shifted photons toward the diffractive lens (bottom axis) and away from the diffractive lens (top axis).

longer than the L/v_g, the flying focus will counter-propagate with respect to the flying focus beam; when the pulse duration is shorter than L/v_g, the flying focus will co-propagate. This nonlinear chirp accounts for the initial rapidly changing group velocity of the accelerating photons [Fig. 151.7(a)]. Extending the bandwidth to a typical value available in current ultrashort pulse lasers ($\Delta\lambda/\lambda_0 \simeq 200$ nm/1000 nm) lengthens the accelerator to nearly $L \simeq 10$ cm, and the accelerated photons reach a final wavelength of 100 nm, assuming the same conditions for the ionization wave as above. The maximum wavelength shift could be significantly increased by using a density ramp to maintain a constant $\omega_p / \omega'(t)$ as the photons are accelerated.

Summary

The flying focus provides an avenue for novel control over laser–plasma interactions, removes the need for long-focal-length systems or guiding structures to maintain high intensities over long distances, and decouples the velocity of the focal spot from the group velocity of the light. In addition to photon accelerators, the spatiotemporal control of laser intensity achieved by the flying focus has the potential to change the way plasma devices are optimized and could be applied in many areas of physics. In a laser wakefield accelerator,[28,29] the flying focus could eliminate dephasing by generating a focal spot that moves at a velocity that matches the accelerating electrons. This separation of the accelerator length from the plasma density will provide larger accelerating fields for a given accelerator length and could expand the options for optimizing laser-plasma accelerators. Furthermore, applying the flying focus to a laser-plasma amplifier will allow the ionizing pump laser intensity to propagate at $v = -c$ in order to generate a counter-propagating ionization wave just ahead of the amplifying seed pulse. This will enable one to control the plasma conditions observed by the seed and could be the enabling technology for an efficient laser-plasma amplifier (see the next article, **Raman Amplification with a Flying Focus**).

ACKNOWLEDGMENT

This material is based upon work supported by the Department of Energy Office of Fusion Energy Sciences under contract No. DE-SC0016253, Department of Energy National Nuclear Security Administration under Award Number DE-NA0001944, the University of Rochester, and the New York State Energy Research and Development Authority.

REFERENCES

1. S. S. Bulanov *et al*., Phys. Rev. Lett. **105**, 220407 (2010).
2. C. Pellegrini, Eur. Phys. J. H **37**, 659 (2012).
3. C. Joshi and T. C. Katsouleas, Phys. Today **56**, 47 (2003).
4. S. Corde *et al*., Nature **524**, 442 (2015).
5. C. B. Schroeder *et al*., Phys. Rev. ST Accel. Beams **13**, 101301 (2010).
6. V. Malka *et al*., Nat. Phys. **4**, 447 (2008).
7. C. G. Durfee and H. M. Milchberg, Phys. Rev. Lett. **71**, 2409 (1993).
8. S. Jackel *et al*., Opt. Lett. **20**, 1086 (1995).
9. F. Dorchies *et al*., Phys. Rev. Lett. **82**, 4655 (1999).
10. D. J. Spence and S. M. Hooker, Phys. Rev. Lett. **63**, 015401(R) (2000).
11. D. H. Froula, L. Divol, P. Davis, J. P. Palastro, P. Michel, V. Leurent, S. H. Glenzer, B. B. Pollock, and G. Tynan, Plasma Phys. Control. Fusion **51**, 024009 (2009).
12. B. Wattellier *et al*., Opt. Lett. **27**, 213 (2002).
13. E. E. García-Guerrero *et al*., Opt. Express **15**, 910 (2007).
14. H. Vincenti and F. Quéré, Phys. Rev. Lett. **108**, 113904 (2012).
15. V. M. Malkin, G. Shvets, and N. J. Fisch, Phys. Rev. Lett. **82**, 4448 (1999).
16. J. Ren *et al*., Nat. Phys. **3**, 732 (2007).
17. R. M. G. M. Trines *et al*., Nat. Phys. **7**, 87 (2011).
18. G. Vieux *et al*., Sci. Rep. **7**, 2399 (2017).
19. T. Tajima and J. M. Dawson, Phys. Rev. Lett. **43**, 267 (1979).
20. C. Joshi *et al*., Nature **311**, 525 (1984).
21. R. Bingham, Nature **394**, 617 (1998).
22. S. M. Hooker, Nat. Photonics **7**, 775 (2013).
23. S. C. Wilks, J. M. Dawson, and W. M. Mori, Phys. Rev. Lett. **61**, 337 (1988).
24. A. Butler *et al*., Phys. Rev. Lett. **91**, 205001 (2003).
25. J. J. Rocca *et al*., Phys. Rev. Lett. **73**, 2192 (1994); **75**, 1236(E) (1995).
26. V. Bagnoud, I. A. Begishev, M. J. Guardalben, J. Puth, and J. D. Zuegel, Opt. Lett. **30**, 1843 (2005).
27. J. T. Mendonça, *Theory of Photon Acceleration*, Series in Plasma Physics (Institute of Physics Publishing, Bristol, England, 2000).
28. C. G. R. Geddes *et al*., Nature **431**, 538 (2004).
29. S. Steinke *et al*., Nature **530**, 190 (2016).

Raman Amplification with a Flying Focus

Introduction

Continuing to push the boundary of laser intensity using existing technology is increasingly challenged by the need for large, efficient, and damage-resistant gratings. Here, we propose a new laser amplifier scheme utilizing stimulated Raman scattering in plasma in conjunction with a "flying focus"—a chromatic focusing system combined with a chirped pump beam that provides spatiotemporal control over the pump's focal spot.[1] Localized high intensity is made to propagate at $v = -c$ just ahead of the injected counter-propagating seed pulse. By setting the intensity in the interaction region to be just above the ionization threshold, an ionization wave is produced that travels at a fixed distance ahead of the seed. Simulations show that this will make it possible to optimize the plasma temperature and mitigate many of the issues that are known to have impacted previous Raman amplification experiments, in particular the growth of precursors.

Plasma-based laser amplifiers utilizing either stimulated Raman scattering[2] (SRS) or strongly coupled stimulated Brillouin scattering[3–8] have long been of interest. Lacking a damage threshold, compact plasma-based systems could produce unfocused intensities $I \approx 10^{17}$ W/cm^2—more than six orders of magnitude larger than conventional systems. Typically, a moderate-intensity pump pulse with a duration of at least $2L/c$ propagates across a plasma of length L. When the pump's leading edge reaches the end of the plasma, an initially weak seed pulse is injected in a counter-propagating geometry. Tuned to satisfy the Manley–Rowe frequency- and wave-number–matching conditions, the beat wave between the two beams drives a plasma wave that mediates energy transfer from the pump to the seed (c.f., Fig. 151.8). While early work[9–12] on Raman-based plasma amplifiers appeared promising, progress has slowed and numerous attempts have been made recently to elucidate the shortcomings of experiments. A consensus is emerging that thermal effects[13–20] and the amplification of precursors growing from noise ahead of the seed pulse[13,21–25]—issues that are both related to the pump's traversal of ionized plasma prior to meeting the seed—may be among the most pervasive issues that degrade performance.

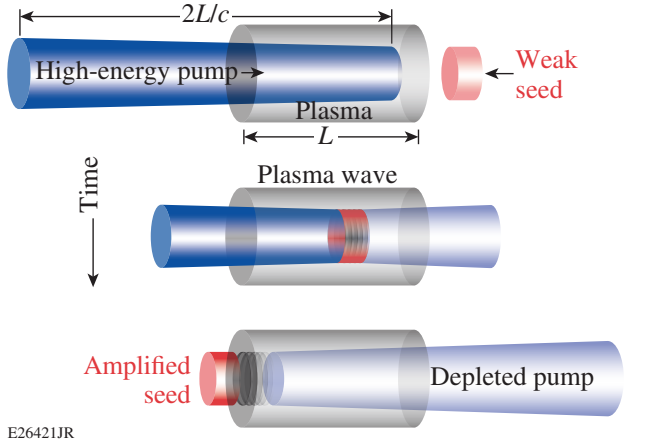

Figure 151.8
A moderate-intensity pump pulse with a duration of at least $2L/c$ propagates across a plasma of length L. When the pump's leading edge reaches the end of the plasma, an initially weak seed pulse is injected in a counter-propagating geometry. Tuned to satisfy the Manley–Rowe frequency- and wave-number–matching conditions, the beat wave between the two beams drives a plasma wave that mediates energy transfer from the pump to the seed.

An alternate scheme has been proposed to mitigate precursor growth in which the seed ionizes the plasma coincident with its amplification by the pump.[26] However, this introduces additional constraints: the pump intensity must be below the threshold for ionization, limiting the Raman growth rate; conversely, the initial seed intensity must be high enough to photoionize the plasma, limiting the degree to which it can be further amplified; and the ionization itself damps the growing seed pulse. To our knowledge, this scheme has yet to be tested because of the added complexity.

A Raman amplifier with a flying focus retains the advantages of seed ionization while eliminating its downsides. A chirped pump is focused by a diffractive lens that introduces chromatic aberration in order to produce a longitudinally distributed focal spot. The temporal dispersion provided by the chirp, combined with the spatial dispersion provided by the lens, provides spatiotemporal control over the propagation of intensity isosurfaces. In the example shown in Fig. 151.9,

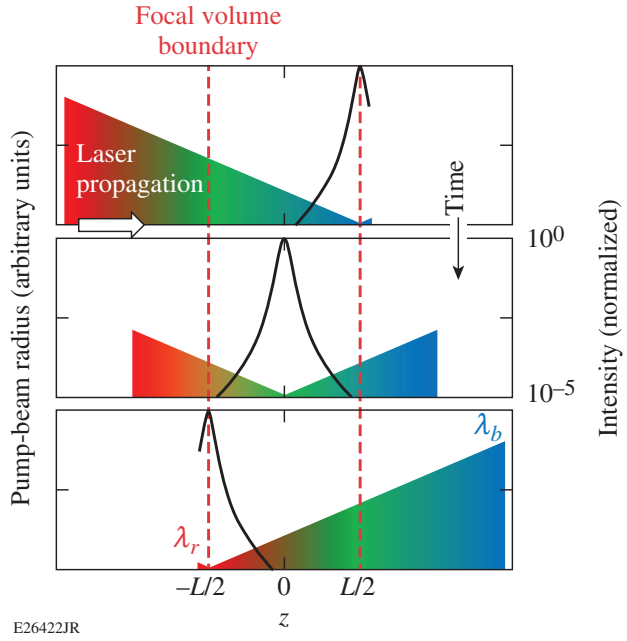

Figure 151.9
A negatively linearly chirped pump combined with a chromatic focusing system causes the high-intensity focus to propagate backward at $v \approx -c$ when the pump duration is $2L/c$, where L is the distance between the foci of the pump's bandwidth extrema.

the pump has a negative linear chirp and a pulse duration that is equal to $T = 2L/c$, where L is both the length of the focal region spanned by its bandwidth and the length of the amplifier interaction region. In this case, the desired pump intensity first appears where the pump exits the interaction region and subsequently propagates backward at $v \approx -c$ at a constant value over a length that can be many times the Rayleigh length. More details regarding the flying focus optical system, along with additional applications, are contained in the companion article **Flying Focus: Spatiotemporal Control of the Laser Focus**, p. 115.[1]

To demonstrate the benefits of this concept, the coupled three-wave equations describing SRS in plasma were solved numerically (see, e.g., Refs. 13 and 26 and references therein). Such models have previously been benchmarked against particle-in-cell simulations and found to be in good agreement when plasma-wave amplitudes were kept below the wave-breaking limit and kinetic effects could be ignored [at low $k_3\lambda_{De} \leq 0.3$, where k_3 is the electron plasma wave's (EPW's) wave number and λ_{De} is the Debye length].[27] The three-wave model is supplemented with a field ionization model to simulate the plasma ionization by the pump.[26] The model is described in much greater detail in **Methods**, p. 125.

For all of the simulations, the initial density of hydrogen atoms was 6×10^{18} cm^{-3} and the interaction length was 4 mm, defining a pump duration of 26.7 ps. The pump wavelength was $\lambda = 1$ μm and the seed was upshifted by the EPW frequency. For the flying focus Raman amplification (FFRA) base case, the pump focusing system was $f/5$ with the focus of each color located past the interaction region. To simulate focusing in this 1-D model, the pump enters from the left edge and its intensity increases as it propagates to the right in a manner that is consistent with the f number of the system. The blue leading edge of the pump converges to a spot diameter of 400 μm at the exit of the interaction region, where the intensity was set to be $I_1 = 1.4 \times 10^{14}$ W/cm^2.

In the simulations, the plasma mediating the energy transfer was formed by the pump beam ionizing the hydrogen gas within the interaction region. The ionization threshold of hydrogen is very close to the optimal pump intensity in systems designed for $\lambda \approx 1$-μm lasers. Since the pump first reaches this intensity at the right edge of the amplifier in the case of FFRA, plasma is initialized there and an ionization wave subsequently propagates backward with the intensity isosurface. The setup can therefore be tuned so that the plasma is formed just before the seed arrival at every point along the interaction region.

The peak of a 500-fs-duration (full width at half maximum) seed pulse with an initial intensity $I = 1 \times 10^{11}$ W/cm^2 was injected at the right edge just after the arrival of the pump's leading edge ($t = 14$ ps). Figure 151.10(a) shows three snapshots of the interaction as the injected seed travels from right to left across the interaction region for the FFRA case. The first frame shows that the gas is ionized only $\left(n_e/n_c > 0\right)$ close to the right edge, where the pump first reaches high intensity. The seed duration stretches as it grows in the linear regime. From the first to the second frame, it is clear that the ionization wave is propagating at an approximately fixed distance ahead of the seed. The nonlinear pump-depletion regime has been reached, with seed pulse compression and the formation of a secondary peak. This efficient amplification continues in the final frame. These results demonstrate the ideal behavior that is expected when the seed enters unperturbed plasma and competing instabilities are avoided.

Contrast Fig. 151.10(a) with the behavior observed in Fig. 151.10(b), which shows the results from a Raman amplifier without the flying focus. In this case, the intensity was set to $I = 1.4 \times 10^{14}$ W/cm^2 at the left edge of the amplifier and was assumed to be collimated as it propagated from left to right (consequently, the pump intensity seen by the seed pulse

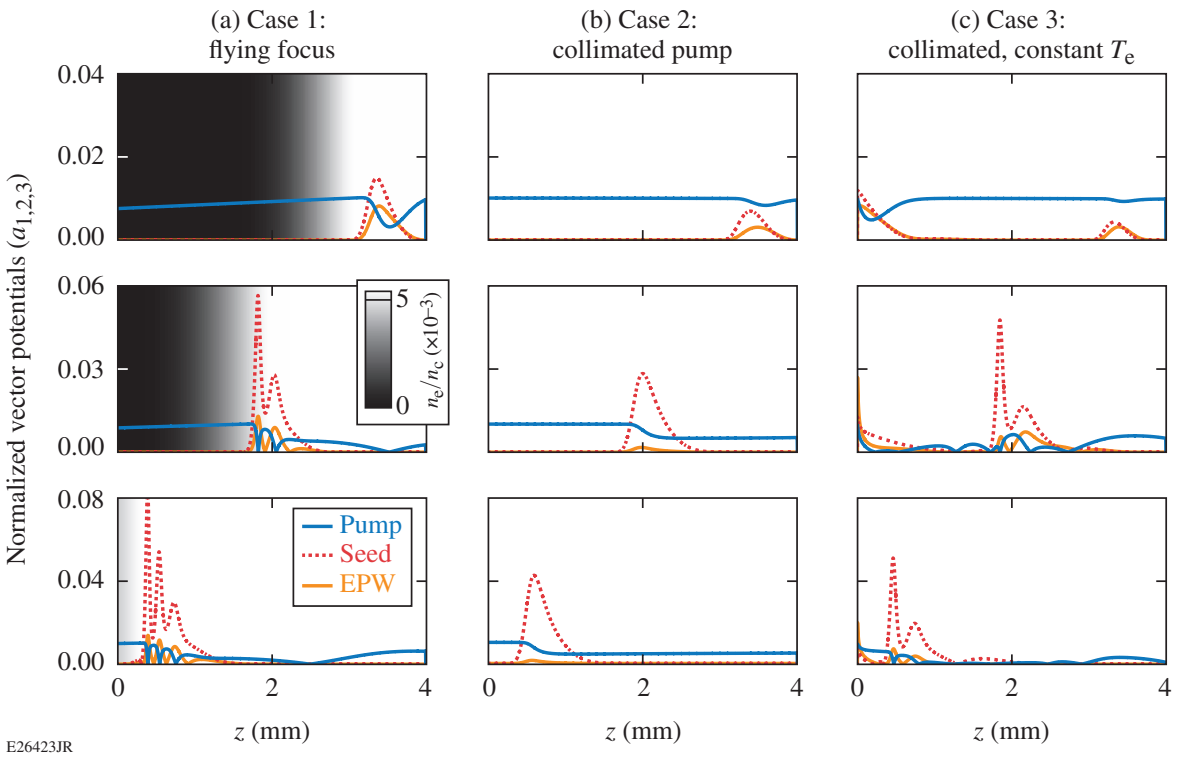

Figure 151.10

Results of three-wave model simulations. (a) With the flying focus, the pump first reaches high intensity at the right edge, where ionization is initialized. Constant intensity moves at $v = -c$ as different colors converge to different locations, so the ionization wave propagates at a nearly fixed distance ahead of the injected seed pulse. Ideal plasma amplifier behavior is observed. (b) When the pump is collimated within the interaction region and above threshold for ionization, the seed encounters higher temperatures along nearly its entire path, which reduces growth via increased Landau damping. (c) With a collimated beam as in Case 2 but holding T_e fixed to be similar to Case 1, spontaneous stimulated Raman scattering (SRS) grows during the long time in which the pump propagates across the ionized plasma. Premature pump depletion degrades the resulting seed amplification. Flying focus Raman amplification (FFRA) Case 1 with noise initialized at the same level did not produce such precursors. EPW: electron plasma wave.

is nearly the same in both cases). The first frame shows that upon reaching the right edge, the plasma is ionized everywhere throughout the interaction region. While growth in the first frame is comparable, it slows rapidly compared to FFRA. Pump depletion and pulse compression fail to occur in this case.

The difference can be understood by looking at the electron temperature encountered by the peak of the seed pulse versus time [Fig. 151.11(a)]. In FFRA "Case 1," after a brief initial growth period, T_e levels off at ≈45 eV because of the nearly constant duration of plasma heating by the pump prior to the seed's arrival at each point along its path. With standard focusing (or a preformed plasma), the seed encountered plasma that was heated for a progressively longer duration as it propagated, producing a strong gradient in T_e (Case 2). This model captures the fact that excessive heating can lead to debilitating levels of collisionless Landau damping, which acts to suppress the seed growth.[13,15] Figure 151.11(b) shows the sum of collisional and collisionless damping as a function of temperature. The former dominates at low temperatures and the latter at high temperatures; FFRA Case 1 is close to the temperature at which EPW damping is minimized.

Note that there could be additional impacts of elevated temperature that are not captured by this model. The thermal gradient seen by the seed pulse can lead to resonance detuning resulting from the Bohm–Gross frequency shift.[14] Detuning can also result from the kinetic nonlinear frequency shift that accompanies particle trapping.[16,19,25] Perhaps most importantly, the wave-breaking threshold is reduced in warm plasma,[17–19,28] which limits the plasma-wave amplitudes and thereby the energy transfer from pump to seed. This model, therefore, likely underestimates the adverse effects of high temperature and lack of temperature control with a conventional focusing and ionization scheme.

Given the uncertainties, a temperature of ≈45 eV may not be optimal. A nice feature of the FFRA scheme, however,

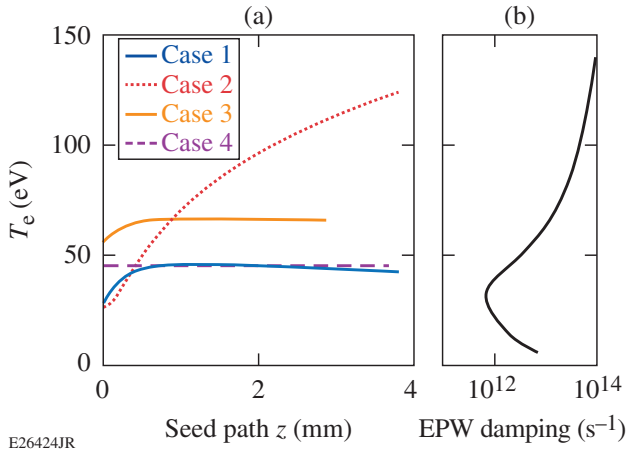

Figure 151.11
(a) In Case 1, the temperature encountered by the seed was nearly constant everywhere because of the ionization wave propagating ahead of the seed. In Case 2, the seed encountered progressively higher temperatures because each slice of plasma was heated for a longer duration. Case 3 used the flying focus (like Case 1) but delayed the seed injection by 3 ps, which shows that T_e is tunable. Case 4 used a collimated pump (like Case 2), but T_e was artificially fixed to be similar to Case 1; this case illustrates the negative effect of precursor growth. (b) The electron plasma wave damping is minimized around $T_e \approx$ 40 eV, so the FFRA scheme can be tuned to operate close to this temperature.

is that the temperature can be easily tuned by adjusting the delay between the ionization wave and the injected seed pulse. Many parameters can influence this delay. Holding all else constant but injecting the seed 3 ps later, its peak encounters an electron temperature that is uniformly higher by ~20 eV [c.f., Fig. 151.11(a), Case 3]. Because of the higher temperature, it takes longer to reach pump depletion and the secondary peaks are suppressed. Both the interaction pump intensity relative to the ionization threshold of the gas and the pump's f number are additional parameters for tuning the delay between ionization and seed injection.

To investigate nonthermal differences between FFRA and standard Raman amplifiers, a Case 4 was run, repeating Case 2 but with a fixed electron temperature ($T_e = 45$ eV). Although the seed encountered a similar electron temperature everywhere in Cases 1 and 4, the pump spent a longer time in ionized plasma prior to seed injection in Case 4 compared to FFRA Case 1. The debilitating effect of spontaneous SRS growing ahead of the seed is observed in Fig. 151.10(c). Although seed growth over the first half of the plasma proceeds in a similar fashion as Case 1, subsequent growth is suppressed because of premature pump depletion and interference with pre-existing EPW's. Although noise was included in the same manner in FFRA Case 1, no spontaneous SRS growth was observed because of the limited distance over which it could grow ahead of the seed.

As with temperature, this model likely underestimates the negative impacts of spontaneous SRS. While the zeroth-order effect is competition for pump energy,[13] there is some evidence that saturation of even low-level precursors can corrupt plasma conditions (e.g., with driven ion-acoustic waves or modified electron distribution functions) over relatively long time scales.[23,24] In these situations, the seed does not encounter quiescent plasma and its growth is compromised. The controlled introduction of frequency detuning has been proposed to mitigate precursors without precluding the desired seed amplification (resulting from the larger resonance bandwidth of the latter in the nonlinear pump-depletion regime).[21,22] Despite evidence that modern experiments have been adversely affected by too much frequency detuning,[18] spontaneous SRS continues to be an issue and was recently observed to dominate the overall backscatter as the Raman growth rate was increased.[25]

The use of a chirped pump beam—a feature of many previous experiments[10–12,15,23,24] is necessary for the flying focus but does introduce some frequency detuning for fixed plasma conditions that could degrade performance.[18] It could be compensated for, however, by introducing a density gradient along the seed path in order to exactly satisfy the frequency-matching condition everywhere. While perfect resonance may result in undue levels of spontaneous SRS in a typical plasma amplifier,[21,22] it would not degrade FFRA because of the alternative means by which FFRA suppresses precursor growth.

Methods

The basic three-wave equations are

$$\begin{aligned}
&\left(\partial_t - v_1\partial_x + \nu_1\right)a_1 = Ka_2a_3,\\
&\left(\partial_t - v_2\partial_x + \nu_2\right)a_2 = Ka_2a_3^*,\\
&\left(\partial_t - v_3\partial_x + \nu_3 + i\delta\omega\right)a_3 = Ka_1a_2^* + S_3,
\end{aligned} \tag{1}$$

where the subscripts 1, 2, and 3 refer to the pump, the seed, and the EPW, respectively; v_i's are group velocities; ν_i's are damping rates; $K = \omega(n_e/n_c)^{1/4}/2$ is the wave-coupling parameter, where n_e is the electron density and n_c is the critical density; $a_{1,2} = 0.855\times10^3\,\lambda_{1,2}\,(\mu\text{m})\sqrt{I_{1,2}\,(\text{W/cm}^2)}$ are normalized laser vector potentials, and $a_3 = |e|\langle E_3\rangle/m_e c\sqrt{\omega\omega_{pe}}$ is the normalized envelope of the EPW, with pump frequency ω and EPW frequency ω_{pe}. Advection of the plasma wave can be neglected ($v_3 \approx 0$), and here detuning was also neglected ($\delta\omega = 0$) since it has been explored

extensively elsewhere.[13,14,18,21,22] The pump and seed are damped collisionally, $\nu_{1,2} = \nu_{ei}(\omega_{pe}^2/\omega^2)$ with $\nu_{ei} = 2.9 \times 10^{-6}\, Zn_e\ (\mathrm{cm}^{-3})\ \Lambda T_e\ (\mathrm{eV})^{-3/2}$; $\nu_3 = \nu_{ei} + \nu_L$ includes both collisional absorption and collisionless (Landau) damping, with $\nu_L \approx \sqrt{\pi/2}\left[\omega_{pe}^4/(k_3 v_e)^3\right]\exp\left[-\omega_{pe}^2/2(k_3 v_e)^2\right]$. S_3 is a noise term that is included to investigate spontaneous SRS growing from undriven plasma fluctuations. Following Ref. 13, $S_3 = c_1 \nu_3 T_e$ is assumed to be proportional to the EPW damping rate and electron temperature, but a multiplier c_1 was added to test the sensitivity to the initial noise level. Experiments often find that plasma fluctuations are elevated over the expected thermal levels.

The three-wave model was supplemented with an ionization model to simulate the plasma ionization by the pump[26]

$$\partial_t n_e = n_n w(a_1), \qquad \partial_t n_n = -n_n w(a_1), \tag{2}$$

where n_n is the neutral gas density and $w(a_1)$ is the ionization rate that depends on the local pump intensity. In the regime of interest, the Keldysh formula is valid.[29,30] For $\gamma = \sqrt{2U_I/m_e c^2}/a_1 \gg 1$, where U_I is the ionization potential, the multiphoton ionization rate $w(a) \cong \omega N^{3/2}(2\gamma)^{-2N}$ is appropriate, where $N = 1 + \mathrm{int}\left(U_I/\hbar\omega\right)$ is the number of photons required to overcome the ionization potential. For $\gamma \ll 1$, the tunneling formula is more accurate:

$$w(a) \cong 4\Omega_0 \left(\frac{U_I}{U_H}\right)^{5/2} \frac{a_H}{a_1} \exp\left[-\frac{2}{3}\left(\frac{U_I}{U_H}\right)^{3/2} \frac{a_H}{a_1}\right],$$

with atomic frequency $\Omega_0 \cong 4.1 \times 10^{16}\ \mathrm{s}^{-1}$, hydrogen ionization potential $U_H = 13.6$ eV, and the hydrogenic electric-field normalized vector potential $a_H \cong 3.05 \times 10^{14}/\omega$. An exponential fit was used to fill in the region between the multiphoton and tunneling regimes. The molecular nature of hydrogen was approximated by using the molecular ionization potential $U_I = U_{H_2} = 15.4$ eV (Ref. 26). To conserve energy, an additional damping term on the pump was added to Eq. (1) by balancing the equation $n_c\left(m_e c^2/2\right)\partial_t a_1^2 = -\left(U_I + \epsilon\right)\partial_t n_e$, where $\epsilon = m_e v_{osc}^2/2$ is the assumed birth energy and v_{osc} is the oscillation velocity of electrons in the pump laser's electric field. The electron temperature was initialized locally at the birth energy, but it can subsequently evolve to balance collisional absorption of the pump and seed.

ACKNOWLEDGMENT

This work was supported by the U.S. Department of Energy Office of Fusion Energy Sciences under contract No. DE-SC0016253, Department of Energy under Cooperative Agreement No. DE-NA0001944, the University of Rochester, and the New York State Energy Research and Development Authority. The support of DOE does not constitute an endorsement by DOE of the views expressed in this article.

D. Turnbull performed the simulations. T. Kessler contributed information about the diffractive optic. D. Haberberger led the experimental efforts on Raman amplification, supported by J. L. Shaw, A. Davies, and S. Bucht that motivated this work. D.H. Froula proposed the flying focus concept.

REFERENCES

1. D. H. Froula, D. Turnbull, T. J. Kessler, D. Haberberger, J. L. Shaw, J. Katz, and I. A. Begishev, "Flying Focus: Spatiotemporal Control of the Longitudinal Laser Beam Intensity," submitted to Nature Physics.
2. V. M. Malkin, G. Shvets, and N. J. Fisch, Phys. Rev. Lett. **82**, 4448 (1999).
3. A. A. Andreev *et al*., Phys. Plasmas **13**, 053110 (2006).
4. L. Lancia *et al*., Phys. Rev. Lett. **104**, 025001 (2010).
5. G. Lehmann, F. Schluck, and K. H. Spatschek, Phys. Plasmas **19**, 093120 (2012).
6. G. Lehmann and K. H. Spatschek, Phys. Plasmas **20**, 073112 (2013).
7. S. Weber *et al*. Phys. Rev. Lett. **111**, 055004 (2013).
8. L. Lancia *et al*., Phys. Rev. Lett. **116**, 075001 (2016).
9. Y. Ping *et al*., Phys. Rev. E **62**, R4532 (2000).
10. Y. Ping *et al*., Phys. Rev. Lett. **92**, 175007 (2004).
11. W. Cheng *et al*., Phys. Rev. Lett. **94**, 045003 (2005).
12. J. Ren *et al*., Nat. Phys. **3**, 732 (2007).
13. D. S. Clark and N. J. Fisch, Phys. Plasmas **10**, 3363 (2003).
14. R. L. Berger, D. S. Clark, A. A. Solodov, E. J. Valeo, and N. J. Fisch, Phys. Plasmas **11**, 1931 (2004).
15. C. H. Pai *et al*., Phys. Rev. Lett. **101**, 065005 (2008).
16. Y. Ping *et al*., Phys. Plasmas **16**, 123113 (2009).
17. J. P. Farmer, B. Ersfeld, and D. A. Jaroszynski, Phys. Plasmas **17**, 113301 (2010).
18. N. A. Yampolsky and N. J. Fisch, Phys. Plasmas **18**, 056711 (2011).
19. X. Yang *et al*., Sci. Rep. **5**, 13333 (2015).
20. J. D. Sadler, R. M. G. M. Trines, M. Tabak, D. Haberberger, D. H. Froula, A. S. Davies, S. Bucht, L. O. Silva, E. P. Alves, F. Fiúza,

L. Ceurvorst, N. Ratan, M. F. Kasim, R. Bingham, and P. A. Norreys, Phys. Rev. E **95**, 053211 (2017).

21. V. M. Malkin, G. Shvets, and N. J. Fisch, Phys. Rev. Lett. **84**, 1208 (2000).
22. Yu. A. Tsidulko, V. M. Malkin, and N. J. Fisch, Phys. Rev. Lett. **88**, 235004 (2002).
23. D. Turnbull, S. Li, A. Morozov, and S. Suckewer, Phys. Plasmas **19**, 073103 (2012).
24. D. Turnbull, S. Li, A. Morozov, and S. Suckewer, Phys. Plasmas **19**, 083109 (2012).
25. G. Vieux *et al*., Sci. Rep. **7**, 2399 (2017).
26. D. S. Clark and N. J. Fisch, Phys. Plasmas **9**, 2772 (2002).
27. J. L. Kline *et al*., Phys. Plasmas **13**, 055906 (2006).
28. T. P. Coffey, Phys. Fluids **14**, 1402 (1971).
29. P. Sprangle, E. Esarey, and J. Krall, Phys. Rev. E **54**, 4211 (1996).
30. L. V. Keldysh, Sov. Phys.-JETP **20**, 1307 (1965).

Full-Wave and Ray-Based Modeling of Cross-Beam Energy Transfer Between Laser Beams with Distributed Phase Plates and Polarization Smoothing

Introduction

In direct-drive inertial confinement fusion (ICF), a millimeter-scale spherical capsule is uniformly illuminated by symmetrically oriented laser beams.[1,2] The capsules have an outer ablator layer and an inner fuel layer. The lasers ablate the outer layer of the capsule, which generates pressure to implode the fuel. The ICF program relies on radiation–hydrodynamics codes for designing capsules and tuning laser conditions to optimize the hydrodynamic efficiency of implosions.[3] An essential component of these codes is a model for coupling laser energy to the capsule ablator.[4,5]

Laser energy is coupled to the ICF capsule primarily through electron–ion collisional absorption of the laser beams propagating through a coronal plasma that forms around the irradiated capsule.[6] Because the wavelength and period of the lasers are typically much smaller than the hydrodynamic spatial and temporal scales, respectively, the eikonal approximation can be used to solve the steady-state electromagnetic-field equations along ray trajectories using the instantaneous plasma conditions.[7]

In addition to collisional absorption, nonlinear laser–plasma interaction (LPI) processes affect laser-energy deposition. The main nonlinear processes that are thought to be energetically important in ICF experiments are the three-wave processes: stimulated Raman scattering (SRS), stimulated Brillouin scattering (SBS), and two-plasmon decay (TPD).[6] Stimulated Brillouin scattering is the parametric coupling between two electromagnetic waves and an ion-acoustic wave (IAW). When the seed and pump electromagnetic waves in the three-wave SBS process correspond to distinct laser beams, it is referred to as cross-beam energy transfer (CBET).[8,9]

Ray-based laser-energy deposition models that have been adapted to include CBET predict that laser absorption is reduced by ~10% to 20% (Ref. 4) and that laser-energy deposition uniformity is significantly modified in typical direct-drive ICF experiments.[3,10] Hydrodynamic simulations that include CBET show significantly better agreement with measured scattered-light spectra and implosion trajectories, but ray-based CBET calculations must still be modified using *ad hoc* multipliers and field limiters to give quantitative agreement with experimental observations.[11,12] In addition to the eikonal approximation,[7] ray-based CBET models that are used in radiation–hydrodynamics codes assume steady-state linear convective gains, pairwise coupling between rays, and local plane-wave laser beams. Direct-drive ICF experiments also employ polarization smoothing to improve drive-beam uniformity by splitting each laser beam into two beams with orthogonal polarization and a small angular divergence.[13,14] This is accounted for in ray-based models by assuming random relative polarizations of interacting beams and spatially averaged incoherence between the two polarization components of each beam.[15] A more-complete model of CBET is required to test the validity of these approximations.

This article compares wave- and ray-based CBET calculations in the presence of laser beam speckle and polarization smoothing using the full-wave LPI code *LPSE*.[16] The wave-based calculations suggest that laser beam speckle and polarization smoothing can lead to significantly more CBET than is predicted by ray-based calculations. To account for speckle effects in the ray-based model, a modification is presented that gives excellent agreement with wave-based calculations. Full-scale wave-based calculations in hydrodynamic profiles based on direct-drive experiments on the OMEGA laser suggest that beam speckle has a small (<1%) effect on direct-drive laser absorption.

This article (1) puts the current work in the context of previous work on the beam speckle's effect on CBET; (2) describes the ray-based CBET model; (3) describes the equations solved by *LPSE*; (4) compares the ray- and wave-based CBET models for a variety of laser and hydrodynamic configurations using both linearly polarized beams and beams with polarization smoothing; and (5) summarizes the conclusions.

Relation to Other Work

The theory of the speckle statistics of laser beams generated by distributed phase plates was developed using the formalism of Gaussian random fields.[17–20] There has been considerable theoretical work on the impact of laser speckle on filamentation,[21,22] deflection,[23,24] SBS,[25–27] and CBET in the paraxial approximation relevant to indirect-drive ICF.[28] Most of the previous studies of laser beam speckle in the ICF context have focused on ponderomotive self-focusing and filamentation. A recent study looked at the interaction between ponderomotive self-focusing and CBET.[29] The present study focuses on the effect of laser speckle on CBET in the absence of filamentation because this is the situation most relevant to direct-drive ICF experiments, where the single-beam laser intensities are typically well below the filamentation threshold and multibeam filamentation should not be important.[30] The simulations were performed using a full-wave solver that does not make the paraxial approximation and solves the vector wave equation in 3-D, which is essential for studying direct-drive ICF where polarization smoothing is used and beams cross at arbitrary angles.

Ray-based modeling of laser-energy deposition and CBET is now routine in radiation–hydrodynamic simulations of ICF experiments.[4,5] Ray-based CBET models typically inject the beams as plane waves with an intensity equal to the spatially averaged intensity of the speckled laser beams that are used in the experiments. A recent study used the ray-based paraxial complex geometric optics (PCGO) approach to calculate CBET between speckled beams and compared the results to a paraxial wave-based code.[31] The PCGO approach gives a pseudo-speckle pattern that produces a statistical intensity distribution similar to a real speckle pattern over a limited range of speckle intensities. We present a ray-based model for calculating CBET between speckled beams that gives improved agreement with wave-based calculations by using ray tracing to directly solve the electromagnetic-field equations within the eikonal approximation.[7] This produces a real speckle pattern that, in the absence of CBET, exactly matches the wave-based calculation in regions of space where the eikonal approximation is valid and shows excellent agreement with the wave-based CBET calculations up to gains ≳5.

We also present a study of CBET between polarization-smoothed beams. Ray-based models rely on the assumption of uncorrelated polarization and phase to calculate the interaction between laser beams that employ polarization smoothing,[15] but the limits of this approximation have not been previously studied because most previous studies were based on wave-based codes that solve only the scalar wave equation for the electromagnetic fields.

Ray-Based CBET Modeling

Cross-beam energy transfer is calculated along ray trajectories by numerically integrating the steady-state homogeneous gain along ray trajectories using the local plasma conditions.[32] The differential change in the energy of ray i at the jth location along its path caused by an interaction with ray k at the lth location along its path is[9]

$$\frac{\mathrm{d}W_{ij}}{\mathrm{d}s} = -\frac{W_{ij}}{\alpha_{ij}} + W_{ij}\xi_{ij}^{kl}\left(\frac{W_{kl}}{\varepsilon_0}\frac{\mathrm{d}S_{k0}}{\mathrm{d}S_{kl}}\right), \tag{1}$$

where $W_{ij} = \sqrt{\varepsilon_0}\left(\mathrm{d}S_{ij}/\mathrm{d}S_{i0}\right)\left|E_{ij}\right|^2$ is the ray energy, E_{ij} is the enveloped electric-field amplitude, $\varepsilon_0 = 1 - n_\mathrm{e}/n_\mathrm{c}$ is the permittivity, n_e is the electron density, $n_\mathrm{c} = m_\mathrm{e}\omega_0^2/(4\pi e^2)$ is the critical density for light with frequency ω_0, m_e is the electron mass, e is the electron charge, $\mathrm{d}S_{i0}/\mathrm{d}S_{ij}$ is the ratio of the initial to current cross-sectional area of ray i (proportional to the ray intensity),

$$\xi_{ij}^{kl} = 5.88\times10^{-2}\frac{\lambda_0}{T_\mathrm{e}\left(1+3T_\mathrm{i}/ZT_\mathrm{e}\right)}\frac{n_\mathrm{e}}{n_\mathrm{c}}\frac{\omega_s}{\nu_\mathrm{IAW}}P\left(\eta_{ij}^{kl}\right),$$

$$P(\eta) = \frac{\left(\nu_\mathrm{IAW}/\omega_s\right)^2\eta}{\left(\eta^2-1\right)^{2s}+\left(\nu_\mathrm{IAW}/\omega_s\right)^2\eta^2},$$

$$\eta_{ij}^{lk} = \frac{\omega_{kl}-\omega_{ij}-\left(\mathbf{k}_{kl}-\mathbf{k}_{ij}\right)\cdot\mathbf{u}}{\omega_s},$$

λ_0 is the laser wavelength in vacuum (in microns), ω_{ij} is frequency of the ith ray at the jth location along its path in the lab frame and $\mathbf{k}_{ij}$ is the corresponding wave vector, ω_s is the acoustic frequency, ν_IAW is the IAW energy-damping rate, T_e (T_i) is the electron (ion) temperature in keV, Z is the ionization state of the ions, and $\mathbf{u}$ is the plasma flow velocity. α_{ij} is the local laser absorption length, which for electron–ion collisional absorption is equal to the group velocity over the

energy-damping rate $\alpha_{ij} = c\sqrt{\varepsilon_0}\, n_c \big/ \nu_{ei} n_e$ evaluated at the local plasma conditions.[6] The collisional damping rate is $\nu_{ei} = \sqrt{2\pi} e^4 Z^2 n_i \Lambda_{ei} \big/ \left(3\sqrt{m_e} T_e^{3/2}\right)$, where Λ_{ei} is the Coulomb logarithm.[33] Additional corrections related to laser absorption[34] and the temporal derivative of the background density profile[35] are included in ray-based models used in radiation–hydrodynamics codes, but these corrections were not used in the calculations here.

Equation (1) can be solved in numerous ways that all essentially come down to defining a procedure for breaking rays up into discrete segments and a procedure for mapping the energy of nearby rays onto a given section of a ray's path. The discretized version of Eq. (1) is

$$W_{i,j+1} = W_{ij} \exp\left[s_{ij} \left(-\frac{1}{\alpha_{ij}} + \sum_{kl} \frac{\xi_{ij}^{kl}}{\varepsilon_0} \frac{\mathrm{d}S_{k0}}{\mathrm{d}S_{kl}} W_{kl} \right) \right], \tag{2}$$

where s_{ij} is the length of the jth section of ray i's path. Equation (2) is a nonlinear system of equations that can be solved using fixed-point iteration,[36] but written in its current form it converges slowly because information about upstream changes along a ray propagate only one path step per iteration. The rate of convergence can be improved significantly by noting that

$$W_{ij} = W_{i0} \prod_{k=1}^{j} \frac{W_{ik}}{W_{i,k-1}},$$

where W_{i0} is the incident energy of the ith ray. Defining $\tilde{W}_{ik} \equiv W_{ik} \big/ W_{i,k-1}$, Eq. (2) can be written as a fixed-point iteration over the $\tilde{W}_{ij}$,

$$\tilde{W}_{i,j+1} = \exp\left[s_{ij} \left(-\frac{1}{\alpha_{ij}} + \sum_{kl} \frac{\xi_{ij}^{kl}}{\varepsilon_0} \frac{\mathrm{d}S_{k0}}{\mathrm{d}S_{kl}} W_{k0} \prod_{m=1}^{l} \tilde{W}_{km} \right) \right], \tag{3}$$

which propagates information along complete ray paths on each iteration and has a negligible increase in computational cost for a single iteration because the term in brackets can be stored in terms of the W_{kl} by taking the cumulative product along the ray paths after each iteration.

The ray trajectories of geometrical optics are determined by solving the coupled ordinary differential equations

$$\begin{aligned} \frac{\mathrm{d}\mathbf{x}}{\mathrm{d}\tau} &= \mathbf{k}, \\ \frac{\mathrm{d}\mathbf{k}}{\mathrm{d}\tau} &= \frac{1}{2} \nabla \varepsilon_0(\mathbf{x}), \end{aligned} \tag{4}$$

where the wave-vector magnitude is normalized to the vacuum value $\left(k = \sqrt{\varepsilon_0}\right)$. The solution to Eq. (4) is single valued at every point in ($\mathbf{x}$, $\mathbf{k}$) phase space, but it does not necessarily have a single-valued projection onto x space.[7] The divisions between regions of the phase space solution that have a single-valued projection onto x space occur at caustics, and when the solution is divided into distinct sections that individually have single-valued projections onto x space, the regions are referred to as "sheets." In ray-based CBET calculations, a ray from each sheet interacts with every other sheet at a given point in x space. Accordingly, the sum in Eq. (3) is restricted to rays on distinct sheets. The time-enveloped electric field is reconstructed from the eikonal solution by summing over sheets:

$$\mathbf{E}(\mathbf{x}) = \sum_{j \text{ sheets}} \mathbf{E}_j(\mathbf{x}) e^{i\phi_j(\mathbf{x})},$$

where ϕ_j is the phase corresponding to the field amplitude E_j. Additional subtleties are involved with ray-based CBET calculations at caustics because the electromagnetic-field amplitude in the eikonal approximation is singular. This topic will be discussed in a future publication (none of the ray-based calculations presented in this article included caustics).

The ray-based CBET calculations presented in this article discretized the ray trajectories on a Cartesian grid. Figure 151.12 shows a representation of the ray indexing scheme for two interacting beams, where rays 1 and 2 correspond to one beam and rays 3 and 4 correspond to the other beam. As an example of the indexing for the interactions, the crossing of rays 2 and 4 in grid cell 3 corresponds to the ray energies $W_{ij} \rightarrow W_{22}$ and $W_{kl} \rightarrow W_{42}$ with the interaction coefficient $\xi_{ij}^{kl} \rightarrow \xi_{22}^{42}$. Note that this example uses the ray energies at the grid cell entrance to calculate the interaction, but the numerical scheme converges to the same result if the midpoint or endpoint is used instead. Discretization onto a grid has the advantage of simplicity when determining the ray interactions because this step is reduced to simply looking at the other rays crossing a given grid cell, which also makes this step straightforward for parallel computation. The disadvantage, relative to interpolation-based

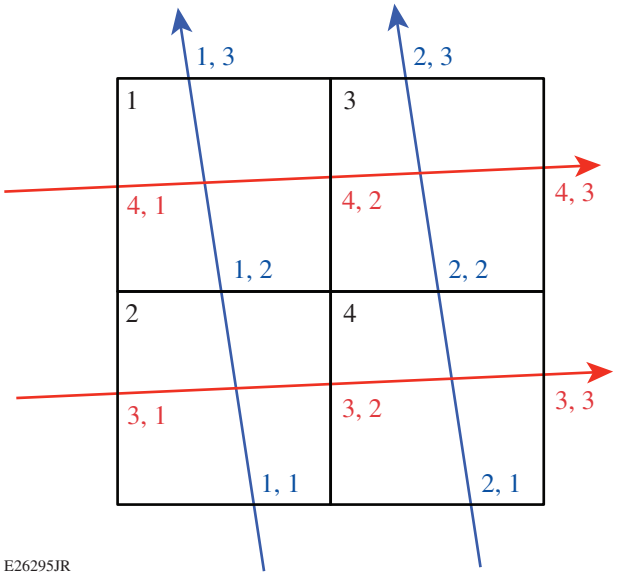

Figure 151.12
Indexing scheme for the ray paths and cross-beam energy transfer (CBET) grid for two interacting laser beams. The ray paths are divided according to their intersections with grid cell boundaries.

approaches, is that the rays must be dense enough that at least one ray from each sheet passes through each grid cell in the region where CBET is occurring for the solution to be valid.

1. Speckle in Ray-Based CBET

The laser beams used in ICF experiments pass through distributed phase plates (DPP's) that produce a speckle pattern consisting of many local minima and maxima at the focal plane.[13,19] The boundary condition for the electric field of a DPP beam injected at $z = 0$ can be modeled using

$$\mathbf{E}(x,y,z=0,t)=\sum_{\mathbf{k}}\left|\mathbf{E}(\mathbf{k},t)\right|e^{i(\mathbf{k}\cdot\mathbf{x}+\phi_{\mathbf{k}})}, \tag{5}$$

where the sum is over beamlets generated by the DPP with distinct wave vectors $\mathbf{k}$ and random phases ($\phi_{\mathbf{k}}$) (Ref. 18). The eikonal solution for the electromagnetic fields with this boundary condition cannot be calculated from a single sheet of rays because the wavefront is not locally a plane wave, but it is a superposition of many plane waves, so the field is obtained by taking the coherent sum of the ray-trace solution for each term in Eq. (5). For a given boundary condition, this gives the same solution for the fields as the wave-based calculation in the absence of CBET (in regions of space where the eikonal approximation is valid). The superposition solution used to calculate the fields cannot be applied to CBET, however, because the energy transfer is not linear in the electric field.[37]

To approximately include speckle effects in the ray-based CBET calculation, the local intensity variations were calculated using the superposition solution for the unperturbed electromagnetic fields and interpolated onto the ray trajectories used in the plane-wave calculation. The rest of the CBET calculation is identical to the plane-wave case with the intensity variations along the ray trajectories appearing as an additional term in the exponent in Eq. (3).

The primary increase in computational cost associated with the speckle model is that the speckles must be resolved on the CBET grid, which typically requires several-times-better spatial resolution for convergence than is needed for plane-wave beams. The transverse correlation length of a speckled beam is given by the product of the laser wavelength of the f number and the focusing optic ($f\lambda_0$) (Ref. 38), which is ~2 μm for the typical laser configurations used in ICF experiments (f/6.7 lenses and 0.351-μm light).[13]

We expect that a plane-wave approximation will be sufficient over some range of interaction configurations, and that the proposed model for including speckle effects in ray-based CBET calculations will extend this range, but a more-complete model is required to test the limits of these approximations.

LPSE

LPSE solves the time-enveloped Maxwell's equations coupled to the low-frequency plasma response in the fluid approximation. The plasma response is linearized around an inhomogeneous background density and flow velocity profile.[16] The time-enveloped wave equation for the electric field is

$$\frac{2i\omega_0}{c^2}\frac{\partial}{\partial t}\mathbf{E}+\nabla^2\mathbf{E}-\nabla(\nabla\cdot\mathbf{E})+\frac{\omega_0^2}{c^2}\varepsilon(\omega_0;\mathbf{x},t)\mathbf{E}=0,$$

where ε is the plasma dielectric function

$$\varepsilon(\omega_0;\mathbf{x},t)=1-\frac{\omega_{\mathrm{pe}}^2(\mathbf{x},t)}{\omega_0(\omega_0+i\nu_{\mathrm{ei}})}$$

and ν_{ei} is the electron–ion collision frequency. The physical electric field is given by $\tilde{\mathbf{E}}=\Re\left[\mathbf{E}(\mathbf{x},t)\exp(-i\omega_0 t)\right]$.

The equations for the low-frequency plasma response are

$$\left[\partial_t + \mathbf{U}_0(\mathbf{x})\cdot\nabla\right]\left(\frac{\delta n}{n_0}\right) = -\mathcal{W},$$

$$\left[\partial_t + \mathbf{U}_0(\mathbf{x})\cdot\nabla + 2\hat{\nu}_{\mathrm{IAW}}\right]\mathcal{W} = -\nabla^2\left[c_s^2\left(\frac{\delta n}{n_0}\right) + \frac{Ze^2}{4m_e m_i \omega_0^2}\left|\mathbf{E}\right|^2\right],$$

where $\mathcal{W} \equiv \nabla\cdot\delta\mathbf{U}$, $\mathbf{U}_0$ is the background flow profile, c_s is the sound speed, m_i is the ion mass, and $\hat{\nu}_{\mathrm{IAW}}$ is a phenomenological operator used to reproduce Landau damping of IAW's,[23] which is implemented by applying a constant damping of $\nu_{\mathrm{IAW}}/2$ in k space (the factor of 1/2 appears because ν_{IAW} is the energy damping rate, and the damping is applied to the wave amplitudes in *LPSE*). The density is $n_e(\mathbf{x},t) = n_0(\mathbf{x}) + \delta n(\mathbf{x},t)$ and the flow velocity is $\mathbf{U}(\mathbf{x},t) = \mathbf{U}_0(\mathbf{x}) + \delta\mathbf{U}(\mathbf{x},t)$. *LPSE* uses a total-field/scattered-field approach, where the laser beams are injected inside of the total-field region and the scattered-field region acts as an absorbing boundary. Further details of the numerical algorithm and benchmarking can be found in Refs. 16 and 39.

Comparison Between *LPSE* Numerical Solutions and the Ray-Based Model

This section is divided into subsections corresponding to interactions between linearly polarized beams in a plasma with a constant density and linearly varying flow, interactions between linearly polarized beams in ICF-relevant plasma conditions, and interactions between beams with polarization smoothing.

1. Homogeneous Plasma

Figure 151.13 shows the magnitude of the steady-state electric field from a 2-D *LPSE* simulation of the interaction between two counter-propagating speckled beams in a plasma with a linear flow velocity profile given by $v_{\mathrm{flow}}(x) = -\hat{x}c_s(0.005x + 1)$ and a constant density $n_e/n_c = 0.01$. The other plasma parameters were $T_e = 2$ keV, $T_i = 1$ keV, $Z = 3.1$, $A = 5.3$ (ion mass in amu), and $\nu_{\mathrm{IAW}}/\omega_s = 0.2$. The grid size was 80×240 μm^2 (3168×9504 grid cells) and the simulations were run until a steady state was established (4 ps). The speckle patterns correspond to f/6.7 lenses and were generated by launching 128 beamlets from each boundary with top-hat intensity distributions in wave-vector space [Eq. (5)] and fourth-order super-Gaussian distributions in physical space. The average initial intensity of the pump (seed) beam was 2×10^{15} W/cm^2 (1×10^{12} W/cm^2); both beams were polarized out of the plane (the average intensity is defined here as the peak intensity that a plane-wave beam would have for the same beam width and flux). The beams were launched 4 μm inside the simulation boundaries, and the outer 2 μm of the simulation grid were absorbing. The seed beam is not visible at its injection point (x = 36 μm) because of its low initial intensity, but it can be seen in the scattered region at the bottom of the image, where it exits with an average intensity of 3.2×10^{14} W/cm^2 corresponding to a gain of 5.8 (the gain is defined as the log of the incident seed-beam energy over the outgoing seed-beam energy).

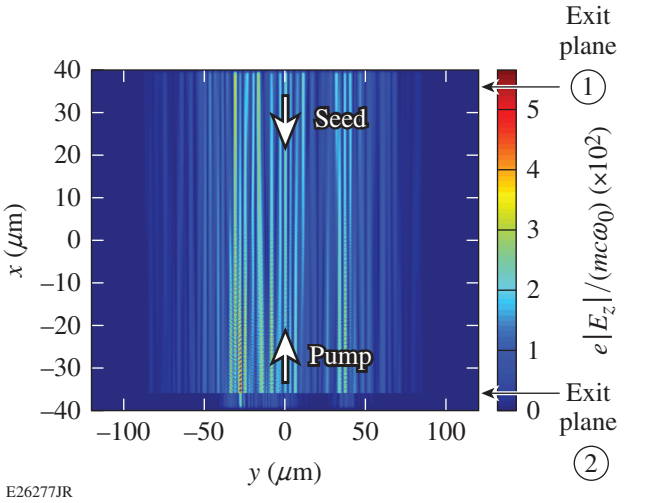

Figure 151.13
Magnitude of the time-enveloped electric field from an *LPSE* simulation of two counter-propagating beams with initial average intensities of 2×10^{15} W/cm^2 and 1×10^{12} W/cm^2.

Figure 151.14 shows lineouts of the *LPSE* field magnitude from Fig. 151.13 for the (a) pump and (b) seed beams at their respective exit planes (blue) and the corresponding result from the ray-based calculation (red). The two methods give nearly identical results for the field of the pump beam because it lost only 32% of its initial energy. The seed beam was amplified by more than 300×, and the two speckle patterns look completely different. Despite the significant differences in the structure of the calculated fields, the gain predicted by the ray-based model was only 0.8% lower than the wave-based calculation (the gain from the ray-based calculation using plane-wave beams was 38% lower). The ray-based calculation does not reproduce the detailed structure of the fields because the local variations in the direction of the wavefront were neglected when the magnitude of the fields was interpolated onto the ray trajectories from the plane-wave calculation. The interpolation procedure gives the correct statistical variations in the laser intensity, which is why the average CBET from the wave-based calculation was reproduced, but after energy is transferred, it is forced to fol-

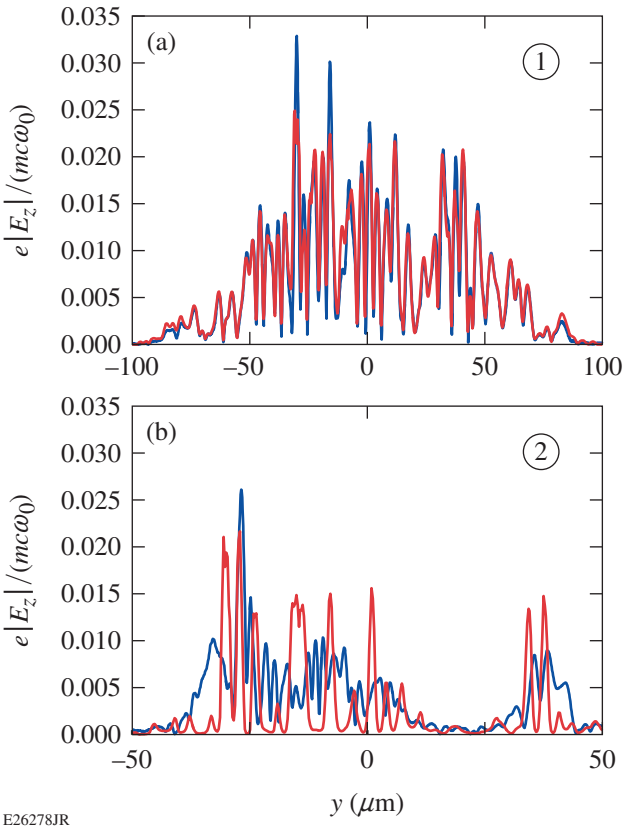

Figure 151.14
(a) Lineout of Fig. 151.13 at $x = 37$ μm (blue), which corresponds to the scattered field of the pump beam. The corresponding lineout from the ray-based calculation is shown in red. (b) Similar lineouts at $x = -37$ μm corresponding to the scattered field of the seed beam. Labels (1) and (2) correspond to the exit plane labels in Fig. 151.13.

low the ray trajectories whereas it follows the local wavefront in the wave-based calculation.

The advantage of the ray-based calculation is a significant reduction in computational cost. The *LPSE* calculation depicted in Fig. 151.13 took one hour on 792 CPU cores, while the corresponding ray-based calculation took only a few minutes on a desktop computer. For a given grid resolution, the computational cost of the *LPSE* calculation is proportional to the number of grid cells $O(N_G)$. The relevant computational requirement for the ray-based CBET calculation is the number of pairwise interactions between rays, which is $O\left(N_G N_B^2\right)$, where N_B is the number of laser beams. The grid resolution in *LPSE* is determined by the need to resolve the wavelength of light, while in the ray-based calculation, it is necessary to resolve spatial variations in the laser intensity and hydrodynamic conditions. Although the quadratic dependence on the number of laser beams causes the ray-based calculation to scale poorly to many beam systems, the grid resolution requirement is typically lower by a factor of 10 to 100 per dimension.

Figure 151.15 shows the results of a number of calculations similar to the one depicted in Fig. 151.13, where the pump intensity and the angle between the pump and seed beam were varied. The gains from the speckled-beam calculations are compared to those obtained in calculations that were identical except the speckled beams were replaced with plane-wave beams. For the case of counter-propagating beams, there is a difference of more than two e foldings in the energy gain for the speckled beams relative to the plane-wave beams at the highest pump intensity. At lower intensities, the difference diminishes. When the angle between the beams is increased, the difference between the plane-wave and speckled cases is reduced, and for more than 30° between the beams, there is no significant difference. Figure 151.15(d) shows the beam geometry used for these comparisons, which was chosen so that the peak of the CBET resonance was always at Mach 1.

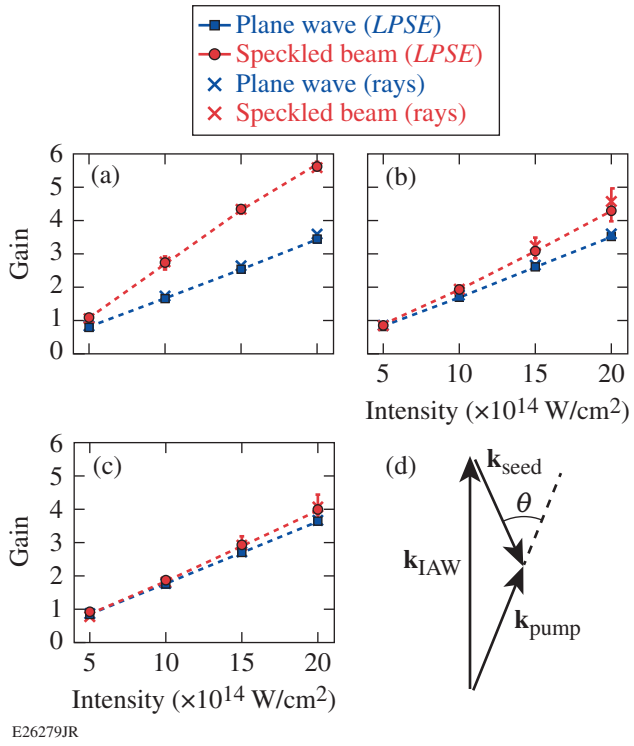

Figure 151.15
Gain as a function of laser intensity for beams separated by (a) 0°, (b) 15°, and (c) 30° relative to counter-propagating. The *LPSE* results are shown with red circles (speckled beams) and blue squares (plane-wave beams). The corresponding ray-trace results are shown with ×'s of the same color. The error bars correspond to the standard deviation in the gain over three different speckle realizations. (d) The beam geometry, where the wave vector of the resonant ion-acoustic wave (IAW) is antiparallel to the flow velocity gradient.

Figure 151.15 also shows the corresponding gains calculated using the ray-based CBET model. The ray-based model shows excellent agreement with the full-wave calculation for the interaction between plane waves, which indicates that the assumptions made in the ray-based model that are not related to beam speckle are valid in this configuration. The ray-based model also shows very good agreement with the speckled-beam results, and the calculated gains in the ray-based model always fall within one standard deviation of the *LPSE* gain averaged over different speckle realizations. The fact that the ray-based speckle model is in such good agreement with the wave-based calculations even when the plane-wave assumption gives a very poor approximation suggests that this is an extremely useful modification for including speckle effects in ray-based laser-plasma simulations. An additional benefit of the ray-based speckle model is that it inherently gives a more-realistic laser-energy deposition profile than a plane-wave approximation.

The maximum intensity used in Fig. 151.15 was chosen to keep the filamentation control parameter[38]

$$\left\langle \frac{P}{P_c} \right\rangle = 0.04 f^2 \left(\frac{n_e}{n_c} \right) \left(\frac{I_{14} \lambda_0^2}{T_e} \right) \tag{6}$$

below 1 (f is the f number and I_{14} is the laser intensity in units of 10^{14} W/cm^2). At the highest average intensity $\langle P/P_c \rangle = 0.22$. This is right at the limit where the highest-intensity speckles could potentially filament, but no filamentation was observed in the simulations depicted in Fig. 151.15. This was necessary for the comparison to the ray-based CBET model because the equations solved by *LPSE* implicitly include filamentation but the ray model does not.

The trends in Fig. 151.15 can be understood qualitatively by considering the average intensity over the CBET interaction region because the energy transfer is exponential in both the pump intensity and the interaction length. When the beams are counter-propagating, some of the speckles will see an increased pump intensity along the entire interaction length, giving exponentially larger gains, while the partially compensating reduction in the fraction of the beam profile that undergoes significant CBET is only a linear effect. When the angle between the beams is large, a given seed speckle will interact with many high- and low-intensity pump speckles, and the product of interaction length and pump intensity integrated over the interaction region averages out to the same value as for plane-wave beams. The same logic applies to the longitudinal extent of the speckles. In this example the speckles were longer than the interaction region, but as the length of the interaction region is increased relative to the length of the speckles, the plane-wave gains are eventually recovered regardless of the relative beam orientation.

2. Amplitude of Density Perturbations

In addition to modifying the CBET gain, most of the CBET between speckled beams happens in localized hot spots, which can lead to larger density perturbations than occur when plane-wave beams interact. Figure 151.16 shows the ratio of root-mean-square (rms) density perturbations for a speckled-beam simulation and the corresponding plane-wave simulation. The ratio is always larger than 1, indicating that the typical density perturbation is larger for the speckled-beam interaction than for the plane-wave interaction. Although *LPSE* does not include the relevant physics, nonlinear effects become important at large $\delta n/n$ and cause CBET to saturate.[15,38] Note that the amplitude of the density perturbations is insensitive to the relative beam angle, which shows that this is not simply a result of increased CBET.

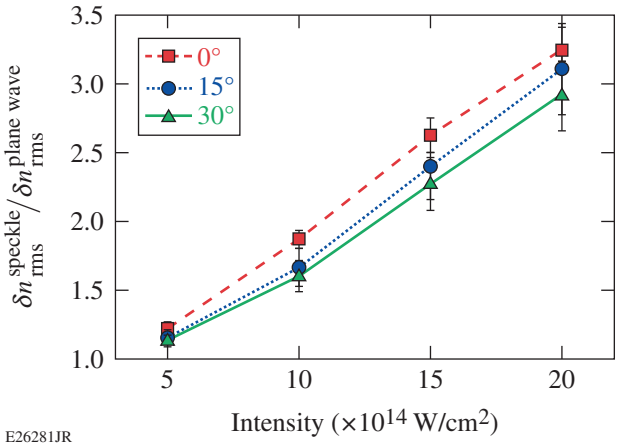

Figure 151.16
Root-mean-square (rms) density perturbation from *LPSE* simulations for the interaction between speckled beams divided by the rms density perturbation for the interaction between plane-wave beams. The rms perturbation was taken from the region $y = [-70,70]$ and $x = [0,30]$. The region was offset toward larger x so that the energy gain of the seed beam did not have a significant impact on the amplitude of the density perturbations. The error bars correspond to the standard deviation for three different speckle realizations.

To test the qualitative impact of nonlinear saturation, the *LPSE* simulations depicted in Fig. 151.15 were repeated with a clamp on the amplitude of the density perturbations $|\delta n/n| \leq 0.01$. This clamp was chosen to be more restrictive than the expected $|\delta n/n| \sim 0.1$ threshold[38] to exaggerate the impact of

nonlinear saturation. Previous studies using a code similar to *LPSE* have shown that an even more restrictive clamp on $\delta n/n$ is required to obtain quantitative agreement with scattered-light measurements in indirect-drive ICF experiments.[40] Figure 151.17 compares the *LPSE* gains plotted in Fig. 151.15 and the clamped simulations (only one speckle realization was simulated at each condition and compared to the corresponding simulation that used the same seed for random phase generation). At all relative beam angles and intensities, the perturbation-limited results are essentially indistinguishable for the plane-wave simulations, but in the speckled-beam simulations, the clamp reduced the amount of CBET significantly.

3. OMEGA Implosions

Although the subscale calculations presented in the previous section show that speckles can increase the CBET gain, the effect on laser absorption in direct-drive ICF experiments is expected to be small for two main reasons: (1) the single-beam intensities in ICF experiments are usually about an order of magnitude lower than the lowest intensity from Fig. 151.15; and (2) in a 3-D spherical implosion, the fraction of the solid angle that corresponds to nearly counter-propagating rays is small. The effect could be greater in indirect-drive ICF where many of the beams are nearly co-propagating although the single-beam intensities are still relatively low.[15]

Figure 151.18 shows the steady-state magnitude of the electric-field envelope and the corresponding ion-density perturbations for plane-wave and speckled-beam 2-D *LPSE* simulations of two *f*/6.7 *s*-polarized beams interacting in a realistic direct-drive ICF plasma profile from the 1-D radiation–hydrodynamics code *LILAC*.[41] The beams were injected at normal incidence 22 μm inside the minimum x and y boundaries. The

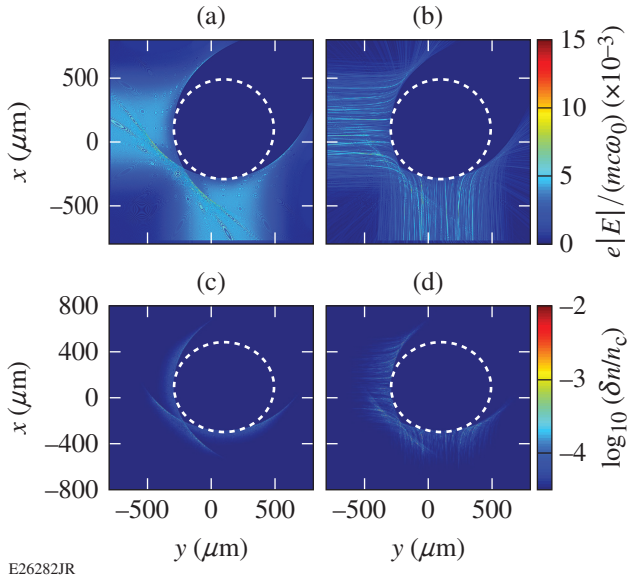

Figure 151.18
Amplitude of the electric-field envelope in a full-scale two-beam *LPSE* simulation (at 12 ps) using ICF-relevant plasma conditions with (a) plane-wave beams and (b) speckled beams at initial intensities of 2×10^{14} W/cm^2. The corresponding density perturbations are shown in (c) and (d). The critical density is denoted by white dashed circles. The electromagnetic-field (density-perturbation) grid was 40,000 × 40,000 (80,000 × 80,000) cells. The small-scale rings in the fields are aliasing artifacts associated with the wavelength-scale perturbations on the high-resolution grids.

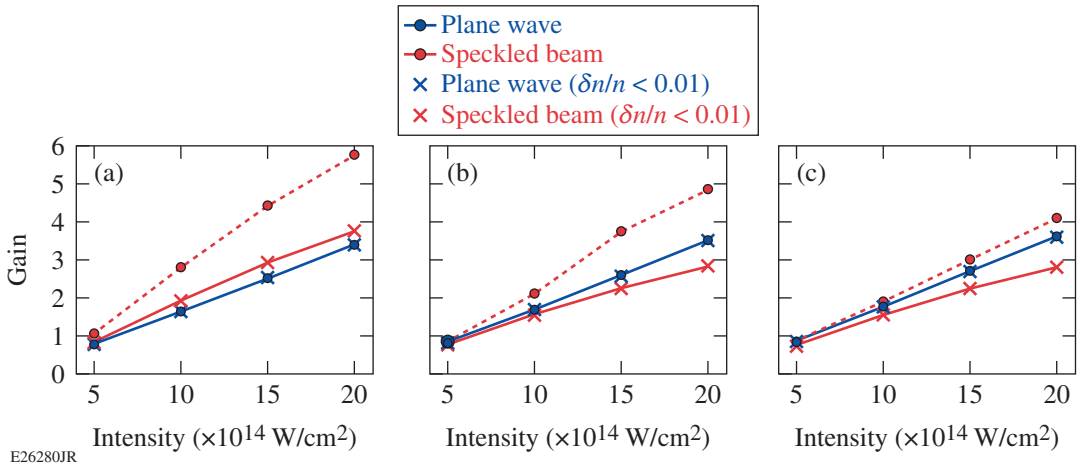

Figure 151.17
Gain as a function of pump intensity from *LPSE* simulations for speckled beams (red) and plane-wave beams (blue) with (circles) and without (crosses) a limiter of $|\delta n/n| \leq 0.01$ for beams separated by (a) 0°, (b) 15°, and (c) 30°.

angle between the beams was set to 90° because it gives nearly maximal CBET.[10] In Fig. 151.18(a), the field amplitude of the incident beams is visibly reduced after they cross through the caustic of the other beam. Because the outgoing portion of the beams gain energy from the incident beams, this interaction leads to a reduction in the total laser absorption. The density perturbations shown in Figs. 151.18(a) and 151.18(b) indicate where CBET occurs. The dominant interaction regions are in the beam caustics crossing through the middle of the other incoming beam and near to the critical density where the beams are reflected. The interaction at near-critical density is seeded by the reflected beam and is referred to as self-CBET. Self-CBET is typically not as energetically important as the interaction between distinct beams because it occurs at high densities and most of the energy that is transferred is still absorbed. The speckled-beam calculations are qualitatively similar to the plane-wave calculations in terms of where CBET occurs with the additional restriction that most of the CBET occurs in high-intensity speckles.

Two-beam simulations were performed at two different single-beam intensities, 1×10^{14} W/cm^2 and 2×10^{14} W/cm^2. These intensities are higher than the single-beam intensities in ICF experiments, but there are many more beams interacting in that case. The intensities were chosen to give a non-negligible reduction in laser absorption resulting from CBET while staying below the filamentation threshold. In the absence of CBET, the percentage of the incident laser energy that was absorbed by the plasma in the simulations similar to those shown in Fig. 151.18 was 94% regardless of beam type/intensity. For laser intensities of 1×10^{14} W/cm^2, the absorption was 90.5% (89.2%) for the plane-wave (speckled) beams, and for laser intensities of 2×10^{14} W/cm^2, the absorption was 85.4% (82.8%) for the plane-wave (speckled) beams. In both cases the reduction in laser absorption was ~30% larger for the speckled-beam simulations (relative to the no-CBET simulations). However, this configuration should significantly overestimate the impact of speckles because of the high single-beam intensities.

To test the effect of using many lower-intensity beams, 2-D quarter-scale, 16-beam *LPSE* simulations were run using single-beam intensities of 4×10^{14} W/cm^2. The beams were injected uniformly at 22.5° increments. In the quarter-scale, 16-beam configuration, the plane-wave simulation had 67% absorption and the speckled-beam simulation had 66.8% absorption (98% absorption without CBET). Despite the significant reduction in absorption caused by CBET, the plane-wave and speckled-beam simulations had nearly the same total laser absorption, which suggests that the use of many lower-intensity beams smooths out single-beam speckle effects but does not diminish the impact of CBET.[30] Accordingly, a plane-wave approximation is expected to be sufficient for calculations of CBET between linearly polarized beams in many-beam direct-drive ICF applications.

4. Polarization Smoothing

Polarization smoothing is typically accounted for in ray-based CBET models by multiplying the gain coefficient calculated for parallel-polarized beams [ξ_{ij}^{kl} in Eq. (3)] by a factor of $\left(1+\cos^2\theta\right)/4$, where θ is the angle between the interacting rays. This factor is obtained by assuming random relative polarizations of the interacting beams and spatially averaged incoherence between the two polarization components of each beam.[15] This approximation can be tested by comparing the ray model to *LPSE* simulations, which have full polarization effects.

Figure 151.19 shows the results of a series of comparisons between the *LPSE* and the ray-based model using polarization smoothing and two different f numbers (6.7 and 3) at pump-beam intensities of 5×10^{14} W/cm^2. The plasma conditions were the same as discussed in **Homogeneous Plasma** (p. 132) (homogeneous density and constant flow velocity gradient), and polarization smoothing was obtained by splitting the energy of the incident beams evenly between s and p polarizations. The two polarizations had statistically independent speckle realizations. The gain calculated by *LPSE* was higher than the gain in the ray-based model for all but the orthogonal *f*/3 beams. The gains are higher for the *f*/6.7 because their longitudinal correlation length ($2\pi f^2\lambda_0 \approx 100$ μm) is longer than the interaction volume,[38] so the assumption of incoherence between the polarization components when averaged over the

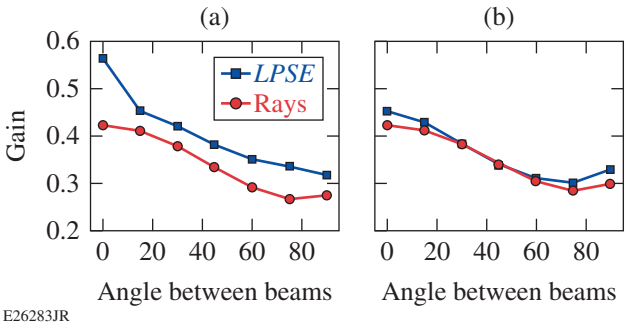

Figure 151.19
The CBET gain for a seed beam interacting with a pump beam at an intensity of 5×10^{14} W/cm^2. Both beams were smoothed by polarization with the energy split evenly between s and p polarization. The f numbers of the beams were (a) 6.7 and (b) 3. The wave-based (ray-based) results are shown in blue (red).

interaction region is violated. The speckle length for the *f*/3 beams is expected to be in better agreement with the ray-based calculation because of the reduced speckle length (~20 μm).

There is a significant difference between the wave-based and ray-based results shown in Fig. 151.19, even though the intensity was only 5×10^{14} W/cm^2, and the gains were much lower than for the corresponding linearly polarized calculations. The discrepancy between *LPSE* and the ray-based model in the case where the beams are orthogonal is readily explained by noting that the in-plane components of the beams' polarizations do not interact, and the out-of-plane components have the same interaction as two linearly polarized beams with half of the energy. If the average intensity amplification for the linearly polarized case is written $I/I_0 = e^G$, then this should give $I/I_0 = (1 + e^{G/2})/2$, whereas using the factor of $(1 + \cos^2\theta)/4$ gives $I/I_0 = e^{G/4}$.

In the case of counter-propagating beams, the difference can be understood by using a simple square-wave model, where a speckled beam is treated as having a beam spot profile with twice the average intensity over half of the beam profile and zero intensity over the rest. If the speckles are random, the interaction between two linearly polarized counter-propagating beams will have the same statistical properties as the interaction between the two beam profiles depicted in Fig. 151.20(a). The interaction can be broken up into four situations that occur with equal probability, only one of which results in any CBET (it is assumed here that the speckles are much longer than the interaction region). The expected intensity amplification is $(I/I_0)_{\text{speckle}} = (1 + e^{2G})/2$. Comparing this to the amplification using the average intensity $(I/I_0)_{\text{avg}} = e^G$, the first nonvanishing term in the Taylor expansion of the difference is $(I/I_0)_{\text{speckle}} - (I/I_0)_{\text{avg}} \approx G^2/2$, quadratic in the gain.

The same model can be used for polarization-smoothed beams, but each of the beams must also be split into two orthogonal polarizations. There are now four equally probable combinations of amplitude and polarization within each beam and 16 possible types of interactions between beams that are depicted in Fig. 151.20(b). Adding up the various contributions to the amplification gives $(I/I_0)_{\text{PS}} = 1/2 + (3e^G + e^{2G})/8$. This should be compared to the amplification that is used in the ray-based model, $(I/I_0)_{\text{PS(rays)}} = e^{G/2}$, which to leading order gives $(I/I_0)_{\text{PS}} - (I/I_0)_{\text{PS(rays)}} \approx G/8$. The lowest-order correction is linear in G, consistent with the deviation between the wave- and ray-based calculations occurring at lower gains for polarization-smoothed beams than for linearly polarized beams.

The comparisons shown in Fig. 151.19 are useful for illustrating why CBET between polarization-smoothed beams might not agree with ray-based calculations, but they do not represent a fair comparison because the relative polarizations of the interacting beams were not random. Figure 151.21 shows the results of calculations where the initial polarization of the two beams was chosen randomly (and independently) before applying phase plates and polarization smoothing. For the *f*/6.7 beams, the average gain over realizations still differs from the ray-based model because of the large speckle length. The calculations using *f*/3 beams are in good agreement with the ray-based model, which suggests that the gain multiplier used to correct for polarization smoothing in the ray-based models is accurate when the underlying assumptions are satisfied.

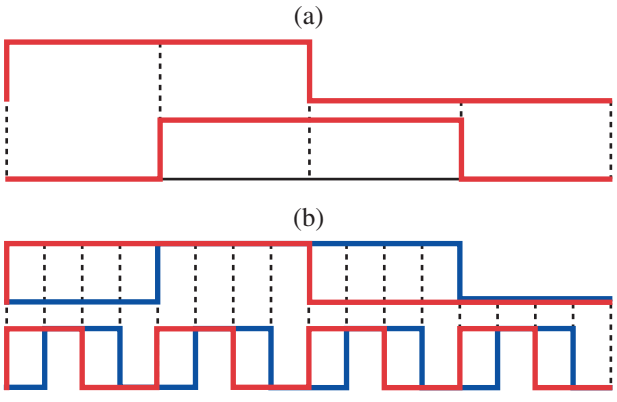

Figure 151.20
Beam profiles with the same statistical properties as a square-wave speckle model for (a) linearly polarized beams and (b) polarization-smoothed beams split evenly between *s* and *p* polarization.

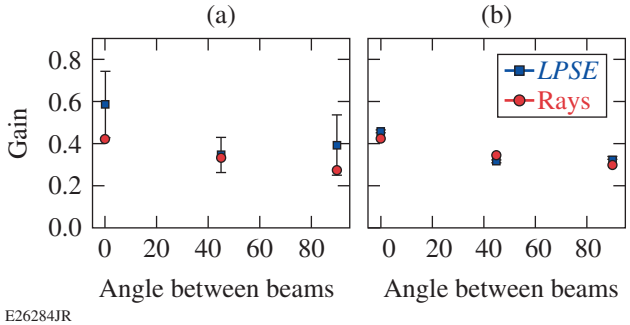

Figure 151.21
The average and standard deviations in the gain for different realizations of the relative beam polarization and various angles between the pump and seed beams (blue points with error bars). Twelve different realizations were used for (a) the *f*/6.7 beams and five realizations were used for (b) the *f*/3 beams. The red points show the corresponding results from ray-based calculations.

The discrepancy at larger *f* numbers could be significant in ICF experiments because the gradient scale lengths are typically comparable to the speckle length of the drive beams. In Fig. 151.18(c), the majority of the CBET is occurring in the "wings" in the lower left part of the image, where the caustic of the outgoing beam gains energy as it crosses the center of the incoming beam. The spatial extent of this transfer region is $\lesssim$100 μm.

Summary

The impact of beam speckle and polarization smoothing on CBET was studied using the full-wave LPI code *LPSE*. The results were compared to ray-based calculations using a code that is based on the ray models used to simulate ICF experiments. The ray-based model tends to underpredict the amount of CBET when the assumption of spatially averaged incoherence over the length of the interaction region is violated. A ray-based speckle model was presented that gives excellent agreement with the wave-based calculations over a broad range of gains and relative beam angles.

At all relative angles, the CBET interaction between speckled beams generates larger rms density perturbations than the corresponding plane-wave interaction. These enhanced density perturbations could lead to the earlier onset of nonlinear saturation of CBET between speckled beams. The single-beam intensities in ICF experiments are not sufficient for this effect to be significant, but it could play a role in many-beam interactions.

For linearly polarized beams, the large gain ($\gtrsim$1) and small relative beam angle that were required to see a significant difference between the plane-wave and speckled-beam calculations suggest that a plane-wave approximation should not result in a significant error in laser-absorption calculations for direct-drive ICF. This conclusion is supported by *LPSE* simulations in hydrodynamic profiles relevant to direct-drive ICF that showed a modest reduction in laser absorption for two-beam interactions and almost no reduction in laser absorption for a 16-beam interaction. For polarization-smoothed beams, there is a significant difference between the wave- and ray-based results at modest gains and over a broader range of relative beam angles, which could have an impact on CBET calculations for ICF.

ACKNOWLEDGMENT

This material is based upon work supported by the Department of Energy National Nuclear Security Administration under Award Number DE-NA0001944, the University of Rochester, and the New York State Energy Research and Development Authority.

REFERENCES

1. R. S. Craxton, K. S. Anderson, T. R. Boehly, V. N. Goncharov, D. R. Harding, J. P. Knauer, R. L. McCrory, P. W. McKenty, D. D. Meyerhofer, J. F. Myatt, A. J. Schmitt, J. D. Sethian, R. W. Short, S. Skupsky, W. Theobald, W. L. Kruer, K. Tanaka, R. Betti, T. J. B. Collins, J. A. Delettrez, S. X. Hu, J. A. Marozas, A. V. Maximov, D. T. Michel, P. B. Radha, S. P. Regan, T. C. Sangster, W. Seka, A. A. Solodov, J. M. Soures, C. Stoeckl, and J. D. Zuegel, Phys. Plasmas **22**, 110501 (2015).

2. S. Atzeni and J. Meyer-ter-Vehn, *The Physics of Inertial Fusion: Beam Plasma Interaction, Hydrodynamics, Hot Dense Matter*, International Series of Monographs on Physics (Clarendon Press, Oxford, 2004).

3. V. N. Goncharov, T. C. Sangster, R. Betti, T. R. Boehly, M. J. Bonino, T. J. B. Collins, R. S. Craxton, J. A. Delettrez, D. H. Edgell, R. Epstein, R. K. Follet, C. J. Forrest, D. H. Froula, V. Yu. Glebov, D. R. Harding, R. J. Henchen, S. X. Hu, I. V. Igumenshchev, R. Janezic, J. H. Kelly, T. J. Kessler, T. Z. Kosc, S. J. Loucks, J. A. Marozas, F. J. Marshall, A. V. Maximov, R. L. McCrory, P. W. McKenty, D. D. Meyerhofer, D. T. Michel, J. F. Myatt, R. Nora, P. B. Radha, S. P. Regan, W. Seka, W. T. Shmayda, R. W. Short, A. Shvydky, S. Skupsky, C. Stoeckl, B. Yaakobi, J. A. Frenje, M. Gatu-Johnson, R. D. Petrasso, and D. T. Casey, Phys. Plasmas **21**, 056315 (2014).

4. I. V. Igumenshchev, W. Seka, D. H. Edgell, D. T. Michel, D. H. Froula, V. N. Goncharov, R. S. Craxton, L. Divol, R. Epstein, R. Follett, J. H. Kelly, T. Z. Kosc, A. V. Maximov, R. L. McCrory, D. D. Meyerhofer, P. Michel, J. F. Myatt, T. C. Sangster, A. Shvydky, S. Skupsky, and C. Stoeckl, Phys. Plasmas **19**, 056314 (2012).

5. P. Michel *et al*., Phys. Plasmas **17**, 056305 (2010).

6. W. L. Kruer, *The Physics of Laser Plasma Interactions*, Frontiers in Physics, Vol. 73, edited by D. Pines (Addison-Wesley, Redwood City, CA, 1988).

7. E. R. Tracy *et al*., *Ray Tracing and Beyond: Phase Space Methods in Plasma Wave Theory* (Cambridge University Press, Cambridge, England, 2014).

8. R. W. Short and E. A. Williams, Phys. Rev. Lett. **47**, 337 (1981).

9. C. J. Randall, J. R. Albritton, and J. J. Thomson, Phys. Fluids **24**, 1474 (1981).

10. D. H. Edgell, R. K. Follett, I. V. Igumenshchev, J. F. Myatt, J. G. Shaw, and D. H. Froula, Phys. Plasmas **24**, 062706 (2017).

11. A. K. Davis, D. Cao, D. T. Michel, M. Hohenberger, D. H. Edgell, R. Epstein, V. N. Goncharov, S. X. Hu, I. V. Igumenshchev, J. A. Marozas, A. V. Maximov, J. F. Myatt, P. B. Radha, S. P. Regan, T. C. Sangster, and D. H. Froula, Phys. Plasmas **23**, 056306 (2016).

12. P. Michel *et al*., Phys. Plasmas **20**, 056308 (2013).

13. T. R. Boehly, R. S. Craxton, T. H. Hinterman, J. H. Kelly, T. J. Kessler, S. A. Kumpan, S. A. Letzring, R. L. McCrory, S. F. B. Morse, W. Seka, S. Skupsky, J. M. Soures, and C. P. Verdon, Rev. Sci. Instrum. **66**, 508 (1995).

14. T. R. Boehly, V. A. Smalyuk, D. D. Meyerhofer, J. P. Knauer, D. K. Bradley, R. S. Craxton, M. J. Guardalben, S. Skupsky, and T. J. Kessler, J. Appl. Phys. **85**, 3444 (1999).

15. D. T. Michel, A. V. Maximov, R. W. Short, J. A. Delettrez, D. Edgell, S. X. Hu, I. V. Igumenshchev, J. F. Myatt, A. A. Solodov, C. Stoeckl, B. Yaakobi, and D. H. Froula, Phys. Plasmas **20**, 055703 (2013).

16. J. F. Myatt, R. K. Follett, J. G. Shaw, D. H. Edgell, D. H. Froula, I. V. Igumenshchev, and V. N. Goncharov, Phys. Plasmas **24**, 056308 (2017).

17. R. J. Adler, *The Geometry of Random Fields, Classics in Applied Mathematics* (Society for Industrial and Applied Mathematics, Philadelphia, 2010).

18. H. A. Rose and D. F. DuBois, Phys. Fluids B **5**, 590 (1993).

19. J. Garnier, Phys. Plasmas **6**, 1601 (1999).

20. J. Garnier and L. Videau, Phys. Plasmas **8**, 4914 (2001).

21. H. A. Rose and D. F. DuBois, Phys. Fluids B **5**, 3337 (1993).

22. A. J. Schmitt and B. B. Afeyan, Phys. Plasmas **5**, 503 (1998).

23. H. A. Rose, Phys. Plasmas **3**, 1709 (1996).

24. D. E. Hinkel *et al*., Phys. Plasmas **6**, 571 (1999).

25. H. A. Rose, Phys. Plasmas **2**, 2216 (1995).

26. V. T. Tikhonchuk, C. Labaune, and H. A. Baldis, Phys. Plasmas **3**, 3777 (1996).

27. A. V. Maximov, J. Myatt, W. Seka, R. W. Short, and R. S. Craxton, Phys. Plasmas **11**, 2994 (2004).

28. P. Michel *et al*., Phys. Plasmas **16**, 042702 (2009).

29. G. Raj and S. Hüller, Phys. Rev. Lett. **118**, 055002 (2017).

30. H. A. Rose and D. F. DuBois, Phys. Fluids B **4**, 252 (1992).

31. A. Colaïtis *et al*., Phys. Plasmas **23**, 032118 (2016).

32. I. V. Igumenshchev, D. H. Edgell, V. N. Goncharov, J. A. Delettrez, A. V. Maximov, J. F. Myatt, W. Seka, A. Shvydky, S. Skupsky, and C. Stoeckl, Phys. Plasmas **17**, 122708 (2010).

33. J. D. Huba, NRL Plasma Formulary, Naval Research Laboratory, Washington, DC, Report NRL/PU/6790-94-265 (1994).

34. A. B. Langdon, Phys. Rev. Lett. **44**, 575 (1980).

35. T. Dewandre, J. R. Albritton, and E. A. Williams, Phys. Fluids **24**, 528 (1981).

36. L. R. Scott, *Numerical Analysis* (Princeton University Press, Princeton, NJ, 2011).

37. H. A. Rose and S. Ghosal, Phys. Plasmas **5**, 1461 (1998).

38. D. Pesme, S. Hüller, J. Myatt, C. Riconda, A. Maximov, V. T. Tikhonchuk, C. Labaune, J. Fuchs, S. Depierreux, and H. A. Baldis, Plasma Phys. Control. Fusion **44**, B53 (2002).

39. J. F. Myatt, J. G. Shaw, R. K. Follett, D. H. Edgell, D. H. Froula, I. V. Igumenshchev, and V. N. Goncharov, "*LPSE*—A 3-D Wave-Based Model of Cross-Beam Energy Transfer in Laser-Irradiated Plasmas," to be submitted to the Journal of Computational Physics.

40. P. Michel *et al*., Phys. Rev. E **83**, 046409 (2011).

41. J. Delettrez, R. Epstein, M. C. Richardson, P. A. Jaanimagi, and B. L. Henke, Phys. Rev. A **36**, 3926 (1987).

Origins and Scaling of Hot-Electron Preheat in Ignition-Scale Direct-Drive Inertial Confinement Fusion Experiments

Direct-drive inertial confinement fusion (ICF)[1,2] is one of two laser-based techniques being pursued for achieving controlled nuclear fusion at the 1.8-MJ National Ignition Facility (NIF).[3] In direct-drive hot-spot ignition designs, laser ablation of a spherical shell drives the implosion and compression of a cryogenic deuterium–tritium (DT) fuel layer, into which a fusion burn wave propagates after first being initiated in a central, low-density hot spot.[4] To achieve ignition, the fuel must be compressed to an areal density greater than 0.3 g/cm^2, which can be achieved by keeping the pressure close to the Fermi-degenerate pressure. Preheat of the DT fuel by suprathermal electrons generated by laser–plasma instabilities (LPI's) increases this pressure, degrades compression, and inhibits ignition. Consequently, control of LPI suprathermal (or "hot")-electron production is critical for a successful implosion.

Stimulated Raman scattering (SRS)[5–8] and two-plasmon decay (TPD)[9] are two instabilities that are capable of generating hot electrons since they both excite electrostatic waves in the plasma that provide accelerating fields. SRS entails the decay of a laser light wave into an electron plasma wave and a scattered-light wave at densities at or below one quarter of the critical density of the laser, while TPD is the decay of a laser light wave into two electrostatic plasma waves (plasmons) near the quarter-critical density. Previous studies of SRS and TPD have examined single-beam thresholds,[9,10] quantified suprathermal electron production,[6,11,12] explored collective multibeam processes,[13–18] and investigated the spatial properties of TPD[19] and the angular distribution of the resulting hot electrons[20]—an important consideration when computing preheat. SRS imposes serious constraints on ignition designs in the indirect-drive approach to ICF because of the high single-beam intensities and large volumes of quasi-homogeneous plasma that are required when using gas-filled hohlraums.[21] To date, direct-drive experiments have shown minimal SRS resulting from lower single-beam intensities and density scale lengths shorter than ignition scale.

The low level or absence of observable SRS reflectivity in subscale (density scale length $L_n \sim 150$ μm and electron temperature $T_e \sim 2$ keV) direct-drive implosions on the OMEGA laser [maximum laser energy (power) of 30 kJ (30 TW)] (Ref. 22) has focused work instead on the physics, scaling, and mitigation of TPD, which is observed close to threshold.[15] Direct-drive implosions on OMEGA are known to excite collective multibeam TPD, which, at the highest-available irradiation intensities, converts as much as 1% of the incident laser energy to hot electrons. This level of hot electrons is close to what can be tolerated in direct-drive–ignition designs, and the scaling of hot-electron production to ignition scale has not yet been assessed. Ignition-scale direct-drive implosions[23] will have much longer density scale lengths ($L_n \sim 600$ μm) and hotter coronal electron temperatures ($T_e \lesssim 5$ keV), placing the interaction conditions in a previously unexplored regime. Until the experiments described herein, carried out on a MJ-scale facility, it was not possible to simultaneously achieve the density scale length, laser intensity, electron temperature, and transverse plasma dimensions that are characteristic of ignition-scale direct-drive implosions.

This article presents the first exploration of the LPI origins, scaling, and possible mitigation of hot electrons under direct-drive ignition-relevant conditions. These new observations indicate the dominance of SRS over TPD, a result not previously anticipated, with significant implications for direct-drive–ignition designs.

Planar targets were irradiated from one side with 351-nm laser light using a subset of the NIF's 192 beams, with 1-D smoothing by spectral dispersion[24] at 90 GHz. These beams are arranged into cones that share a common angle with respect to the polar axis. There are four such cones in each hemisphere: the "inner" cones have angles of 23.5° and 30° (32 beams in each hemisphere), while the "outer" cones have angles of 44.5° and 50° (64 beams in each hemisphere). All targets described here were irradiated using beams in the southern hemisphere. The targets were thick CH (or Si) disks with a 4.4-mm diameter and a 1.2-mm (or 0.75-mm) thickness, oriented toward a polar angle between 0° and 30°. Planar targets were chosen because they are the only way, currently, to achieve direct-drive ignition-relevant plasma conditions, while using a reduced laser energy (~200 kJ)

on the NIF. The use of planar targets also reduces the level of cross-beam energy transfer[25] relative to spherical targets.

Time-resolved SRS diagnostics, with or without spectral resolution (400 to 750 nm), were located at polar angles of 23.5°, 30°, and 50° (Ref. 26), as shown in Fig. 151.22. The targets were irradiated with laser pulses of ≤8-ns duration at vacuum overlapped intensities of $\leq 3 \times 10^{15}$ W/cm^2. The plasma evolution was simulated using the 2-D radiation–hydrodynamics code *DRACO*[27] for comparison with experimental observations. The *DRACO* predictions for the density scale lengths and electron temperatures, in the vicinity of the quarter-critical density $n_e = n_c/4$ [where n_e is the electron density and n_c is the critical density for the laser wavelength λ_0 (in μm), with $n_c \approx 1.1\times10^{21}\,\lambda_0^{-2}\,\mathrm{cm}^{-3}$] were $L_n \sim 500$ to 700 μm and $T_e \sim$ 3 to 5 keV, respectively. *DRACO* simulations calculate that the laser intensity is attenuated by ~50% on reaching the quarter-critical surface as a result of collisional absorption.

A time-resolved scattered-light spectrum obtained from NIF shot N160420-003 is shown in Fig. 151.22(a). It displays a narrow, intense feature at a wavelength slightly above 702 nm ($2\lambda_0$). A local (i.e., near $n_c/4$) electron temperature measurement can be obtained from this feature from the relation $T_{e,\mathrm{keV}} = \Delta\lambda_{\mathrm{nm}}/3.09$ (Ref. 28), where $\Delta\lambda$ is the shift of the spectral peak from $2\lambda_0$ after corrections for Doppler and Dewandre shifts[29] have been applied.[30] The electron temperature inferred from this technique is $T_e = 4.5\pm0.2$ keV. The *DRACO* calculations predict a consistent temperature (4.5 keV), giving confidence in the numerical modeling of the corona and indicating that ignition-relevant temperatures have been achieved. As a result of refraction effects, this spectral feature is emitted only perpendicularly to the density gradient (i.e., along the target normal),[19] and its observation required that the target be tilted to face the diagnostic [Fig. 151.22(d)]. For this reason, it is not seen in Figs. 151.22(b) or 151.22(c).

Importantly, this feature demonstrates significant differences relative to the near-$2\lambda_0$ spectrum obtained at smaller scales on OMEGA. A typical half-harmonic spectrum from a spherical implosion experiment (shot 80802) on OMEGA is shown in the inset of Fig. 151.22(a), sharing the same wavelength scale as the NIF spectrum. The characteristic half-harmonic features that are red- and blue-shifted with respect to $2\lambda_0$ seen

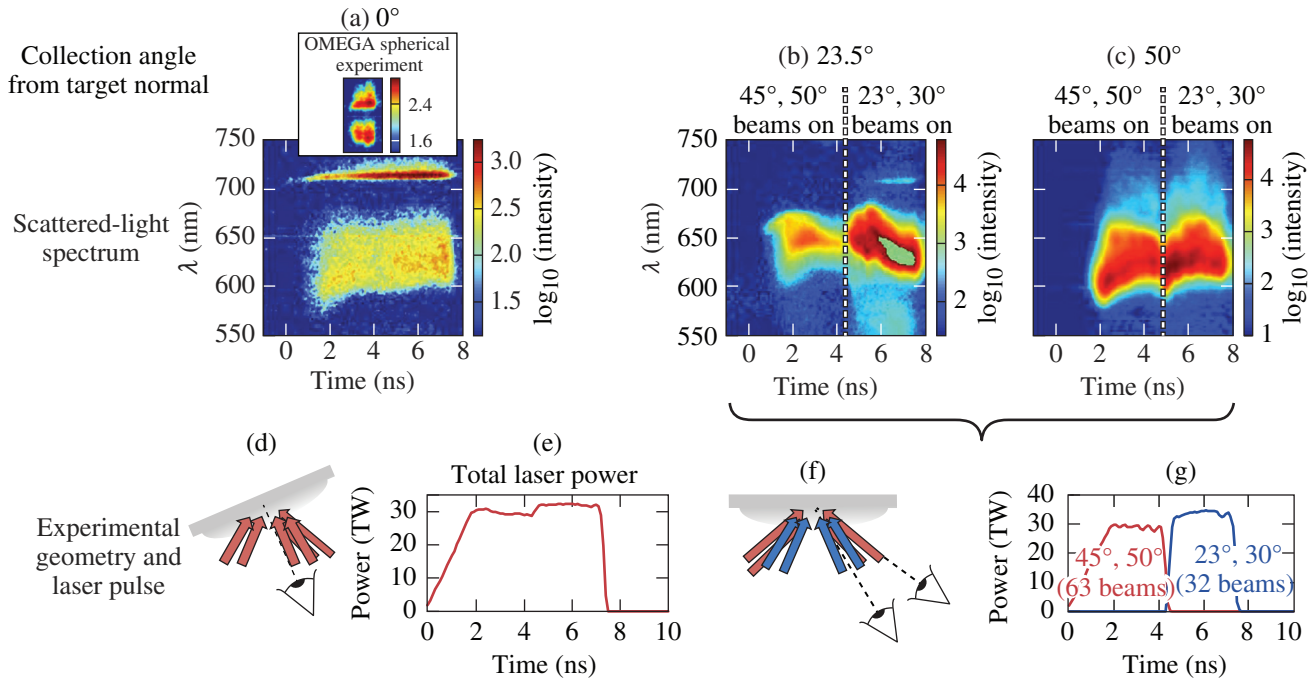

Figure 151.22
Time-resolved scattered-light spectra at collection angles of (a) 0°, (b) 23.5°, and (c) 50° relative to the target normal. These images were obtained in two CH target experiments. The image in (a) corresponds to an experiment (d) with the target oriented toward a streaked spectrometer and (e) irradiated by a ramp-flat pulse at a peak quarter-critical laser intensity of 1.3×10^{15} W/cm^2. The images in (b) and (c) correspond to an experiment (f) with the target oriented toward the south pole of NIF and was (g) irradiated first by beams at incidence angles of 45° and 50°, followed by beams at 23° and 30°. The streaked spectrum from a spherical-geometry experiment on OMEGA [inset in (a)] is contrasted to the image in (a).

in the OMEGA experiment are a definitive diagnostic of the presence of TPD.[31] The doublet arises by processes such as inverse resonance absorption, inverse parametric decay, and self-Thomson scattering that convert the up- and down-shifted TPD daughter plasma waves into transverse (light) waves.[28] The lack of a blue-shifted half-harmonic and the narrowness of the red-shifted feature seen in the NIF experiment is a strong indication that different physical processes are occurring at the quarter-critical surface. The sharp feature observed in the NIF experiment is a well-known signature of the absolute Raman instability that can occur at densities close to quarter critical.[28] The OMEGA spectrum implies the absence of SRS around $n_c/4$ and the presence of TPD, while the NIF spectrum implies the presence of SRS at and below $n_c/4$. Although the presence of some TPD activity in the NIF experiment cannot be entirely ruled out on the basis of Fig. 151.22(a) since the conversion efficiencies of TPD waves to half-harmonic emission relative to absolute SRS are difficult to quantify, it seems most plausible that SRS, rather than TPD, is the dominant quarter-critical LPI mechanism in ignition-scale direct-drive experiments.

Simple considerations based on the absolute threshold intensities for SRS $\left(I_{14}^{\mathrm{SRS,thr}} = 2377/L_{\mathrm{n},\mu\mathrm{m}}^{4/3}\right)$ and TPD $\left(I_{14}^{\mathrm{TPD,thr}} = 233\,T_{\mathrm{e,keV}}/L_{\mathrm{n},\mu\mathrm{m}}\right)$, for normally incident single plane-wave beams,[9,10] further support this identification. In these expressions, I_{14}^{thr} is the threshold intensity in units of 10^{14} W/cm^2. As an illustrative case, Fig. 151.23 shows the ratio of the absolute TPD threshold to twice that for absolute SRS as a function of electron temperature and density scale length. This

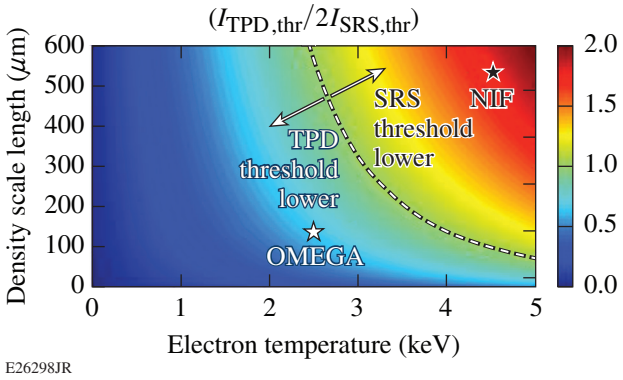

Figure 151.23
Ratio of absolute single-beam intensity threshold for two-plasmon decay (TPD)[10] to twice the absolute, single-beam threshold for SRS[9] (to acknowledge a potential difference in multibeam effects) as a function of electron temperature and density scale length. Conditions corresponding to the NIF (OMEGA) spectra in Fig. 151.22(a) are represented by the black (white) star. To the left (right) of the dashed line, the TPD (SRS) threshold is lower and TPD (SRS) is expected to be dominant.

is intended to acknowledge the fact that while TPD has been observed to be a multibeam phenomenon, it may be the case that fewer beams contribute to SRS. The OMEGA experiment that produced the spectrum shown adjacent to Fig. 151.22(a) ($L_n \sim 150$ μm, $T_e \sim 2.5$ keV, $I \sim 6 \times 10^{14}$ W/cm^2) is marginally unstable with respect to TPD and slightly less so to SRS if the total overlapped laser intensities are substituted into the expressions for the single-beam thresholds. In contrast, the NIF experiment at ignition-relevant conditions ($L_n \sim 525$ μm, $T_e \sim 4.5$ keV, $I \sim 1.3 \times 10^{15}$ W/cm^2), which produced the spectrum shown in Fig. 151.22(a), is in the SRS-dominated regime: the threshold for SRS is exceeded by a factor of ~22, while the TPD threshold is exceeded by a factor of ~6. It is expected that this qualitative trend of SRS being increasingly prominent relative to TPD with increasing scale length and temperature[32] applies also for more-complicated cases of multiple obliquely incident beams, although this is a subject of future work.

The broad spectral features seen in Figs. 151.22(a)–151.22(c) are characteristic of SRS occurring at densities below $n_c/4$ (between 0.15 and 0.22 n_c). Figures 151.22(b) and 151.22(c) highlight SRS spectra obtained at two different angles of observation and two distinct irradiation conditions. The target normal was parallel to the NIF polar axis [Fig. 151.22(f)], and the target was irradiated symmetrically, first by the outer beams from $t = 0$ to $t = 4.5$ ns, followed by the inner beams from $t = 4.5$ ns to $t = 7.5$ ns [Fig. 151.22(g)]. The predicted quarter-critical plasma conditions during the outer (inner) beam drive were $L_n \sim 500$ (690) μm, $I \sim 1.6$ (1.1) $\times 10^{15}$ W/cm^2, and $T_e \sim 4.7$ (4.4) keV, respectively. Temporally resolved scattered-light spectra[26] were obtained at 23.5° [Fig. 151.22(b)] and 50° [Fig. 151.22(c)]. SRS is observed by both diagnostics at early times during outer-beam irradiation and at later times when irradiated by the inner beams.

This observation is attributed to SRS sidescatter,[33] for which newly developed theory and supporting simulations are described in a companion manuscript.[34] In this process the SRS light waves propagate approximately tangentially to contours of constant electron density in the corona and see much greater gains relative to backscatter. The data shown in Figs. 151.22(b) and 151.22(c) are in agreement with the predictions of this theory and cannot be explained by narrow-angle backscatter simply caused by refraction, particularly for the SRS observed at 50°. Therefore, the propagation direction (and collection angle) of SRS light, after it has finished refracting and is in vacuum, is determined solely by its wavelength (i.e., the density where it was generated) and depends only weakly on the incidence angle of the beams that produced it. This is evident in Fig. 151.22(b), where SRS light at 23.5° is observed

at ~650 nm during both outer-beam and inner-beam irradiation. The SRS shifts to shorter wavelengths (~620 nm) when the observation angle is moved to 50°.

To determine the total amount of SRS generated in these experiments, absolutely calibrated photodiodes measured the SRS light collected in $\sim 2 \times 10^{-3}$ sr in the two full-aperture backscatter stations (FABS's)[26] at 50° and 30°. These measurements were then extrapolated to account for the total emission. This was accomplished using a ray-tracing code with plasma parameters and geometry provided by *DRACO* simulations to obtain simulated SRS emission profiles that include refraction and absorption as functions of wavelength and angle of observation (transmission of SRS light from its origin ranges from 2% at 702 nm to ~50% at 630 nm). These calculations assume 2π azimuthal symmetry around the target normal. With the above assumptions, it is estimated that between 2% and 6% of incident laser energy is converted to SRS light.

The inferred SRS light energy is compared to the energy in hot electrons, which is inferred from hard x-ray bremsstrahlung emission generated by the interaction of hot electrons with the target.[35] This bremsstrahlung emission was detected using the NIF filter fluorescer (FFLEX) diagnostic.[36] The FFLEX signals were analyzed by performing Monte Carlo electron–photon transport calculations with the *EGSnrc* code,[37] using a single-temperature (T_{hot}) 3-D Maxwellian hot-electron distribution. These calculations relate the absolute intensity of hard x-ray emission to the total quantity of hot electrons that produce it. Figure 151.24 shows the corresponding fraction of laser energy converted to hot electrons (f_{hot}) as a function of laser intensity at the quarter-critical density as calculated by *DRACO* for a series of experiments that include both CH and Si targets. The hard x-ray data were integrated over the period of the experiment starting after 4.5 ns. For outer-beam irradiation, f_{hot} increased from 0.7±0.2% to 2.9±0.6% as the laser intensity increased from 5.9×10^{14} W/cm^2 to 14×10^{14} W/cm^2. For inner-beam irradiation of CH targets, f_{hot} increased from 1.2±0.2% to 2.6±0.5% for intensities of 6.2×10^{14} W/cm^2 to 11×10^{14} W/cm^2. The uncertainty in f_{hot} is based on the statistical uncertainty in the single-temperature fit to the hard x-ray spectra. For CH experiments, T_{hot} is inferred to be between 45 and 55 keV for the outer-beam drive and 62 keV for the inner-beam drive, independent of laser intensity, with an uncertainty of ±4 to 5 keV. The threshold intensity for the onset of measurable hot electrons in CH targets lies in the vicinity of 4×10^{14} W/cm^2.

The inferred energy and temperature of the hot electrons are consistent with simple arguments based on SRS being

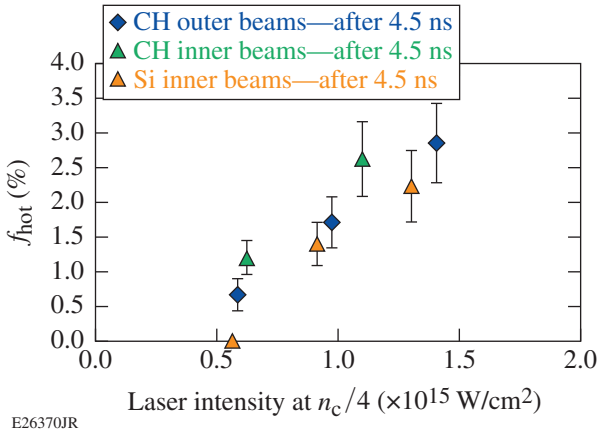

Figure 151.24
Fraction of laser energy converted to hot electrons as a function of quarter-critical laser intensity, for laser drive using outer beams (diamonds) and inner beams (triangles), for CH ablators (blue, green) and Si ablators (orange). The uncertainty in f_{hot} is based on the statistical uncertainty in T_{hot} extracted from the fit to the hard x-ray spectrum, propagated through *EGSnrc* modeling.

their source. By conserving wave action in the scattering process (i.e., the Manley–Rowe relations[38]), it was determined that, for SRS wavelengths between 600 and 650 nm, the total energy in plasma waves is 70% to 85% of the total energy in SRS or between 1.4% and 5% of the incident laser energy for the experiments shown in Fig. 151.22. It is quite plausible that kinetic mechanisms such as wave breaking or stochastic processes can convert the plasma-wave energy into hot electrons with an efficiency sufficient to account for the fraction that is observed (f_{hot} = 1% to 3%). The characteristic temperature for SRS-generated electrons is often estimated by $T_\phi = (1/2)\, m_e v_\phi^2$ (Ref. 8), where v_ϕ is the phase velocity of the plasma wave. For our experiments, where SRS is observed from wavelengths of ~620 nm to ~702 nm ($2\lambda_0$), the corresponding hot-electron temperatures range from ~30 to ~85 keV ($T_\phi \sim m_e c^2/6$ for $n_e = n_c/4$), which is consistent with the hot-electron temperatures that best fit the measured hard x-ray spectrum.

The combination of T_{hot} and f_{hot} inferred in these experiments is close to the level that can be permitted in direct-drive–ignition designs, typically considered to be f_{hot} ~0.5% to 1% for T_{hot} ~ 50 keV (Refs. 2 and 39). This estimate is based on an allowable coupling of ~0.1% of laser energy to hot-electron preheat in the DT fuel and a near-2π angular divergence of hot electrons inferred in OMEGA spherical experiments.[20] Based on these data, direct-drive–ignition designs using a CH ablator and quarter-critical laser intensities of $\sim 5 \times 10^{14}$ W/cm^2 may be acceptable, but for higher intensities, LPI mitigation is likely to be necessary. The discovery of a regime dominated by SRS, rather than by TPD as on OMEGA, necessitates a

re-evaluation of the angular divergence of hot electrons at direct-drive ignition-relevant conditions and may also require reconsideration of mitigation strategies.

One potential LPI mitigation strategy, originally proposed for TPD, uses strategically placed mid-Z layers in the ablator to locally shorten the density scale length, increase the electron temperature, enhance electron–ion collisional damping, and reduce Landau damping of ion-acoustic waves.[40–45] This reduction in scale length and increase in temperature are predicted as well for planar Si experiments (L_n from ~690 μm in CH to ~560 μm in Si; T_e from ~4.4 keV in CH to ~5.2 keV in Si), for which hot-electron data are shown in Fig. 151.24. The use of Si ablators has a modest effect on hot-electron levels, although it does increase the hot-electron intensity threshold to around 6×10^{14} W/cm^2. The lack of hot electrons in this experiment also correlates with a minimal level of SRS observed in any of the spectrometers.

In summary, the first experiments to investigate LPI at direct-drive ignition-relevant coronal plasma conditions have revealed evidence of a regime dominated by SRS, with a significant contribution from tangential sidescatter. This result is in stark contrast to prior experiments on OMEGA at shorter scale lengths and lower temperatures, in which SRS was minimal and quarter-critical instabilities were identified as TPD. For the first time, intensity thresholds for LPI hot electrons have been evaluated at direct-drive–ignition scales, and the use of a Si ablator has been found to increase the threshold intensity slightly, from ~4×10^{14} W/cm^2 to ~6×10^{14} W/cm^2. These quarter-critical laser intensities present a viable design space for direct drive. As discussed, these results have implications for LPI hot-electron preheat mitigation in direct-drive–ignition designs, which traditionally have included strategies to mitigate TPD, but will have to consider SRS. In future experiments, it will be important to characterize the angular distribution of hot electrons, which strongly affects the tolerable level of hot-electron generation and may be different in this SRS-dominated regime than in TPD-dominated experiments on OMEGA.[20] Optical Thomson scattering will ultimately be used on the NIF[46,47] to directly probe and characterize plasma waves in the quarter-critical region, as has been done previously on OMEGA,[16] in order to definitively assess the presence or absence of TPD.

ACKNOWLEDGMENT

The authors thank NIF Operations and Target Fabrication Groups for their assistance in executing these experiments. This material is based upon work supported by the Department of Energy National Nuclear Security Administration under Award No. DE-NA0001944, the University of Rochester, and the New York State Energy Research and Development Authority. The support of the DOE does not constitute an endorsement by the DOE of the views expressed in this article.

REFERENCES

1. J. Nuckolls *et al*., Nature **239**, 139 (1972).
2. R. S. Craxton, K. S. Anderson, T. R. Boehly, V. N. Goncharov, D. R. Harding, J. P. Knauer, R. L. McCrory, P. W. McKenty, D. D. Meyerhofer, J. F. Myatt, A. J. Schmitt, J. D. Sethian, R. W. Short, S. Skupsky, W. Theobald, W. L. Kruer, K. Tanaka, R. Betti, T. J. B. Collins, J. A. Delettrez, S. X. Hu, J. A. Marozas, A. V. Maximov, D. T. Michel, P. B. Radha, S. P. Regan, T. C. Sangster, W. Seka, A. A. Solodov, J. M. Soures, C. Stoeckl, and J. D. Zuegel, Phys. Plasmas **22**, 110501 (2015).
3. G. H. Miller, E. I. Moses, and C. R. Wuest, Opt. Eng. **43**, 2841 (2004).
4. S. Atzeni and J. Meyer-ter-Vehn, *The Physics of Inertial Fusion: Beam Plasma Interaction, Hydrodynamics*, Hot Dense Matter, International Series of Monographs on Physics (Clarendon Press, Oxford, 2004).
5. D. W. Phillion *et al*., Phys. Fluids **25**, 1434 (1982).
6. H. Figueroa *et al*., Phys. Fluids **27**, 1887 (1984).
7. W. Seka, E. A. Williams, R. S. Craxton, L. M. Goldman, R. W. Short, and K. Tanaka, Phys. Fluids **27**, 2181 (1984).
8. W. L. Kruer, in *The Physics of Laser Plasma Interactions*, Frontiers in Physics, Vol. 73, edited by D. Pines (Addison-Wesley, Redwood City, CA, 1988), Chap. 4, pp. 37–43.
9. A. Simon, R. W. Short, E. A. Williams, and T. Dewandre, Phys. Fluids **26**, 3107 (1983).
10. C. S. Liu, M. N. Rosenbluth, and R. B. White, Phys. Fluids **17**, 1211 (1974).
11. N. A. Ebrahim *et al*., Phys. Rev. Lett. **45**, 1179 (1980).
12. R. P. Drake, R. E. Turner, B. F. Lasinski, K. G. Estabrook, E. M. Campbell, C. L. Wang, D. W. Phillion, E. A. Williams, and W. L. Kruer, Phys. Rev. Lett. **53**, 1739 (1984).
13. C. Stoeckl, R. E. Bahr, B. Yaakobi, W. Seka, S. P. Regan, R. S. Craxton, J. A. Delettrez, R. W. Short, J. Myatt, A. V. Maximov, and H. Baldis, Phys. Rev. Lett. **90**, 235002 (2003).
14. D. T. Michel, A. V. Maximov, R. W. Short, S. X. Hu, J. F. Myatt, W. Seka, A. A. Solodov, B. Yaakobi, and D. H. Froula, Phys. Rev. Lett. **109**, 155007 (2012).
15. J. F. Myatt, J. Zhang, R. W. Short, A. V. Maximov, W. Seka, D. H. Froula, D. H. Edgell, D. T. Michel, I. V. Igumenshchev, D. E. Hinkel, P. Michel, and J. D. Moody, Phys. Plasmas **21**, 055501 (2014).
16. R. K. Follett, D. H. Edgell, R. J. Henchen, S. X. Hu, J. Katz, D. T. Michel, J. F. Myatt, J. Shaw, and D. H. Froula, Phys. Rev. E **91**, 031104(R) (2015).
17. P. Michel *et al*., Phys. Rev. Lett. **115**, 055003 (2015).

18. S. Depierreux, C. Neuville, C. Baccou, V. Tassin, M. Casanova, P.-E. Masson-Laborde, N. Borisenko, A. Orekhov, A. Colaitis, A. Debayle, G. Duchateau, A. Heron, S. Huller, P. Loiseau, P. Nicolaï, D. Pesme, C. Riconda, G. Tran, R. Bahr, J. Katz, C. Stoeckl, W. Seka, V. Tikhonchuk, and C. Labaune, Phys. Rev. Lett. **117**, 235002 (2016).

19. W. Seka, J. F. Myatt, R. W. Short, D. H. Froula, J. Katz, V. N. Goncharov, and I. V. Igumenshchev, Phys. Rev. Lett. **112**, 145001 (2014).

20. B. Yaakobi, A. A. Solodov, J. F. Myatt, J. A. Delettrez, C. Stoeckl, and D. H. Froula, Phys. Plasmas **20**, 092706 (2013).

21. J. D. Lindl, Phys. Plasmas **2**, 3933 (1995).

22. T. R. Boehly, D. L. Brown, R. S. Craxton, R. L. Keck, J. P. Knauer, J. H. Kelly, T. J. Kessler, S. A. Kumpan, S. J. Loucks, S. A. Letzring, F. J. Marshall, R. L. McCrory, S. F. B. Morse, W. Seka, J. M. Soures, and C. P. Verdon, Opt. Commun. **133**, 495 (1997).

23. T. J. B. Collins, J. A. Marozas, K. S. Anderson, R. Betti, R. S. Craxton, J. A. Delettrez, V. N. Goncharov, D. R. Harding, F. J. Marshall, R. L. McCrory, D. D. Meyerhofer, P. W. McKenty, P. B. Radha, A. Shvydky, S. Skupsky, and J. D. Zuegel, Phys. Plasmas **19**, 056308 (2012).

24. S. Skupsky, R. W. Short, T. Kessler, R. S. Craxton, S. Letzring, and J. M. Soures, J. Appl. Phys. **66**, 3456 (1989).

25. I. V. Igumenshchev, D. H. Edgell, V. N. Goncharov, J. A. Delettrez, A. V. Maximov, J. F. Myatt, W. Seka, A. Shvydky, S. Skupsky, and C. Stoeckl, Phys. Plasmas **17**, 122708 (2010).

26. J. D. Moody *et al*., Rev. Sci. Instrum. **81**, 10D921 (2010).

27. P. B. Radha, V. N. Goncharov, T. J. B. Collins, J. A. Delettrez, Y. Elbaz, V. Yu. Glebov, R. L. Keck, D. E. Keller, J. P. Knauer, J. A. Marozas, F. J. Marshall, P. W. McKenty, D. D. Meyerhofer, S. P. Regan, T. C. Sangster, D. Shvarts, S. Skupsky, Y. Srebro, R. P. J. Town, and C. Stoeckl, Phys. Plasmas **12**, 032702 (2005).

28. W. Seka, B. B. Afeyan, R. Boni, L. M. Goldman, R. W. Short, K. Tanaka, and T. W. Johnston, Phys. Fluids **28**, 2570 (1985).

29. T. Dewandre, J. R. Albritton, and E. A. Williams, Phys. Fluids **24**, 528 (1981).

30. The Doppler shift resulting from plasma flow affects the wavelength of both the incoming 351-nm light and the outgoing $\omega/2$ light, and constitutes an ~10% effect on the $\omega/2$ wavelength. The Dewandre shift results from plasma expansion and an increase in the plasma density between the quarter-critical region and the observer as $\omega/2$ propagates outward, and is an ~2% effect on the wavelength.

31. W. Seka, D. H. Edgell, J. F. Myatt, A. V. Maximov, R. W. Short, V. N. Goncharov, and H. A. Baldis, Phys. Plasmas **16**, 052701 (2009).

32. S. Weber and C. Riconda, High Power Laser Sci. Eng. **3**, e6 (2015).

33. B. B. Afeyan and E. A. Williams, Phys. Fluids **28**, 3397 (1985).

34. P. Michel, M. J. Rosenberg, T. Chapman, W. Seka, A. Solodov, R. W. Short, C. Goyon, M. Hohenberger, J. D. Moody, S. P. Regan, and J. F. Myatt, "Measurements and Modeling of Raman Side-Scatter in ICF Experiments," submitted to Physical Review Letters.

35. R. P. Drake, R. E. Turner, B. F. Lasinski, E. A. Williams, K. Estabrook, W. L. Kruer, E. M. Campbell, and T. W. Johnston, Phys. Rev. A **40**, 3219 (1989).

36. M. Hohenberger, F. Albert, N. E. Palmer, J. J. Lee, T. Döppner, L. Divol, E. L. Dewald, B. Bachmann, A. G. MacPhee, G. LaCaille, D. K. Bradley, and C. Stoeckl, Rev. Sci. Instrum. **85**, 11D501 (2014).

37. I. Kawrakow, Med. Phys. **27**, 485 (2000).

38. J. M. Manley and H. E. Rowe, Proc. IRE **44**, 904 (1956).

39. M. Hohenberger, P. B. Radha, J. F. Myatt, S. LePape, J. A. Marozas, F. J. Marshall, D. T. Michel, S. P. Regan, W. Seka, A. Shvydky, T. C. Sangster, J. W. Bates, R. Betti, T. R. Boehly, M. J. Bonino, D. T. Casey, T. J. B. Collins, R. S. Craxton, J. A. Delettrez, D. H. Edgell, R. Epstein, G. Fiksel, P. Fitzsimmons, J. A. Frenje, D. H. Froula, V. N. Goncharov, D. R. Harding, D. H. Kalantar, M. Karasik, T. J. Kessler, J. D. Kilkenny, J. P. Knauer, C. Kurz, M. Lafon, K. N. LaFortune, B. J. MacGowan, A. J. Mackinnon, A. G. MacPhee, R. L. McCrory, P. W. McKenty, J. F. Meeker, D. D. Meyerhofer, S. R. Nagel, A. Nikroo, S. Obenschain, R. D. Petrasso, J. E. Ralph, H. G. Rinderknecht, M. J. Rosenberg, A. J. Schmitt, R. J. Wallace, J. Weaver, C. Widmayer, S. Skupsky, A. A. Solodov, C. Stoeckl, B. Yaakobi, and J. D. Zuegel, Phys. Plasmas **22**, 056308 (2015).

40. R. E. Turner, K. Estabrook, R. L. Kauffman, D. R. Bach, R. P. Drake, D. W. Phillion, B. F. Lasinski, E. M. Campbell, W. L. Kruer, and E. A. Williams, Phys. Rev. Lett. **54**, 189 (1985); **54**, 1878(E) (1985).

41. V. A. Smalyuk, R. Betti, J. A. Delettrez, V. Yu. Glebov, D. D. Meyerhofer, P. B. Radha, S. P. Regan, T. C. Sangster, J. Sanz, W. Seka, C. Stoeckl, B. Yaakobi, J. A. Frenje, C. K. Li, R. D. Petrasso, and F. H. Séguin, Phys. Rev. Lett. **104**, 165002 (2010).

42. J. F. Myatt, H. X. Vu, D. F. DuBois, D. A. Russell, J. Zhang, R. W. Short, and A. V. Maximov, Phys. Plasmas **20**, 052705 (2013).

43. S. X. Hu, D. T. Michel, D. H. Edgell, D. H. Froula, R. K. Follett, V. N. Goncharov, J. F. Myatt, S. Skupsky, and B. Yaakobi, Phys. Plasmas **20**, 032704 (2013).

44. R. K. Follett, J. A. Delettrez, D. H. Edgell, V. N. Goncharov, R. J. Henchen, J. Katz, D. T. Michel, J. F. Myatt, J. Shaw, A. A. Solodov, C. Stoeckl, B. Yaakobi, and D. H. Froula, Phys. Rev. Lett. **116**, 155002 (2016).

45. J. R. Fein, J. P. Holloway, M. R. Trantham, P. A. Keiter, D. H. Edgell, D. H. Froula, D. Haberberger, Y. Frank, M. Fraenkel, E. Raicher, D. Shvarts, and R. P. Drake, Phys. Plasmas **24**, 032707 (2017).

46. P. Datte, J. S. Ross, D. Froula, J. Galbraith, S. Glenzer, B. Hatch, J. Kilkenny, O. Landen, A. M. Manuel, W. Molander, D. Montgomery, J. Moody, G. Swadling, J. Weaver, G. Vergel de Dios, and M. Vitalich, J. Phys.: Conf. Ser. **717**, 012089 (2016).

47. J. S. Ross, P. Datte, L. Divol, J. Galbraith, D. H. Froula, S. H. Glenzer, B. Hatch, J. Katz, J. Kilkenny, O. Landen, A. M. Manuel, W. Molander, D. S. Montgomery, J. D. Moody, G. Swadling, and J. Weaver, Rev. Sci. Instrum. **87**, 11E510 (2016).

Measurement of Cryogenic Target Position and Implosion Core Offsets on OMEGA

Introduction

Direct-drive inertial confinement fusion experiments are performed by uniformly illuminating spherical cryogenic deuterium–tritium (DT) fuel-bearing CH shell capsules with high-power laser beams.[1] A goal of inertial confinement fusion (ICF) experiments is thermonuclear ignition and gain; in order for this to occur, the fuel must be symmetrically compressed to high areal densities, i.e., at least 0.3 g/cm^2, and the central hot-spot temperature must be at least 10 keV (Refs. 2–4). Target performance is degraded by imperfections in symmetric laser illumination and in the target itself. Perturbations of the intensity in the low Legendre modes ($\ell \leq 6$), which may include target offset, can distort the core at stagnation while higher-mode ($\ell \geq 6$) perturbations lead to Rayleigh–Taylor unstable growth, target breakup, and mixing of the materials in the shell and fuel.[5] These perturbations reduce the peak temperature and areal density of the final fuel region; therefore, minimizing them is desired. Assessing the performance of the implosions requires one to simulate the implosion with one-dimensional (Ref. 6) and multidimensional hydrocode simulations,[7] and the multidimensional simulations require accurate values of target offset from beam aiming to accurately simulate the implosions. This article describes our method of measuring initial target offset from the aim point of the beams and determining the core offset resulting from target offset from this aim point.

Measurements of Initial Target Offsets

Targets illuminated by the 60 beams of OMEGA at intensities ranging from ~10^{14} to ~10^{15} W/cm^2 emit x rays, easily imaged by pinhole cameras, in the range of 1 to 10 keV. A set of x-ray pinhole cameras (XRPC's) is used on OMEGA to precisely align the laser beams to the target center.[8] This is currently done to an accuracy of ~7-μm rms (root mean square) using a set of fixed and retractable XRPC's, all digitally recording the images with charge-injection–device (CID) cameras.[9] This set includes five fixed XRPC's, which are attached to the OMEGA target chamber, and six ten-inch-manipulator (TIM)–based XRPC's, which are retractable through a vacuum gate valve. The fixed XRPC's remain in use during both cryogenic target and non-cryogenic target implosions.

Since the targets used to precisely align the OMEGA beams by locating the x-ray spot emitted by each beam on pointing shots[8] are positioned by visible light cameras, all other non-cryogenic targets are aligned to this same point. This position is referred to as target chamber center (TCC), although it is really the aim point of the beams determined through precision pointing using the CID-based XRPC's. The precise locations of TCC in the XRPC images are determined by measuring x rays emitted by a precisely located non-cryogenic target; these TCC reference images are all from target shots taken on the same day as the cryogenic target shots. This effectively eliminates the possibility of changes in the XRPC's contributing to the determined offsets. Positioning cryogenic targets is complicated by the need to view the cryogenic target through windows in the shroud that maintains the target at near the triple point (~20 K). These windows refract the light passing through them by an amount that must be determined by testing prior to the actual shots. Furthermore, vibration of the cryogenic target stalk while the shroud is in place and impulses transmitted to this stalk when the shroud is retracted (~50 ms before the shot) can misplace the cryogenic target. This can cause the cryogenic target to be offset from TCC at t_0 (the beginning of the laser pulse).

The example of a non-cryogenic target XRPC image in Fig. 151.25(a) shows a 1.5×1.5-mm region at the target plane. The outer edge of the x-ray emission, which occurs at t_0, is determined from the maximum gradient using a Sobel filter.[10] This set of positions is then fit to a circle whose center position is then determined [overlaid circle and central cross in Fig. 151.25(a)]. An example cryogenic target x-ray image is shown in Fig. 151.25(b). The fusion neutrons created by the implosion of this target ($y_n = 3 \times 10^{13}$) have generated copious amounts of noise including a gamma-ray–induced background, single-pixel upsets caused by neutron-scattering events that produce protons, and line and column noise caused by similar interactions with the readout structure of the CID camera. This noise can in large part be removed by first filtering the image using a single-pixel upset detection and replacement algorithm,[11] next by removing the average line and column noise measured away from the image itself, and lastly by using a

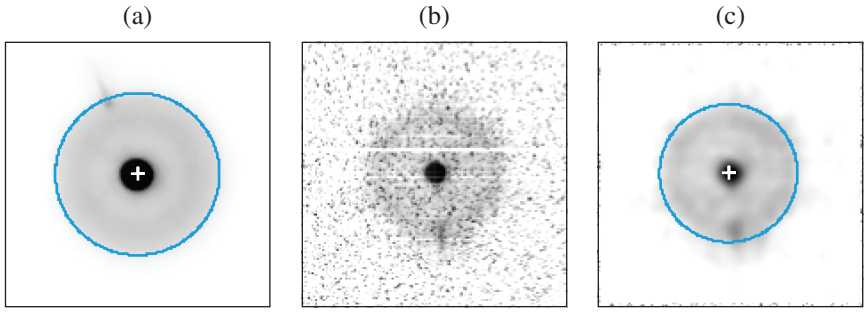

Figure 151.25
X-ray images from the OMEGA H4 x-ray pinhole camera (XRPC) charge-injection device (CID). (a) Target chamber center (TCC) reference image on shot 85780, (b) unfiltered image from a cryogenic target on shot 85784, and (c) filter image of the same. Both the reference image (a) and the filtered cryogenic target shot image (c) have the best-fit positions indicated by a circle and a cross in the center.

median filter to reduce additional noise. The result of performing this noise removal procedure is shown in Fig. 151.25(c), and the position of the center of the cryogenic target is determined in like fashion to the reference non-cryogenic target. The pixel-location differences of the two centers are then converted to microns, and the difference between the cryogenic target position and the reference target position is a measured projected offset at t_0.

Two methods are employed to determine the three-space offset **r** of cryogenic targets at t_0 from TCC. Both methods use the projected offsets of the cryogenic target centers at t_0 from the reference non-cryogenic targets whose centers are at TCC. The view vectors for each XRPC are related to the target chamber vector coordinates by the following formulas:

$$\mathbf{q} = \frac{\mathbf{z}\times\mathbf{v}}{\left|\mathbf{z}\times\mathbf{v}\right|}, \tag{1}$$

$$\mathbf{p} = \frac{\mathbf{v}\times\mathbf{q}}{\left|\mathbf{v}\times\mathbf{q}\right|}, \tag{2}$$

where **q** is the horizontal vector in an image whose view direction is **v** and the normalized cross product of **z** (straight up) and **v**, while the vertical direction in the image plane **p** is given by the normalized cross product of **v** and **q** (see Fig. 151.26).

The XRPC's provide multiple quasi-orthogonal views of the target x-ray emission, from which **r** can be determined. The first method uses the projected offsets from pairs of cameras to determine the three-space offsets. For an offset in space of **r**, the projections of **r** in a pair of camera views are given by

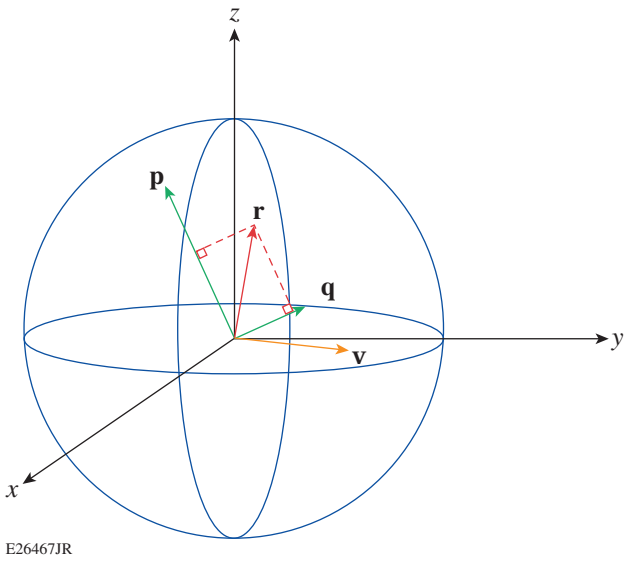

Figure 151.26
Vector representation displaying view direction, solution direction, and unit vectors of image plane with respect to each other.

$$\mathbf{r}\cdot\mathbf{q}_1 = r_x q_{x_1} + r_y q_{y_1} + r_z q_{z_1}, \tag{3}$$

$$\mathbf{r}\cdot\mathbf{p}_1 = r_x p_{x_1} + r_y p_{y_1} + r_z p_{z_1}, \tag{4}$$

$$\mathbf{r}\cdot\mathbf{q}_2 = r_x q_{x_2} + r_y q_{y_2} + r_z q_{z_2}, \tag{5}$$

$$\mathbf{r}\cdot\mathbf{p}_2 = r_x p_{x_2} + r_y p_{y_2} + r_z p_{z_2}, \tag{6}$$

where 1 and 2 refer to the first and second view, respectively. The results can be combined into two different matrices by choosing to solve for **r** using either Eqs. (3), (4), and (5) or Eqs. (3), (4), and (6). This is equivalent to using the vertical offset from either camera 1 or 2. These choices can be written in matrix form as follows:

$$\overleftrightarrow{M}_{q_1q_2p_1} \cdot \mathbf{r} = \begin{bmatrix} r_{q_1} \\ r_{q_2} \\ r_{p_1} \end{bmatrix} = \begin{bmatrix} q_{x_1} & q_{y_1} & q_{z_1} \\ q_{x_2} & q_{y_2} & q_{z_2} \\ p_{x_1} & p_{y_1} & p_{z_1} \end{bmatrix} \begin{bmatrix} r_x \\ r_y \\ r_z \end{bmatrix}, \tag{7}$$

$$\overleftrightarrow{M}_{q_1q_2p_2} \cdot \mathbf{r} = \begin{bmatrix} r_{q_1} \\ r_{q_2} \\ r_{p_2} \end{bmatrix} = \begin{bmatrix} q_{x_1} & q_{y_1} & q_{z_1} \\ q_{x_2} & q_{y_2} & q_{z_2} \\ p_{x_2} & p_{y_2} & p_{z_2} \end{bmatrix} \begin{bmatrix} r_x \\ r_y \\ r_z \end{bmatrix}. \tag{8}$$

Inverting the matrices gives two possible solutions to the offset as follows:

$$\mathbf{r}_{121} = \overleftrightarrow{M}^{-1}_{q_1q_2p_1} \cdot \mathbf{r}_{q_1q_2p_1}, \tag{9}$$

$$\mathbf{r}_{122} = \overleftrightarrow{M}^{-1}_{q_1q_2p_2} \cdot \mathbf{r}_{q_1q_2p_2}. \tag{10}$$

The average of these two solutions is the choice used in this method and is given by

$$\mathbf{r} = \frac{\left(\mathbf{r}_{121} + \mathbf{r}_{122}\right)}{2}. \tag{11}$$

To improve the accuracy of determining **r**, values are computed from as many quasi-orthogonal camera pairs as possible. The results are averaged and the standard deviations of the values are used as an estimate of the errors of these values.

The second method of determining **r** uses a least-squares approach. For a given assumed offset of the target **r**, the values r_{q_i} and r_{p_i} that would be observed in the ith view are given by

$$r_{q_i} = r_x q_x + r_y q_y + r_z q_z, \tag{12}$$

$$r_{p_i} = r_x p_x + r_y p_y + r_z p_z. \tag{13}$$

The least-squares search is performed to minimize the quantity χ^2 given by

$$\chi^2 = \sum_i \left(\Delta r_{\perp,i}\right)^2 w_i^2, \tag{14}$$

where the values w_i are the weights given to the ith view and the quantities $\Delta r_{\perp,i}$ are the perpendicular offsets in the ith view in turn given by

$$\Delta r_{\perp,i} = \sqrt{\left(r_{q_i} - \Delta q_i\right)^2 + \left(r_{p_i} - \Delta p_i\right)^2}, \tag{15}$$

where Δq_i and Δp_i are the horizontal and vertical offsets of the target in the ith view. The value of **r** that minimizes χ^2 is taken as the best value, while the error dr is given by

$$\mathrm{d}r = \left(\chi^2 \Big/ \sum w_i\right)^{1/2} \tag{16}$$

and is equivalent to the error of the mean of the best-fit value. When only two views are available, the first method of determining **r** is the best method to use, whereas when more than two views are available, the second method gives the most unbiased result. Table 151.I shows the current set of fixed XRPC's used in this position analysis. Typical errors when determining the position are ~3 to 5 μm.

Table 151.I: X-ray pinhole camera (XRPC) parameters.

Camera	Position θ (°)	Position ϕ (°)	Magnification
h4	29.52* 45.23**	234.00	4.047* 3.861**
h8	79.30	153.78	2.028
h12	108.89	54.00	4.000
h13	9.74	342.00	4.043
p2	68.43	54.00	3.992

*Before 17 March 2017
**After 17 March 2017

Measurement of Implosion Core Offsets

The implosion cores are imaged by the gated monochromatic x-ray imager (GMXI)[12] operating in time-integrating mode with four CID cameras recording the four images formed by the Kirkpatrick–Baez (KB) microscope optical assembly. Two of these images (GMXI-c and GMXI-d, filtered by 50.8 and 76.2 μm of Al, respectively) had signal levels that did not exceed the capacity of the CID cameras for all cryogenic and non-cryogenic target experiments that determined reference core positions. As for determining the t_0 offset, the non-cryogenic reference target is assumed to be perfectly centered at TCC. The energy bands are approximately the same for these two images being ~5 to 8 keV and ~5.5 to 8 keV for images GMXI-c and GMXI-d, respectively. The GMXI cameras observe the implosion cores from the common spherical coordinates θ = 96.02°, ϕ = 54° with respect to the target plane (each being ~1° away).

In contrast to the t_0 images where the limb of the image is used to determine the center, core images are centrally peaked, so the centroid is a better measure of the core's position in the CID image. Figure 151.27 shows example GMXI images, trimmed to 200 × 200 μm. The reference images used in this

case are from a target experiment with a non-cryogenic target consisting of an 18-μm-thick CH shell filled with 3 atm of D_2 gas, imploded with the same pulse shape used on the subsequent cryogenic target shots [these are referred to as pulse-shape setup (PSS) shots]. Figures 151.27(a) and 151.27(b) are from the reference non-cryogenic target implosion (OMEGA shot 81056, GMXI-c and GMXI-d images); Figs. 151.27(c) and 151.27(d) are from a cryogenic target implosion (OMEGA shot 81060, GMXI-c and GMXI-d images). The "×" symbols denote the centroids of the images; the diamond symbols on the GMXI-c and GMXI-d images of OMEGA shot 81060 show the points of maximum cross correlation between the cryogenic and PSS shots in the GMXI-c and GMXI-d images, respectively. The square symbols on shot 81060 images denote the averages between the centroid centers and the cross-correlation maximums. The amount of core offset is taken as the amount by which the image must be shifted to maximize the cross correlation. Figure151.28 shows the core offsets determined from the GMXI-c and GMXI-d images for a large number of cryogenic target shots; their consistency is evident. The average offset of the GMXI-c and GMXI-d images is therefore taken as the offset and the difference is an estimate of the error of this offset.

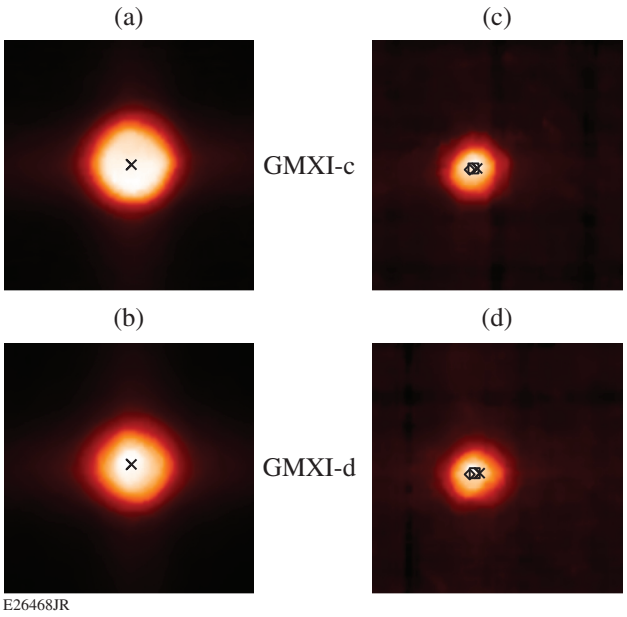

Figure 151.27

Four 200 × 200-μm gated monochromatic x-ray imager (GMXI) images, including a reference and a cryogenic shot. The "×" represents the centroid centers, diamonds represent the cross-correlation maximums, and squares represent the averages between those points. The offset of OMEGA shot 81060 from OMEGA shot 81056 is (–22.0,–5.0)±(0.0,2.0).

The t_0 offsets are compared with the GMXI offsets by computing the projections of the t_0 offsets in the view of the GMXI in the horizontal and vertical directions $q_{0,\mathrm{GMXI}}$ and $p_{0,\mathrm{GMXI}}$, respectively, given by

$$q_{0,\mathrm{GMXI}} = \mathbf{r} \cdot \mathbf{q}_{\mathrm{GMXI}}, \tag{17}$$

$$p_{0,\mathrm{GMXI}} = \mathbf{r} \cdot \mathbf{p}_{\mathrm{GMXI}}, \tag{18}$$

where $\mathbf{q}_{\mathrm{GMXI}}$ and $\mathbf{p}_{\mathrm{GMXI}}$ are the horizontal and vertical vectors, respectively, of the GMXI view. Since there is no other digitally recorded view of the core, the three-space core offset cannot be determined but the GMXI core offset and the projection of the t_0 offset into the GMXI view can be compared.

Results

Figures 151.29 and 151.30 show the measured core offsets compared to the projected t_0 offsets for horizontal, vertical, and

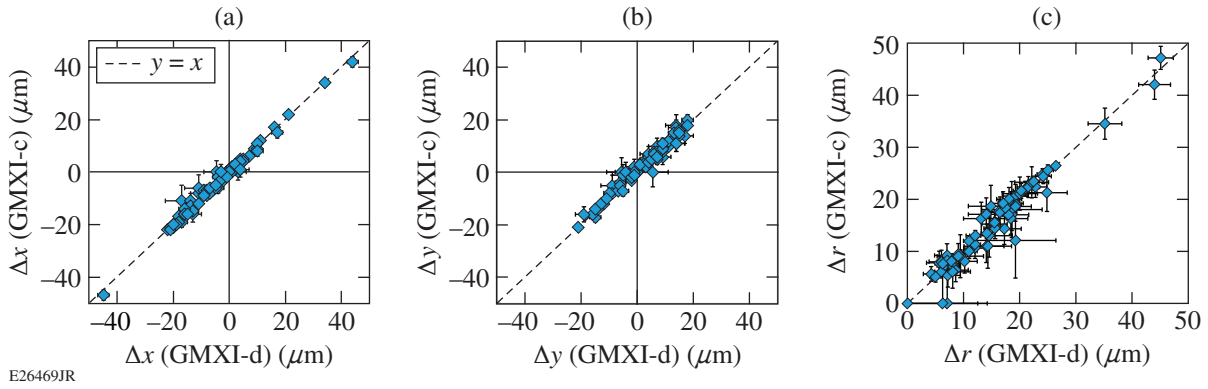

Figure 151.28

Comparisons of implosion core offset coordinates, GMXI-c against GMXI-d. Errors were calculated using the rms deviations from the lines of best fit, which are very nearly $y = x$ lines.

radial directions, respectively. The offsets in Fig. 151.29 are for a quasi-uniformly distributed sample of cryogenic target shots that span offsets from near zero to >100 μm and whose offset directions were nearly perpendicular to the GMXI view direction. Figure 151.29(a) shows that the horizontal displacement of the core is in the same direction as the t_0 offset and nearly equal in magnitude; i.e., the core is forming at approximately the position of the offset target center. In large part the core offsets confirm the accuracy of the t_0 offsets. Figure 151.30 compares the horizontal, vertical, and radial offsets of the implosion cores and the projected t_0 offsets for all recent cryogenic target shots (since 2015). The horizontal components of the t_0 and core offsets [Fig. 151.30(a)] are approximately uniformly distributed about the origin and most are <20 μm. The few large horizontal offsets agree in direction and are nearly of the same magnitude. In contrast, the vertical t_0 offsets are biased toward positive offset (in this case, from the TCC reference), whereas the core vertical offsets (y axis) are more uniformly distributed between positive and negative values. The reason for the positive bias of the t_0 vertical target offset is not known, but it is suggestive that the cryogenic targets are systematically above TCC at t_0 with an average offset of ~5 μm.

A large offset is expected to have a very detrimental effect on the fusion neutron yield, and even small offsets are calculated to have an effect on the yield under ideal simulated conditions,[13] so placing the target at TCC as accurately as possible is desired. But in real experimental conditions where many other factors may affect the implosion in addition to target offset, it may be difficult to assess the importance of target offset alone. To explore this dependence, the measured neutron yield divided by the calculated yield [yield-over-clean (YOC)] by the 1-D hydrocode *LILAC*[6] is plotted in Fig. 151.31 as a function of the measured t_0 offset for all recent cryogenic target shots (since 2015). Figure 151.31 shows that the YOC varies from ~0.2 to 0.7 for offsets less than ~15 μm and is smaller (~0.3 or less)

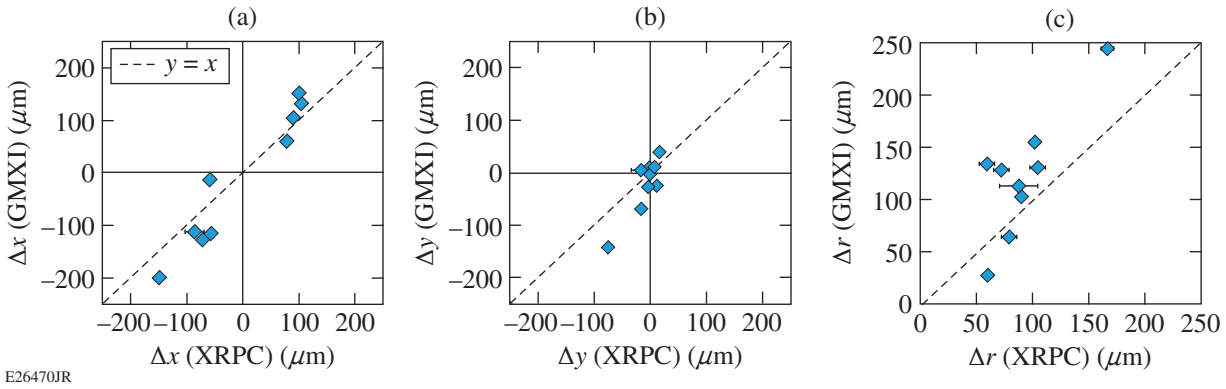

Figure 151.29
Comparisons of earlier OMEGA shots with large offset, implosion core positions against t_0 positions.

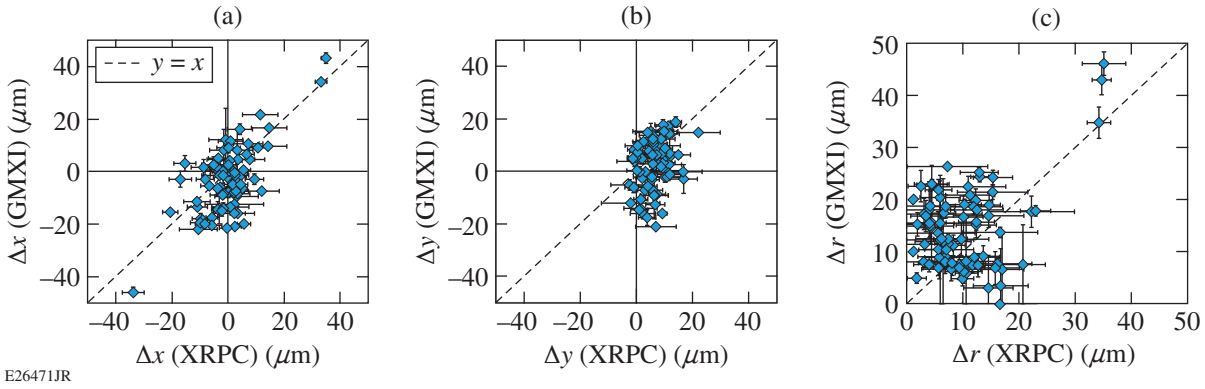

Figure 151.30
Comparisons of offset coordinates of implosion cores at image capture against the cores at time t_0.

for offsets greater than ~20 μm. These results are consistent with requiring a small offset to get a large value of the YOC but that a smaller value may be obtained at a small initial target offset for other unrelated reasons.

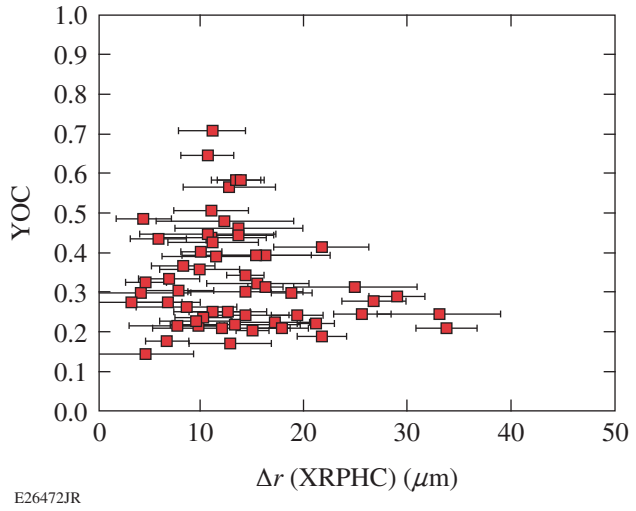

Figure 151.31
The measured cryogenic target neutron yield divided by the calculated yield ratio [yield-over-clean (YOC)] plotted as a function of the offset of the target at t_0.

Conclusions

This work describes the method for determining the offsets of cryogenic targets relative to the aim point of the OMEGA laser beams (t_0 offset) and shows measurements of the implosion core offsets from well-centered targets as determined in one direction (that of the GMXI). The t_0 offsets projected in the direction of the GMXI agree in direction and are close in magnitude to that of the core offsets with considerable scatter at small t_0 offsets (<20 μm). The approximate dependence of the YOC on target offset is such that no large YOC's are obtained when the t_0 offset is large (>20 μm). Knowing the accurate value of the t_0 offset is therefore critical in assessing the fusion performance of the implosion.

ACKNOWLEDGMENT

The authors acknowledge with gratitude the staff of the Laboratory for Laser Energetics for their work on ICF using the OMEGA Laser System. This material is based upon work supported by the Department of Energy National Nuclear Security Administration under Award Number DE-NA0001944, the University of Rochester, and the New York State Energy Research and Development Authority. The support of the DOE does not constitute an endorsement by the DOE of the views expressed in this paper.

REFERENCES

1. J. D. Lindl *et al*., Phys. Plasmas **11**, 339 (2004).
2. S. Atzeni and J. Meyer-ter-Vehn, *The Physics of Inertial Fusion: Beam Plasma Interaction, Hydrodynamics, Hot Dense Matter*, International Series of Monographs on Physics (Clarendon Press, Oxford, 2004).
3. R. Betti, K. Anderson, V. N. Goncharov, R. L. McCrory, D. D. Meyerhofer, S. Skupsky, and R. P. J. Town, Phys. Plasmas **9**, 2277 (2002).
4. E. M. Campbell and W. J. Hogan, Plasma Phys. Control. Fusion **41**, B39 (1999).
5. V. N. Goncharov, T. C. Sangster, R. Betti, T. R. Boehly, M. J. Bonino, T. J. B. Collins, R. S. Craxton, J. A. Delettrez, D. H. Edgell, R. Epstein, R. K. Follet, C. J. Forrest, D. H. Froula, V. Yu. Glebov, D. R. Harding, R. J. Henchen, S. X. Hu, I. V. Igumenshchev, R. Janezic, J. H. Kelly, T. J. Kessler, T. Z. Kosc, S. J. Loucks, J. A. Marozas, F. J. Marshall, A. V. Maximov, R. L. McCrory, P. W. McKenty, D. D. Meyerhofer, D. T. Michel, J. F. Myatt, R. Nora, P. B. Radha, S. P. Regan, W. Seka, W. T. Shmayda, R. W. Short, A. Shvydky, S. Skupsky, C. Stoeckl, B. Yaakobi, J. A. Frenje, M. Gatu-Johnson, R. D. Petrasso, and D. T. Casey, Phys. Plasmas **21**, 056315 (2014).
6. J. Delettrez, R. Epstein, M. C. Richardson, P. A. Jaanimagi, and B. L. Henke, Phys. Rev. A **36**, 3926 (1987).
7. I. V. Igumenshchev, V. N. Goncharov, F. J. Marshall, J. P. Knauer, E. M. Campbell, C. J. Forrest, D. H. Froula, V. Yu. Glebov, R. L. McCrory, S. P. Regan, T. C. Sangster, S. Skupsky, and C. Stoeckl, Phys. Plasmas **23**, 052702 (2016).
8. R. A. Forties and F. J. Marshall, Rev. Sci. Instrum. **76**, 073505 (2005).
9. F. J. Marshall, T. Ohki, D. McInnis, Z. Ninkov, and J. Carbone, Rev. Sci. Instrum. **72**, 713 (2001).
10. R. N. Bracewell, *Two-Dimensional Imaging* (Prentice Hall, Englewood Cliffs, NJ, 1995), pp. 286–288.
11. F. J. Marshall, T. DeHaas, and V. Yu. Glebov, Rev. Sci. Instrum. **81**, 10E503 (2010).
12. F. J. Marshall and J. A. Oertel, Rev. Sci. Instrum. **68**, 735 (1997).
13. S. X. Hu, P. B. Radha, J. A. Marozas, R. Betti, T. J. B. Collins, R. S. Craxton, J. A. Delettrez, D. H. Edgell, R. Epstein, V. N. Goncharov, I. V. Igumenshchev, F. J. Marshall, R. L. McCrory, D. D. Meyerhofer, S. P. Regan, T. C. Sangster, S. Skupsky, V. A. Smalyuk, Y. Elbaz, and D. Shvarts, Phys. Plasmas **16**, 112706 (2009).

Subpercent-Scale Control of 3-D Modes 1, 2, and 3 of Targets Imploded in a Direct-Drive Configuration on OMEGA

In laser-driven implosion experiments, a laser illuminates a spherical target either directly (direct-drive configuration) or after conversion into x rays (indirect-drive configuration). This absorbed laser energy leads to the ablation and extreme acceleration of the outer surface of the target through the "rocket effect." This method is widely used to study plasma physics[1] including high-energy-density physics[2–4] and inertial confinement fusion (ICF).[5] In all cases, maintaining spherical symmetry throughout the implosion is critical to obtaining a 1-D behavior that maximizes the internal energy of the imploded plasma at final compression. In ICF experiments, a capsule filled with deuterium (D) and tritium (T) is used to create a self-sustained fusion burn that will ignite the fuel and produce a net energy gain. At the end of the implosion, the kinetic energy of the imploding capsule is converted into internal energy, triggering the fusion reaction during stagnation. Several simulations and comparisons with experiments have shown that target low-mode nonuniformities lead to a severe reduction in the implosion performance because of increased residual kinetic energy during stagnation and uneven compression that result in reduced core pressure and truncated burn.[6–9] This degradation was shown to be particularly significant for modes $\ell \le 3$, where ℓ is the order of the modes of the spherical harmonic decomposition of the shell's shape.[8,10] Consequently, reducing low-mode nonuniformity has been identified as one of the most-critical steps in demonstrating ignition at the National Ignition Facility (NIF)[11–13] or conditions that are hydrodynamically equivalent to ignition when scaled from 26-kJ implosions on OMEGA to megajoule energies on the NIF.[14–16]

Over the last decade, many studies have shown significant low-mode asymmetries of the imploding shell. Modes ℓ = 1 have been typically identified from properties of the final assembly including asymmetry in its areal density,[17] variation of its ion temperature along different lines of sight,[18] hot-spot motion,[19] and asymmetric x-ray emission of a Ti layer embedded at the inner surface of the shell.[20] Modes $\ell \ge 2$ have been measured from the hot-spot shape,[21,22] standard[23] or Compton[24] radiography, x-ray absorption spectroscopy,[25] and self-emission shadowgraphy.[26]

Several studies have focused on the causes of the asymmetries and the development of methods to correct them. In indirect-drive ICF, the laser's beam-energy balance was modified to exploit cross-beam energy transfer and improve the sphericity of the core emission.[21,22] The improvement was limited, however, because the observable (i.e., the core shape) was restricted to modes $\ell \ge 2$ and too indirect to give accurate access to the 3-D structure of the shell.[10] In direct-drive ICF,[27] simulations have identified different potential effects that create nonuniformities including target offset, beam-power imbalance, beam pointing, and beam timing. Success has been limited, however, in reproducing the experimental observables obtained on OMEGA[28] because of the difficulty in evaluating and modeling each effect.

This article reports the first experimental demonstration that the amplitude of modes ℓ = 1, 2, and 3 of targets imploded in direct-drive configuration on OMEGA measured at a convergence ratio of ~3 can be controlled within ±0.25% by adjusting the laser's beam-energy balance, leading to a total radial error of 1%. Over three shots, the 3-D shape of the imploding target was tomographically recorded by measuring four lines of sight of the ablation front. The projected ablation-front contours were measured with framing cameras using the x-ray self-emission shadowgraphy technique.[26,29] The projected ablation-front motions were obtained by comparing the positions of the contours on the framing cameras with the corresponding contour positions measured on a nonimploding solid-CH-ball shot. The amplitudes of the modes were determined within ±0.15% by decomposing the contours oriented perpendicular to the lines of sight and shifted by the measured motions over spherical harmonics. The variations of the normalized target mode amplitudes (Δr_ℓ^m, where m is the mode order) between shots were shown to change linearly (within ±0.25%) with the variation of the normalized mode amplitudes of the laser's beam-energy balance $\left(\Delta e_\ell^m\right)$ with a low-mode coupling coefficient $\left(C_\ell = \Delta r_\ell^m \big/ \Delta e_\ell^m\right)$ of $C_1 = -0.66 \pm 0.05$, $C_2 = -0.38 \pm 0.05$, and $C_3 = -0.18 \pm 0.03$ for modes ℓ = 1, 2, and 3, respectively. The decrease of C_ℓ with increasing mode number was expected because of the phase plates used with each beam on OMEGA.

Lateral thermal transport and amplification by the Rayleigh–Taylor instability were not expected to be important because of the long spatial wavelength ($\lambda = 2\pi R/\ell$, where R is the averaged shell radius) of the low modes. The C_ℓ values enabled one to evaluate within ±0.05% of the amplitudes of the residual target modes that appear when the laser's beam energies are balanced and to determine the laser mode amplitudes that mitigate them within ±0.25%.

The experiments employed 60 ultraviolet ($\lambda_0 = 351$ nm) laser beams on the OMEGA Laser System.[30] The beams illuminated the target and were smoothed by polarization smoothing,[31] smoothing by spectral dispersion,[32] and distributed phase plates (fourth-order super-Gaussian with 95% of the energy contained within the initial target diameter).[33] A 2-ns-long square pulse irradiated 866±3-μm-diam capsules with an energy of 20.2±0.4 kJ, resulting in an intensity $\approx 4.3 \times 10^{14}$ W/cm^2. The shells were made of 19.2±0.2-μm-thick glow-discharge polymer (CH with a density of 1.03 mg/cm^3 and each mode amplitude <50 nm) and filled with 17±1.5 atm of deuterium. An additional reference shot was made on an 856-μm-diam solid CH ball. For each shot, the target was placed at target chamber center with a maximum radial error of 1.5 μm measured with two high-speed video cameras (1000 images per second) that were used to automatically position the target before the shot.

The first shot used a standard laser beam-energy balance with a standard deviation of 2.5%. On the second and third shots, the beam-energy balance was varied to change the amplitude of the evaluated laser modes by minimizing

$$\sum_{\mathrm{b}=1}^{60}\left[\sum_{\ell=0}^{\infty}\sum_{m=-\ell}^{\ell}\sqrt{4\pi}\,e_\ell^m\,Y_\ell^m\left(\theta_\mathrm{b},\phi_\mathrm{b}\right)-\bar{E}_\mathrm{b}\right]^2$$

with a larger variation for modes $m = 0$, where $\bar{E}_\mathrm{b}$ is the energy of the beams normalized to averaged beam energy in percent, (θ_b, ϕ_b) are the coordinates of the OMEGA beam ports, and $Y_\ell^m(\theta,\phi)$ are the tesseral spherical harmonics.[34] On the third shot, one beam was reduced by 80% as a result of hardware malfunction, further amplifying the mode amplitudes. The beam energies were measured with integrated spheres within $\delta\bar{E}_\mathrm{b} = \pm 0.5\%$ that were absolutely calibrated within ±2% with calorimeters. This resulted in the same relative error for all mode amplitudes of $\delta\left(e_\ell^m\right) = \delta\bar{E}_\mathrm{b}/\sqrt{N_\mathrm{b}} = \pm 0.06\%$, where $N_\mathrm{b} = 60$ is the number of beams.

Four x-ray framing cameras, located at different lines of sight, used arrays of 16 pinholes to image the soft x rays emitted by the irradiated target on four strips of a microchannel plate (MCP).[35] The cameras were set up to magnifications of $M = 6$ (two cameras) and $M = 4$ (two cameras) with pinhole sizes of 10 μm and 15 μm, respectively. Their point-spread functions (PSF's) result in about 2-D Gaussian convolutions of the images with a full width at half maximum of $d_\mathrm{PSF} \approx 10$ μm and $d_\mathrm{PSF} \approx 15$ μm, respectively.[26] Four short, high-voltage pulses were sent to each strip to activate the signal amplification by the MCP and obtain time-resolved images. For all imploding shells, the electrical pulses were timed to ~0.4 ns, ~1.2 ns, ~1.5 ns, and ~1.8 ns, whereas for the reference shots, they were synchronized to ~0.2 ns after the beginning of the laser pulse (defined as 1% of maximum intensity). The absolute timings between the laser pulse and the images were known to an accuracy of 20 ps, and the interstrip timings were determined within 5 ps (Refs. 26 and 36). Along each strip, the images were separated by ~50 ps. Three cameras had integration times of 40 ps; one had an integration time of 200 ps. On all cameras, 25.4-μm-thick Be filters were used to record the soft x rays above ~1 keV. For each camera, the same pinhole array was used on all shots to maintain the distance between images.

On each self-emission image, the inner edge contour of the intensity peak [Figs. 151.32(a) and 151.32(b)] corresponded to the projection of the ablation-front surface along the line of sight of the diagnostic.[29,37] The recorded intensity was the strongest near the ablation front because the emitting plasma had the largest density (which maximized its emission), and the integration distance of the emitting plasma to the detector was the longest. Just inside the ablation front, the recorded intensity dropped by a factor of 2 over a few microns as the plasma became optically thick, absorbing its emission and the emission coming from the back of the target. The time integration and spatial convolution of the diagnostic induced an inward shift, constant on a given image, of the inner gradient up to 4 μm and 20 μm for integration times of 40 ps and 200 ps, respectively.

The angular variation of the projected ablation-front surface (ΔR_θ) was determined from the difference between the angularly resolved contour radius (R_θ) and the averaged contour radius $\left(\left\langle R_\theta \right\rangle\right)$. To reduce the error, self-emission images were angularly averaged over $\Delta\theta = 20°$, which was larger than the radial convolution $\left[(360/2\pi)\,d_\mathrm{PSF}/\left(\left\langle R_\theta \right\rangle\right) < 5°\right]$ and smaller than the scale length of the modes studied here ($\lambda > 120°$). An error in R_θ of $\delta R_\theta = \pm 0.8$ μm was determined on the reference shot by fitting R_θ with a normal distribution and taking the number at the 90th percentile. This error was larger than the error in $\langle R_\theta \rangle$ of $\delta R_\theta/\sqrt{N_{\Delta\theta}} = \pm 0.2$ μm, where $N_{\Delta\theta} = 360°/\Delta\theta = 18$ is the number of independent measurements. This resulted in $\delta(\Delta R_\theta) \approx \delta R_\theta$.

On each image, the location of the projected center of the ablation-front surface on the framing camera was determined by finding the center of the circle that minimizes the standard deviation of its radial difference with the contour. This resulted in an accuracy in the center position of $\delta R_{\text{center},1} = \delta R_\theta \big/ \sqrt{N_{\Delta\theta}} = \pm 0.2\ \mu$m. The center location was corrected from the electrical-pulse (EP) propagation that introduced a displacement of the contour along the strip by $-(\Delta R)_{\text{EP}} = VM(\Delta t)_{\text{EP}}$, where V is the implosion velocity, $(\Delta t)_{\text{EP}} = V_{\text{EP}}\ \langle R_\theta \rangle M$, and V_{EP} is the electrical-pulse velocity that was characterized off-line within $\delta(V_{\text{EP}}) \big/ V_{\text{EP}} \pm 10\%$. V was determined by fitting the evolution of $\langle R_\theta \rangle$ linearly for the images of first strip [within $\delta(V) \big/ V = \pm 10\%$] and using a third-order polynomial for the other images [within $\delta(V) \big/ V = \pm 4\%$ (Ref. 26)]. The associated error of

$$\delta R_{\text{center},2} \approx (\Delta R)_{\text{EP}} \left\{ \left[\delta(V) \big/ V \right]^2 + \left[\delta(V_{\text{EP}}) \big/ V_{\text{EP}} \right]^2 \right\}^{0.5}$$

grew with time up to $\pm 0.5\ \mu$m. When the images were on the same strip, the error in V_{EP} did not affect the distance between images since it was approximately constant.

The inner edge contours were used to measure the diagnostic magnification on each shot and the magnification anisotropy for each image. On the first strip, the images were recorded at an early time so that the center of the ablation-front surface corresponded to the initial target center, making it possible to measure the diagnostic magnification $M = 1 + D/d$, where D is the distance between contours and $d > 1270\ \mu$m is the distance between pinholes. This resulted in absolute and relative accuracies of $\approx \delta d/d < \pm 0.005$ and $\approx \sqrt{2}\,\delta R_{\text{center},1} \big/ \left[(M-1)\,d \right] < \pm 5 \times 10^{-5}$, where $\delta d = \pm 15\ \mu$m is the error in the pinhole distance specified by the constructor. The error was slightly reduced by linearly fitting D and d over the recorded images. The anisotropy in the camera magnification was determined at each image position on the reference shot by measuring the contour ellipticity. On this shot, all the images were recorded at an early time so the ablation-front nonuniformities were negligible. Although this anisotropy varied among images, it was shown to be consistent at a given image position by repeating the shot.

The shift between each contour center measured on imploding capsule shots and the corresponding contour center measured on the reference shot was used to determine the projected

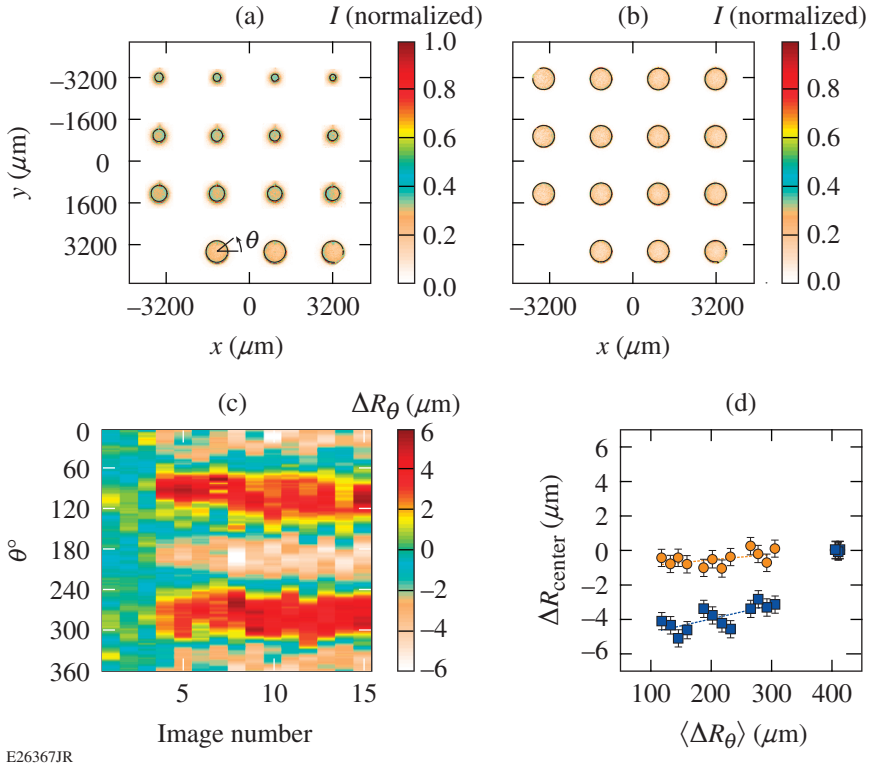

Figure 151.32
Comparison of the self-emission images recorded on (a) the second imploding capsule shot and (b) the reference shot. The circles correspond to the inner edge contours of the intensity peak. (c) Angular variations of the projected ablation-front surface (ΔR_θ) for the images in (a). (d) Projected ablation-front surface motions (ΔR_{center}) as a function of the averaged contour radius ($\langle R_\theta \rangle$) along x (orange circles) and y (blue squares) obtained by comparing the contour centers in (a) with the contour centers in (b).

motion of the ablation-front surface (ΔR_{center}). On the reference shot, each contour center corresponded to the projection of the initial target position on the diagnostic. On a capsule implosion, the contour centers determined on the first strip were aligned with the corresponding contour centers measured on the reference shot. This made it possible to correct for differences in diagnostic pointing and initial target position. Longitudinal and transverse differences were accounted for by comparing the diagnostic relative magnifications and the image locations, respectively. The error in ΔR_{center} was given by

$$\delta\left(\Delta R_{\text{center}}\right) \approx \sqrt{2}\left[\delta\left(R_{\text{center},1}\right)^2 + \delta\left(R_{\text{center},2}\right)^2\right]^{0.5} = \pm 0.8\ \mu\text{m}.$$

The best estimations of the angular variation of the projected ablation-front surface $(\Delta R_\theta)_{150}$ and motion $(\Delta R_{\text{center}})_{150}$ at an average radius of 150 μm were obtained by linearly fitting their evolution with $\langle R_\theta \rangle$ ranging from ~300 μm to ~100 μm [Figs. 151.32(c) and 151.32(d)]. These evolutions were expected to be linear since, over these radii, there was no significant change in the laser intensity, leading to an almost constant pressure applied to the target: $\Delta R \big/ \left(\langle R_\theta \rangle - R_0\right) \approx -\Delta P \big/ \langle P_\theta \rangle \approx -\beta \Delta I \big/ \langle I_\theta \rangle$, where R_0 is the initial target radius; $\langle P_\theta \rangle \propto \langle I_\theta \rangle^\beta$; $\beta \approx 0.5$ (Ref. 15); and ΔR, ΔP, and ΔI are the angular variations and $\langle R_\theta \rangle$, $\langle P_\theta \rangle$, and $\langle I_\theta \rangle$ are the angularly averaged values of the radius, pressure, and laser intensity, respectively. Errors in $(\Delta R_\theta)_{150}$ and $(\Delta R_{\text{center}})_{150}$ of $\delta(\Delta R_\theta)_{150} = \pm 0.4$ μm and $\delta(\Delta R_{\text{center}})_{150} = \pm 0.6$ μm at the 90th percentile of the error distribution were determined by comparing ΔR_θ and ΔR_{center} with their linear fits.[38]

The four measured projected contours were oriented perpendicular to the lines of sight of the corresponding framing cameras to determine the 3-D shape of the ablation-front surface [Fig. 151.33(a)]. Because of the 3-D nonuniformities, the center and averaged radii of each contour were slightly different than the center and averaged radius of the 3-D object. To account for this, one contour was used as a reference and the other contours were shifted transversally and magnified to suppress their radial differences with the reference contour at the two crossing points (i.e., where the polar and azimuthal angles are the same).

The 3-D motion of the ablation-front surface was determined by finding the point at the minimum distance between the four lines defined by the lines of sight of the framing cameras shifted by the measured projected motions and by the displacements introduced during the contour alignment process [Fig. 151.33(b)]. The four projected contours provided two measurements each of the three coordinates of the 3-D

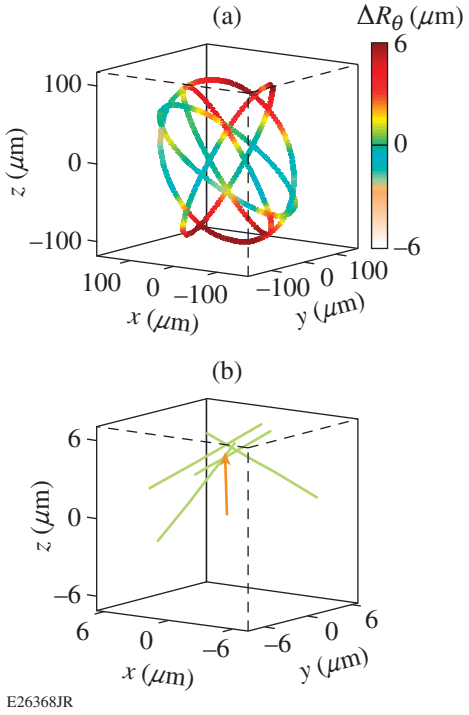

Figure 151.33
(a) The four projected ablation-front contours measured on the second imploding capsule shot were oriented perpendicular to the line of sight of the corresponding framing cameras and then shifted and magnified to minimize the radial difference at the connecting points with the reference contour. (b) The 3-D motion of the ablation-front surface (orange arrow) corresponded to the minimum distance of the four lines (green lines) defined by the lines of sight of each framing camera shifted by the measured projected motions and by the displacements introduced during the contour alignment process.

center, so the five extra measurements reduced the error in the three coordinates.

The amplitudes of modes ℓ = 1, 2, and 3 of the ablation-front surface were obtained by decomposing the four oriented contours shifted by the measured 3-D displacement using spherical harmonics

$$[\bar{R}(\theta_c, \phi_c) = \sum_{\ell=0}^{3} \sum_{m=-\ell}^{\ell} \sqrt{4\pi}\, r_\ell^m\, Y_\ell^m(\theta_c, \phi_c),$$

where $\bar{R}(\theta_c, \phi_c)$ is the radius normalized to the averaged radius in percent $(r_0^0 = 100\%)$ and (θ_c, ϕ_c) are the coordinates of the four contours]. The errors in the mode amplitudes were evaluated by simulating the previously determined error distributions of $\delta(\Delta R_{\text{center}})_{150}$ and $\delta(\Delta R_\theta)_{150}$ and fitting the errors by the normal distribution. Errors of $\delta\left(r_1^m\right) = \pm 0.15\%$, $\delta\left(r_2^m\right) = \pm 0.1\%$, and $\delta\left(r_3^m\right) = \pm 0.1\%$ were obtained at the 90th percentile for modes ℓ = 1, 2, and 3, respectively.

Figures 151.34(a)–151.34(c) show that, for each mode ℓ, the difference in the mode amplitudes of the ablation-front surface between shots Δr_ℓ^m varied linearly with the difference in the corresponding normalized mode amplitudes of the laser's beam-energy balance Δe_ℓ^m with low-mode coupling coefficients of $C_1 = -0.66\pm0.05$, $C_2 = -0.38\pm0.04$, and $C_3 = -0.18\pm0.04$. The negative values were due to the fact that the more intense the laser, the more accelerated that part of the target. The fact that the factor was the same between different shots shows that the effects that create nonuniformities other than the beam-energy balance (such as target position, beam pointing, beam timing) were reproducible between shots. Errors in Δr_ℓ^m of $\delta\left(\Delta r_\ell^m\right) = \pm0.25\%$, $\delta\left(\Delta r_2^m\right) = \pm0.3\%$, and $\delta\left(\Delta r_1^m\right) = \pm0.3\%$ at the 90th percentile were obtained by comparing the points with their linear fits. These comparisons were also used to determine the errors at the 90th percentile of C_ℓ.

The decrease of C_ℓ with mode number [Fig. 151.34(d)] was caused by the phase plates that reduced the amplitude of the modes on target.[39] The laser mode on target is given by

$$\tilde{E}(\theta,\phi) = \sum_{\ell=0}^{\infty}\sum_{m=-\ell}^{\ell}\sqrt{4\pi}\,\tilde{e}_0^0\,Y_\ell^m(\theta,\phi),$$

where $\tilde{e}_\ell^m = a_\ell \sum_{b=1}^{60} \bar{E}_b Y_\ell^m(\theta_b,\phi_b) \approx a_\ell e_\ell^m$; a_ℓ are coefficients that describe the profile of each beam,

$$\tilde{E}_b(\theta,\phi) = \bar{E}_b \sum_{\ell=1}^{\infty} a_\ell (2\ell+1) \Big/ 4\pi P_\ell(\cos\gamma)$$

normalized to have $\tilde{e}_0^0 = 100\%$, P_ℓ is the Legendre polynomials, and γ is the angle between (θ, ϕ) and (θ_b, ϕ_b). The SG5 phase plates reduced the values of modes 1, 2, and 3 by factors of 0.79, 0.47, and 0.2, respectively, which result in a constant $C_\ell \big/ a_\ell = 0.85\pm0.07$ that relate the laser modes on target to the target modes [Fig. 151.34(d)].

The values of $C_\ell \big/ a_\ell = \Delta R \big/ \langle R_\theta \rangle \times \langle I_\theta \rangle \big/ \Delta I$ resulted in

$$\beta \approx -150 \big/ (150 - R_0) \times C_\ell \big/ a_\ell \approx 0.44\pm0.035,$$

which was close to the theoretical value of 0.5. This shows that the smoothing of the laser modes by the lateral heat transport[40] and the amplification by the Rayleigh–Taylor instability were negligible for those modes, as expected.

These linear evolutions allowed us to determine the residual target mode amplitudes $\left[(r_{res})_\ell^m\right]$ that remain when the laser

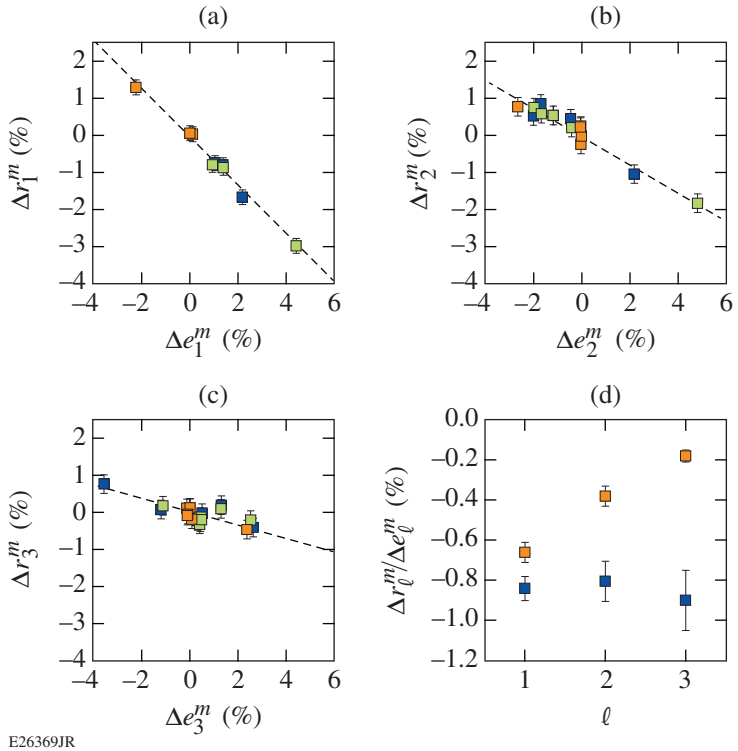

Figure 151.34
Comparison of the difference in the amplitude of the modes (a) $\ell = 1$, (b) $\ell = 2$, and (c) $\ell = 3$ of the ablation-front surface $\left(\Delta r_\ell^m\right)$ between shots 1 and 2 (orange points), 1 and 3 (blue points), and 2 and 3 (green points) with the difference in the corresponding modes in the laser-energy balance $\left(\Delta e_\ell^m\right)$. The linear fits are plotted in (a)–(c) as dashed black lines. (d) Comparison of C_ℓ (orange points) with $C_\ell \big/ a_\ell$ (blue points).

beam energies are balanced and the optimum laser-mode amplitudes that compensate them $\left[(e_{\rm opt})_\ell^m\right]$. Over the three measurements $(r_{\rm res})_\ell^m$ is obtained by averaging $(r_{\rm res})_\ell^m = r_\ell^m - C_\ell e_\ell^m$ with an associated error of $\delta(r_{\rm res})_\ell^m \approx \delta(r_\ell^m)/\sqrt{3} = \pm 0.05\%$; $(e_{\rm opt})_\ell^m$ is given by $(e_{\rm opt})_\ell^m = -(r_{\rm res})_\ell^m / C_\ell$. Applying these corrected laser modes would lead to a spherical implosion with a maximum radial error

$$\approx \left\{\sum_{\ell=0}^{3}\sum_{m=-\ell}^{\ell}\left[\delta\left(\Delta r_\ell^m\right)^2\right]\right\}^{0.5} = \pm 1\%.$$

In summary, tomographies of imploding shells were used to determine the laser energy balance that suppresses target modes ℓ = 1, 2, and 3. This is essential in direct-drive implosion experiments including ICF, where 3-D simulations predict significant enhancement in fusion performance.[8]

ACKNOWLEDGMENT

This material is based upon work supported by the Department of Energy National Nuclear Security Administration under Award Number DE-NA0001944, the University of Rochester, and the New York State Energy Research and Development Authority. The support of DOE does not constitute an endorsement by DOE of the views expressed in this article.

REFERENCES

1. R. P. Drake, *High-Energy-Density Physics: Fundamentals, Inertial Fusion, and Experimental Astrophysics, Shock Wave and High Pressure Phenomena* (Springer, Berlin, 2006).

2. A. L. Kritcher, T. Doeppner, D. Swift, J. Hawreliak, J. Nilsen, J. Hammer, B. Bachmann, G. Collins, O. Landen, C. Keane, S. Glenzer, S. Rothman, D. Chapman, D. Kraus, and R. W. Falcone, J. Phys.: Conf. Ser. **688**, 012055 (2016).

3. R. Nora, W. Theobald, R. Betti, F. J. Marshall, D. T. Michel, W. Seka, B. Yaakobi, M. Lafon, C. Stoeckl, J. A. Delettrez, A. A. Solodov, A. Casner, C. Reverdin, X. Ribeyre, A. Vallet, J. Peebles, F. N. Beg, and M. S. Wei, Phys. Rev. Lett. **114**, 045001 (2015).

4. A. B. Zylstra, J. A. Frenje, P. E. Grabowski, C. K. Li, G. W. Collins, P. Fitzsimmons, S. Glenzer, F. Graziani, S. B. Hansen, S. X. Hu, M. Gatu Johnson, P. Keiter, H. Reynolds, J. R. Rygg, F. H. Séguin, and R. D. Petrasso, Phys. Rev. Lett. **114**, 215002 (2015).

5. J. Nuckolls *et al*., Nature **239**, 139 (1972).

6. O. A. Hurricane *et al*., Nature **506**, 343 (2014).

7. S. P. Regan, V. N. Goncharov, I. V. Igumenshchev, T. C. Sangster, R. Betti, A. Bose, T. R. Boehly, M. J. Bonino, E. M. Campbell, D. Cao, T. J. B. Collins, R. S. Craxton, A. K. Davis, J. A. Delettrez, D. H. Edgell, R. Epstein, C. J. Forrest, J. A. Frenje, D. H. Froula, M. Gatu Johnson, V. Yu. Glebov, D. R. Harding, M. Hohenberger, S. X. Hu, D. Jacobs-Perkins, R. T. Janezic, M. Karasik, R. L. Keck, J. H. Kelly, T. J. Kessler, J. P. Knauer, T. Z. Kosc, S. J. Loucks, J. A. Marozas, F. J. Marshall, R. L. McCrory, P. W. McKenty, D. D. Meyerhofer, D. T. Michel, J. F. Myatt, S. P. Obenschain, R. D. Petrasso, R. B. Radha, B. Rice, M. Rosenberg, A. J. Schmitt, M. J. Schmitt, W. Seka, W. T. Shmayda, M. J. Shoup, III, A. Shvydky, S. Skupsky, A. A. Solodov, C. Stoeckl, W. Theobald, J. Ulreich, M. D. Wittman, K. M. Woo, B. Yaakobi, and J. D. Zuegel, Phys. Rev. Lett. **117**, 025001 (2016); **117**, 059903(E) (2016).

8. I. V. Igumenshchev, V. N. Goncharov, F. J. Marshall, J. P. Knauer, E. M. Campbell, C. J. Forrest, D. H. Froula, V. Yu. Glebov, R. L. McCrory, S. P. Regan, T. C. Sangster, S. Skupsky, and C. Stoeckl, Phys. Plasmas **23**, 052702 (2016).

9. P. B. Radha, V. N. Goncharov, T. J. B. Collins, J. A. Delettrez, Y. Elbaz, V. Yu. Glebov, R. L. Keck, D. E. Keller, J. P. Knauer, J. A. Marozas, F. J. Marshall, P. W. McKenty, D. D. Meyerhofer, S. P. Regan, T. C. Sangster, D. Shvarts, S. Skupsky, Y. Srebro, R. P. J. Town, and C. Stoeckl, Phys. Plasmas **12**, 032702 (2005).

10. B. K. Spears, M. J. Edwards, S. Hatchett, J. Kilkenny, J. Knauer, A. Kritcher, J. Lindl, D. Munro, P. Patel, H. F. Robey, and R. P. J. Town, Phys. Plasmas **21**, 042702 (2014).

11. S. W. Haan *et al*., Phys. Plasmas **18**, 051001 (2011).

12. A. Kritcher *et al*., "Integrated Modeling of Cryogenic Layered High-Foot Experiments at the NIF," submitted to Physics of Plasmas.

13. D. S. Clark *et al*., Phys. Plasmas **23**, 056302 (2016).

14. R. L. McCrory, R. E. Bahr, R. Betti, T. R. Boehly, T. J. B. Collins, R. S. Craxton, J. A. Delettrez, W. R. Donaldson, R. Epstein, J. Frenje, V. Yu. Glebov, V. N. Goncharov, O. Gotchev, R. Q. Gram, D. R. Harding, D. G. Hicks, P. A. Jaanimagi, R. L. Keck, J. Kelly, J. P. Knauer, C. K. Li, S. J. Loucks, L. D. Lund, F. J. Marshall, P. W. McKenty, D. D. Meyerhofer, S. F. B. Morse, R. D. Petrasso, P. B. Radha, S. P. Regan, S. Roberts, F. Séguin, W. Seka, S. Skupsky, V. Smalyuk, C. Sorce, J. M. Soures, C. Stoeckl, R. P. J. Town, M. D. Wittman, B. Yaakobi, and J. D. Zuegel, Nucl. Fusion **41**, 1413 (2001).

15. V. N. Goncharov, S. P. Regan, E. M. Campbell, T. C. Sangster, P. B. Radha, J. F. Myatt, D. H. Froula, R. Betti, T. R. Boehly, J. A. Delettrez, D. H. Edgell, R. Epstein, C. J. Forrest, V. Yu. Glebov, D. R. Harding, S. X. Hu, I. V. Igumenshchev, F. J. Marshall, R. L. McCrory, D. T. Michel, W. Seka, A. Shvydky, C. Stoeckl, W. Theobald, and M. Gatu-Johnson, Plasma Phys. Control. Fusion **59**, 014008 (2017).

16. K. Molvig *et al*., Phys. Rev. Lett. **116**, 255003 (2016).

17. C. K. Li, F. H. Séguin, J. A. Frenje, R. D. Petrasso, J. A. Delettrez, P. W. McKenty, T. C. Sangster, R. L. Keck, J. M. Soures, F. J. Marshall, D. D. Meyerhofer, V. N. Goncharov, J. P. Knauer, P. B. Radha, S. P. Regan, and W. Seka, Phys. Rev. Lett. **92**, 205001 (2004).

18. T. J. Murphy, Phys. Plasmas **21**, 072701 (2014).

19. J. J. Ruby, A. Pak, J. E. Field, T. Ma, B. K. Spears, L. R. Benedetti, D. K. Bradley, L. F. Berzak Hopkins, D. T. Casey, T. Döppner, D. Eder, D. Fittinghoff, G. Grim, R. Hatarik, D. E. Hinkel, N. Izumi, J. D. Kilkenny, S. F. Khan, J. P. Knauer, A. L. Kritcher, F. E. Merrill, J. D. Moody, S. R. Nagel, H.-S. Park, J. D. Salmonson, D. B. Sayre, D. A. Callahan, W. W. Hsing, O. A. Hurricane, P. K. Patel, and M. J. Edwards, Phys. Plasmas **23**, 072701 (2016).

20. R. C. Shah, B. M. Haines, F. J. Wysocki, J. F. Benage, J. A. Fooks, V. Glebov, P. Hakel, M. Hoppe, I. V. Igumenshchev, G. Kagan, R. C. Mancini, F. J. Marshall, D. T. Michel, T. J. Murphy, M. E. Schoff, K. Silverstein, C. Stoeckl, and B. Yaakobi, Phys. Rev. Lett. **118**, 135001 (2017).

21. P. Michel *et al*., Phys. Plasmas **17**, 056305 (2010).

22. G. A. Kyrala *et al*., Phys. Plasmas **18**, 056307 (2011).

23. R. P. J. Town, D. K. Bradley, A. Kritcher, O. S. Jones, J. R. Rygg, R. Tommasini, M. Barrios, L. R. Benedetti, L. F. Berzak Hopkins, P. M. Celliers, T. Döppner, E. L. Dewald, D. C. Eder, J. E. Field, S. M. Glenn, N. Izumi, S. W. Haan, S. F. Khan, J. L. Kline, G. A. Kyrala, T. Ma, J. L. Milovich, J. D. Moody, S. R. Nagel, A. Pak, J. L. Peterson, H. F. Robey, J. S. Ross, R. H. H. Scott, B. K. Spears, M. J. Edwards, J. D. Kilkenny, and O. L. Landen, Phys. Plasmas **21**, 056313 (2014).

24. R. Tommasini, S. P. Hatchett, D. S. Hey, C. Iglesias, N. Izumi, J. A. Koch, O. L. Landen, A. J. MacKinnon, C. Sorce, J. A. Delettrez, V. Yu. Glebov, T. C. Sangster, and C. Stoeckl, Phys. Plasmas **18**, 056309 (2011).

25. H. M. Johns, R. C. Mancini, T. Nagayama, D. C. Mayes, R. Tommasini, V. A. Smalyuk, S. P. Regan, and J. A. Delettrez, Phys. Plasmas **23**, 012709 (2016).

26. D. T. Michel, A. K. Davis, W. Armstrong, R. Bahr, R. Epstein, V. N. Goncharov, M. Hohenberger, I. V. Igumenshchev, R. Jungquist, D. D. Meyerhofer, P. B. Radha, T. C. Sangster, C. Sorce, and D. H. Froula, High Power Laser Sci. Eng. **3**, e19 (2015).

27. R. S. Craxton, K. S. Anderson, T. R. Boehly, V. N. Goncharov, D. R. Harding, J. P. Knauer, R. L. McCrory, P. W. McKenty, D. D. Meyerhofer, J. F. Myatt, A. J. Schmitt, J. D. Sethian, R. W. Short, S. Skupsky, W. Theobald, W. L. Kruer, K. Tanaka, R. Betti, T. J. B. Collins, J. A. Delettrez, S. X. Hu, J. A. Marozas, A. V. Maximov, D. T. Michel, P. B. Radha, S. P. Regan, T. C. Sangster, W. Seka, A. A. Solodov, J. M. Soures, C. Stoeckl, and J. D. Zuegel, Phys. Plasmas **22**, 110501 (2015).

28. I. V. Igumenshchev, D. T. Michel, R. C. Shah, E. M. Campbell, R. Epstein, C. J. Forrest, V. Yu. Glebov, V. N. Goncharov, J. P. Knauer, F. J. Marshall, R. L. McCrory, S. P. Regan, T. C. Sangster, C. Stoeckl, A. J. Schmitt, and S. Obenschain, Phys. Plasmas **24**, 056307 (2017).

29. D. T. Michel, C. Sorce, R. Epstein, N. Whiting, I. V. Igumenshchev, R. Jungquist, and D. H. Froula, Rev. Sci. Instrum. **83**, 10E530 (2012).

30. T. R. Boehly, D. L. Brown, R. S. Craxton, R. L. Keck, J. P. Knauer, J. H. Kelly, T. J. Kessler, S. A. Kumpan, S. J. Loucks, S. A. Letzring, F. J. Marshall, R. L. McCrory, S. F. B. Morse, W. Seka, J. M. Soures, and C. P. Verdon, Opt. Commun. **133**, 495 (1997).

31. T. R. Boehly, V. A. Smalyuk, D. D. Meyerhofer, J. P. Knauer, D. K. Bradley, R. S. Craxton, M. J. Guardalben, S. Skupsky, and T. J. Kessler, J. Appl. Phys. **85**, 3444 (1999).

32. S. Skupsky, R. W. Short, T. Kessler, R. S. Craxton, S. Letzring, and J. W. Soures, J. Appl. Phys. **66**, 3456 (1989).

33. T. J. Kessler, Y. Lin, J. J. Armstrong, and B. Velazquez, Proc. SPIE **1870**, 95 (1993).

34. E. T. Whittaker and G. N. Watson, *A Course of Modern Analysis* (Cambridge University Press, 1927), p. 392.

35. D. K. Bradley, P. M. Bell, J. D. Kilkenny, R. Hanks, O. Landen, P. A. Jaanimagi, P. W. McKenty, and C. P. Verdon, Rev. Sci. Instrum. **63**, 4813 (1992).

36. D. T. Michel, V. N. Goncharov, I. V. Igumenshchev, R. Epstein, and D. H. Froula, Phys. Rev. Lett. **111**, 245005 (2013).

37. D. T. Michel, S. X. Hu, A. K. Davis, V. Yu. Glebov, V. N. Goncharov, I. V. Igumenshchev, P. B. Radha, C. Stoeckl, and D. H. Froula, Phys. Rev. E **95**, 051202(R) (2017).

38. H. L. Seal, Biometrika **54**, 1 (1967).

39. S. Skupsky and K. Lee, J. Appl. Phys. **54**, 3662 (1983).

40. L. Spitzer, Jr. and R. Härm, Phys. Rev. **89**, 977 (1953).

The Effect of Tritium-Induced Damage on Plastic Targets from High-Density DT Permeation

Introduction

Direct-drive inertial fusion experiments on LLE's OMEGA Laser System[1] and indirect-drive experiments at Lawrence Livermore National Laboratory's (LLNL's) National Ignition Facility[2] use glow-discharge polymer (GDP) as the capsule material that contains the cryogenic DT fusion fuel.[3] Knowledge of the outside diameter of the capsule and the fuel layer's thickness and uniformity are critical so that appropriate laser conditions can be set for the implosion experiment.

Cryogenic targets measured in the cryogenic target Characterization Stations have had greater than expected outside diameters (OD's) (up to 13 μm) from thermal contraction after cooling. The expected diameters were calculated from the General Atomics' (GA's) National Institute of Standards and Technology (NIST)-traceable, room-temperature–measured OD value and the coefficient of thermal expansion of GDP; this contraction was not observed. As a secondary effect, mismeasurement of the OD can influence the reported fuel-layer thickness. To examine this effect, several experiments were performed including (1) an optical system calibration check; (2) a comparison of OD's measured in the cryogenic system with a NIST-traceable value (864.1±0.5-μm-OD silicon ball measured at GA); (3) a parametric study of how system variables can affect the OD measurement; and (4) a comparison of an opaque sphere versus a transparent sphere.

Experimental Configuration

1. Optical System Description

Cryogenic targets are characterized[4] using the non-telecentric, *f*/5, long-working-distance objective shown in Fig. 151.35. The target is illuminated with a pulsed 630-nm-wavelength light-emitting diode (LED) to minimize the effects of target vibration. This wavelength, along with the *f*/5 optics, gives a diffraction-limited (Rayleigh criterion) resolution of 3.8 μm. A 1000 × 1000-sq-pixel, 12-bit charge-coupled device (CCD) is used to record an image of the target. This gives a 1-μm pixel size given the 1-mm object-space field of view; the image is oversampled and there is no loss in resolution resulting from the pixel size.

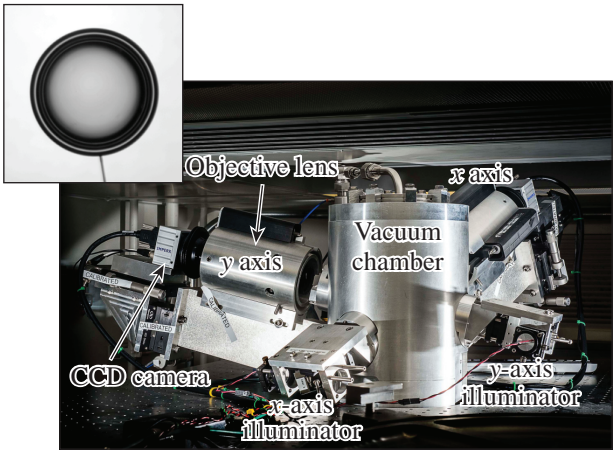

E26202JR

Figure 151.35
Characterization Station used to determine the thickness and uniformity of the solid DT layer. The fuel is layered in a cryogenic enclosure ("layering sphere") filled with He gas that transports heat caused by beta decay of the DT from the capsule. A layered capsule mounted on a SiC fiber is shown in the inset. CCD: charge-coupled device.

2. Image Analysis

The optical system is calibrated (μm/pixel) with a "grid target" that consists of an array of opaque 10-μm-diam aluminum dots that are 20 μm apart on center to within 0.1 μm (see Fig. 151.36). The distortion of the image and centration of the optical axis of the imaging system are also measured and corrected, if necessary, using this grid. Periodic confirmation of calibration using the grid target is performed, especially after any changes are made to the optical path of the system, such as replacing windows or adjusting the optical axis.

To find the outside diameter, 360 radii of the target's image are traced from the center of the capsule. The region where the intensity transition from dark to light is analyzed, the locations where the intensity begins to transition from the local minimum to the local maximum are determined, and the halfway point between them is deemed the perimeter of the target. [See Fig. 151.39 (p. 162) for an example of a radius versus angular position plot.] The target's radius is then calculated using the

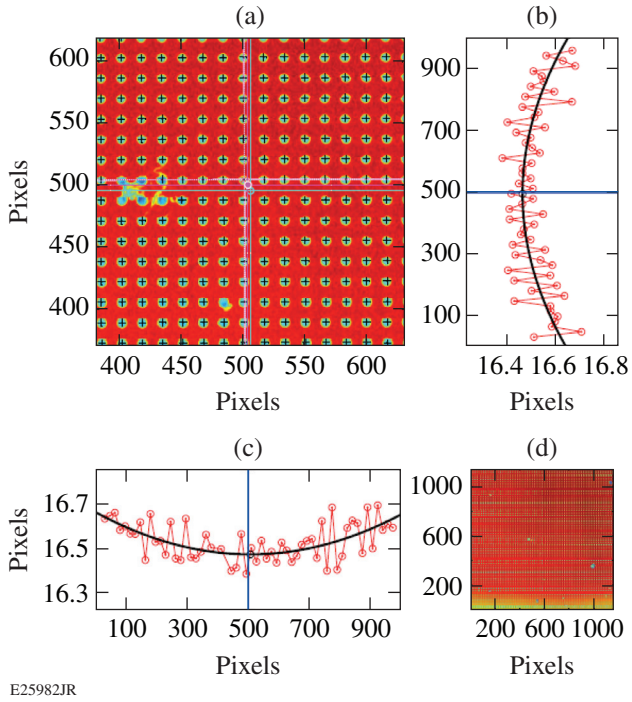

Figure 151.36
Typical calibration images for the Characterization Stations; the image in (a) is the central region of the entire field shown in (d). The locations of the dot centers are compared to the known spacing to calibrate the optical system. Plots used to correct distortion are shown on each side of the central region; the pixel spacing between dot centers is plotted as a function of position in the field for the (b) vertical and (c) horizontal directions. In addition, the optical system is adjusted to remove any skew in these plots to ensure that the capsule is centered on the objective's optical axis.

calibrated μm/pixel value; the OD is given by doubling that number. The diffraction-limited resolution of the optical system is 3.8 μm, but the radius is sampled every degree (360 times) around the perimeter (with some measurements discarded because of the stalk). The theoretical uncertainty in the measured radius could be as low as $3.8/\sqrt{360} = 0.2$ μm. This is doubled when quoting the diameter, so agreement to 0.5 μm should be expected. The diffraction limit is seldom achieved in real systems, however, because of additional sources of aberration such as spherical aberration produced by viewing through the vacuum windows.

Calibration Verification

1. Optical Calibration Confirmation

A grid target (manufactured by Applied Image[5]) identical to the one currently being used with the Characterization Stations was measured with a compound microscope that had been calibrated using a Nikon stage reticule. It was the same grid target that was used when evaluating the cryo target characterization technique off-line during the technique's development. The accuracy of the microscope was also confirmed by correctly measuring a NIST-traceable, standard 1-mm-diam ball.

Using the traveling stage, 30 dots traversed the eyepiece cross hairs in both the x (parallel to stalk) and y (perpendicular to stalk) directions. The measured distances of x = 599.8 μm and y = 599.2 μm give a dot pitch in the x direction of 19.99 μm and in the y direction of 19.97 μm, which agrees with the manufacturer's quoted pitch of 20.0±0.1 μm.

2. Analysis Software Confirmation

To examine the reliability of the analysis software, synthetic data were generated and analyzed with the program. The analysis software reproduced exactly the quantities used to produce the synthetic data.

Possible Sources of Error in OD Measurement

Several parameters were varied to determine their effect on the measured outside diameter as summarized in Table 151.II.

Table 151.II: Effects of parameters studied on the measured OD of the Si ball.

Parameter studied	Effect
Illumination intensity	Effect if background is saturated
Illumination geometry (numerical aperture)	No effect
Focus shift	Effect only if image is conspicuously out of focus
Position of the capsule along the optical axis of the imaging system (image refocused)	No effect
Position of the capsule laterally in the field of view	No effect
Characterization station	No effect
Moving Cryostat Transfer Cart	No effect
Opaque versus transparent sphere	No effect

1. Image Illumination

We first studied the saturation of the camera surrounding the capsule's image and its effect on the diameter reported by the software analysis. A GA-measured (864.1±0.5-μm-outer-diam) silicon (Si) ball was measured using Characterization Station #3. Examples shown in Fig. 151.37 give the measured outside diameters and LED currents that produced the images.

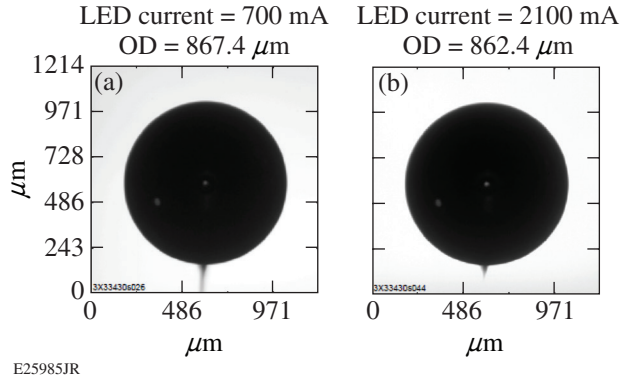

Figure 151.37
Change in apparent diameter of the Si ball resulting from saturation of the camera surrounding the capsule's image. The diameter reported by the software analysis and light-emitting diode (LED) current of the illumination diode is given for (a) a properly illuminated image and (b) an image with a saturated background.

It was noted at this point in the study that the program is reporting a slightly larger OD (867.4 μm) even with appropriate illumination.

The effects of illumination were then tested with a poly α-methyl styrene (PAMS) capsule with a GA-reported outside diameter of 867.4 μm (wall thickness = 19.2 μm). Results for the x-axis view are shown in Fig. 151.38 along with the LED currents that produced the images. In Fig. 151.38(a), when properly illuminated so that the full dynamic range of the camera is utilized, the OD of the x axis is 869.2 μm and the OD of the y axis is 871.2 μm. Figure 151.38(b) is underilluminated and the OD is slightly overestimated: x-axis OD = 869.4 μm; y-axis OD = 871.6 μm. Figure 151.38(c) is clearly saturated and the OD is significantly underestimated: x-axis OD = 862.2 μm; y-axis OD = 859.8 μm. The program is still reporting a slightly larger OD even with proper illumination. Note that the x-axis OD is closer to the GA value than the y-axis OD with proper illumination. The source of this discrepancy is unclear since the Si ball's OD measured the same in both axes. It may be an effect of the capsule's transparency and the illumination nonuniformity present in the frame; this is evident in the offset central bright region inside the capsule's image.

The error in Fig. 151.38(b) may be caused by noise in the image that is clearly visible in the capsule's darker periphery; note that the error is small when compared with Fig. 151.38(a). The OD in Fig. 151.38(c) was underestimated because of "blooming." At saturation, pixels lose their ability to accommodate additional charge. This additional charge will then spread into neighboring pixels, causing them to either report erroneous values or also saturate. This spread of charge to adjacent pixels is known as blooming.

To prevent saturation, the pixel values in the background of the image are displayed by the software in real time by analyzing the image. After it is confirmed that the image is not saturated, data are recorded and analyzed. Only images with the correct illumination are collected for analysis; other than the systematic error of an ~3-μm overestimate of the OD, image illumination is not the source of OD discrepancy.

2. Illumination Geometry

Another test to see if the OD measurement was sensitive to the illuminating ray bundle was performed by adjusting the illuminator's aperture to control the distribution of the rays coming from the light source. Three aperture conditions were tested: 100%, 50%, and 10% open. The 10%-open condition produced distinct diffraction rings around the image of the Si ball, whereas the others only reduced the intensity of the image. The intensity was adjusted to give the same background intensity for each condition, and images were captured and evaluated. All gave the same OD value as previous experiments: the measurement overestimated the OD by about 3 μm.

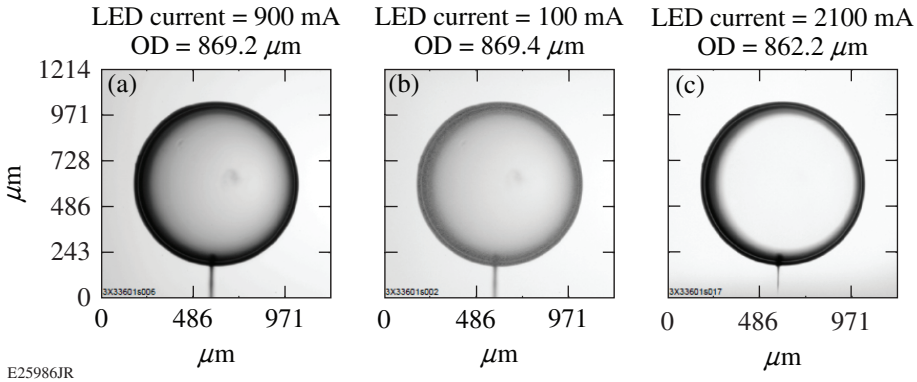

Figure 151.38
Effect of illumination intensity on the apparent diameter of the poly α-methyl styrene (PAMS) capsule. The diameter reported by the software analysis along the x viewing axis and the LED current of the illumination diode are given for (a) a properly illuminated image, (b) an underilluminated image, and (c) an image with a saturated background.

3. Focus Shift

Since the imaging systems in the Characterization Stations are not telecentric, the apparent diameter changes with focus adjustment. When examining the target's surface for debris, the focus is shifted by several hundred micrometers. Returning to the "best focus" after these adjustments is subjective and may be operator dependent. In addition, the target can move in and out of focus because of vibration around its best-focus position.

An experiment was performed to test the effect of moving the Si ball out of the focal plane while holding the objective's focal plane fixed; these results are summarized in Fig. 151.39. The radial unwrapping of each image, shown below the image, indicates the degree of blurring in its perimeter. The line is the location determined by the analysis software to be the edge of the ball. Images of the silicon ball were obtained with it shifted both toward and away from the objective lens by up to 85 μm [Fig. 151.39(b)] in 17-μm steps. The focus control on the objective was not adjusted to compensate for the shift. The measured OD was reproduced within ± 0.5 μm of its average of 867.4 μm for all of the images.

This test was repeated, but this time the focus control on the objective *was* adjusted to compensate for the shift. The remeasured OD was reproduced within ± 0.5 μm of its average of 868.4 μm for all of the images; this time the average was 1 μm larger, most likely because of the lack of telecentricity of the objective lens.

To test the operator's reproducibility to refocus the objective lens, the Si ball was centered in the layering sphere and the objective's focus knob was turned to produce a noticeably out-of-focus image. An image was taken, the objective was refocused, and a second image was taken. This was repeated 15 times and the OD of the refocused images had an average of 867.4 μm with a standard deviation of ± 0.2 μm. The analysis software is surprisingly robust in that it underreported the OD by up to 6 μm, even for the grossly out-of-focus images [Fig. 151.39(c)]. Figures 151.39(a) and 151.39(b) demonstrate that the OD can be reproduced exactly, even when slightly unfocused.

Images of the PAMS capsule were also obtained with it shifted both toward and away from the objective lens by up to

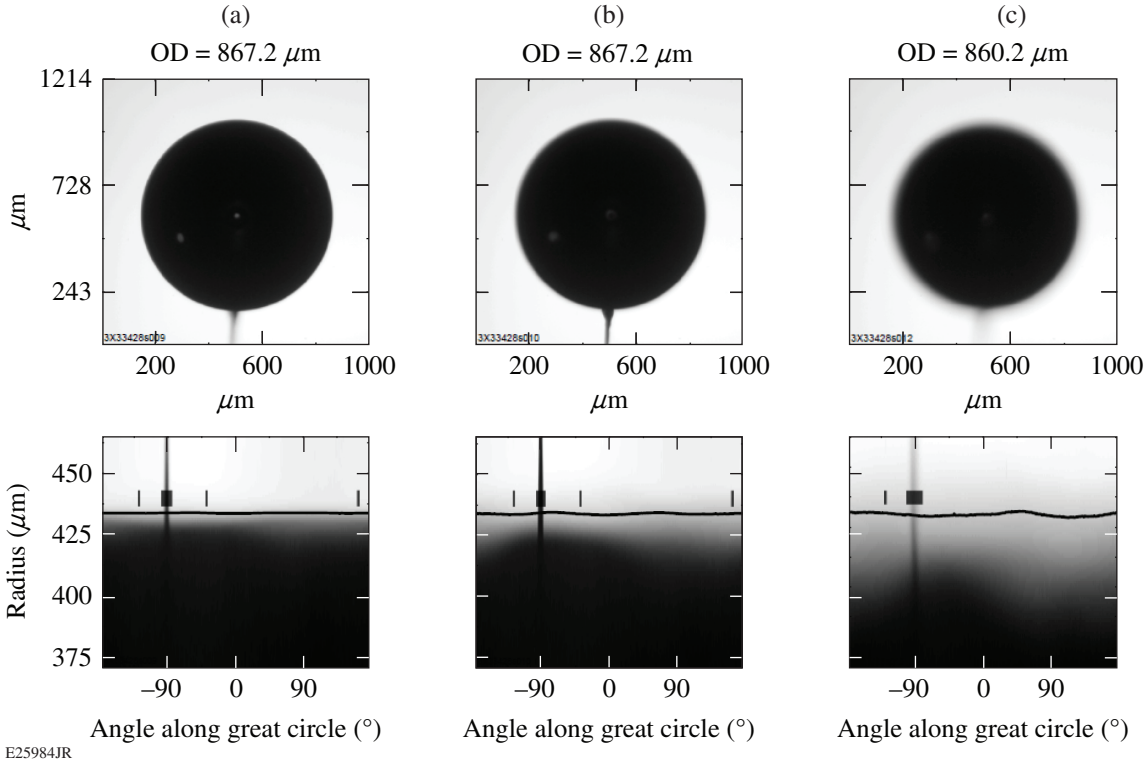

Figure 151.39

Several images taken during the focus scan: (a) Si ball at focal plane; (b) 85 μm away from focal plane; and (c) deliberately out of focus. The radial unwrapping of each image, shown below the image, indicates the degree of blurring in its perimeter. The line is the location determined by the analysis software to be the edge of the ball. Note that the blurring also overestimates the asymmetry of the capsule's OD, as indicated by the increased undulation of the line.

45 μm. In this test, the focus control on the objective was not adjusted to compensate for the shift. The measured OD's were reproduced within ±0.5 μm of their average of 869.2 μm for all of the images.

A lineout along the diameter would allow the operator to more objectively determine best focus in real time. However, the OD measurement is not sensitive to being slightly out of focus, certainly within the operator's qualitative ability to choose the correct focus.

4. Lateral Shift from Center

Since a cryogenic target is often vibrating both in and out of focus and laterally in the image during data acquisition, the sensitivity of the OD measurement to a lateral shift in the field of view was tested. As the capsule was shifted toward and away from the lens along the *x* axis in the focus-scan test, images were recorded along the *y* axis to determine if the measured OD changed with lateral position in the field of view. No difference in OD was measured even at extremes in lateral shift.

5. Characterization Station

The Cryogenic Target Facility contains three identical Characterization Stations. The Si ball was imaged in the same Moving Cryostat Transport Cart (MCTC) in all three stations; each was adjusted to the same illumination and focus conditions. The results are shown in Table 151.III. There was no statistical difference in OD measurement among the three stations.

6. Moving Cryostat Transfer Cart

During cryogenic target experiments, the capsule is stored, layered, transported, and characterized in a cryostat contained in a MCTC.[6] There is some slight variation in window thickness and alignment between the layering spheres in these carts. The data shown in Table 151.III were taken with the Si ball in MCTC #2. The ball was transferred into MCTC #7 and characterized at Characterization Station #3. Using the same illumination and focus conditions, no difference was observed between the measurements made in each cart.

Table 151.III: Comparison of the outside diameter of the Si ball measured at the three different Characterization Stations. The GA-measured OD = 864.1±0.5 μm, which is 3 μm less than the average of 866.8±0.3 μm for both axes shown here.

Characterization Station	*x*-axis OD (μm)	*y*-axis OD (μm)
1	867.0	867.4
2	866.2	866.8
3	866.6	866.8
Mean±σ	866.6±0.3	867.0±0.3

7. Warm Versus Cold Layering Sphere

The Si ball was cooled to 19 K in MCTC #2 at Characterization Station #3 and remeasured. The OD shrunk by, at most, 0.4 μm, as expected from the small thermal expansion coefficient of silicon. There was no statistical difference between the room-temperature and cryogenic measurements.

Data Analysis

1. Contraction of Cold, Unfilled, and D_2-filled Capsules

Images of two cold, unfilled GDP capsules were taken at 90° rotation intervals along both the *x*- and *y*-axis views, and the average OD was determined from each. These data, summarized in Table 151.IV, indicated that GDP capsules *do* contract when cooled; the difference being that they were

Table 151.IV: Change in OD after cooling from 293 K to 19 K for a sample of GDP shells that have *not* been exposed to DT. (The cold OD was reduced by 3 μm from the actual measurement to correct for the systematic error revealed during calibration testing.) The average change is 12.9±0.3 μm as expected from the thermal contraction calculated from the coefficient of thermal expansion and the temperature change.[12]

Capsule Type	Target Number	Outer Diameter (μm)				Average change (μm, corrected)	Percent change (corrected)
		Warm *x* axis	Warm *y* axis	Cold *x* axis	Cold *y* axis		
Unfilled GDP	CRYO-ME-4Q13-12	868.8	871.2	859.0	861.6	12.7	1.46
	CRYO-ME-4Q13-8	877.7	876.6	867.2	866.8	13.2	1.50
D_2-filled GDP	CRYO-2123-19-04	871.6		861.7		12.9	1.48
Mean±σ						12.9±0.3	1.48±0.03

never exposed to high-pressure DT, unlike the GDP capsules imploded during cryogenic target experiments that showed no contraction.

In addition, a single data point was obtained for a D_2-filled GDP capsule that also exhibited contraction. Although, since D_2 cryogenic target experiments have not been performed on OMEGA for many years, the fact that it contracted the same as the unfilled GDP capsule indicates that it is not mechanical stress from pressurization that causes the cold, DT-filled capsules' OD's to remain close to their room-temperature value.

2. Lack of Contraction of Cold, DT-filled Capsules

Past cryo target data were extracted from the database to compare warm versus cold OD's as a function of fill date, fuel-layer thickness, Characterization Station number, and MCTC number. These data represent 129 different capsules over a time period from 26 August 2014 to 8 December 2015; they are shown in increasing change in OD in Fig. 151.40. The warm OD's (measured by GA) and cold OD's (measured at the Characterization Stations) differ, on average, by 0.06±1.2 μm or 0.01±0.13%. Note that the 3-μm systematic error was not corrected in these data.

The possibility that a step change in measurement accuracy took place at some time in the recent past was explored; these data are shown in Fig. 151.41(a). The data on OD change are also plotted versus Characterization Station number [Fig. 151.41(b)] and MCTC number [Fig. 151.41(c)]. There is no clear trend in any of these data.

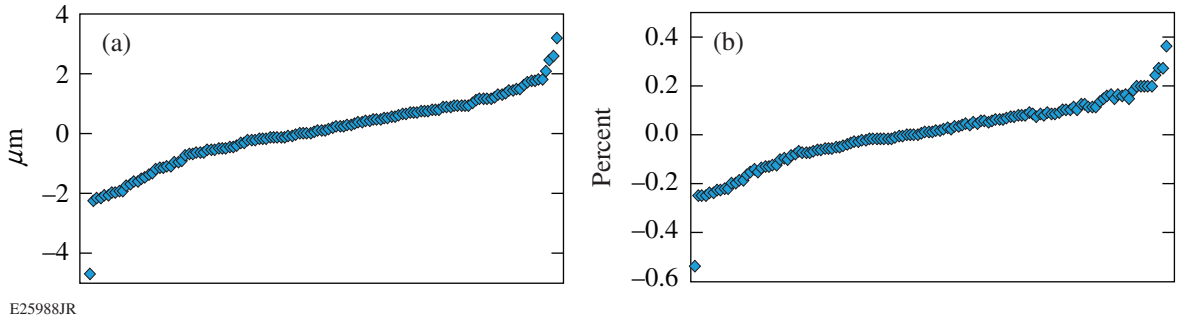

Figure 151.40
LLE's cold OD subtracted from GA's warm OD for 129 capsules, with the order shown in increasing difference: (a) the absolute change and (b) the percentage change. On average, they differ by 0.06±1.2 μm or 0.01±0.13%, respectively.

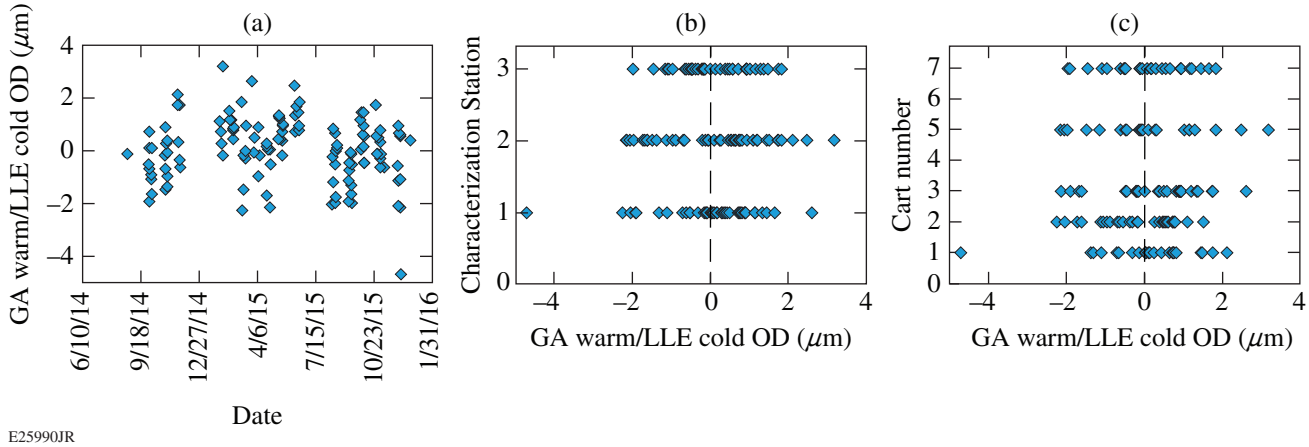

Figure 151.41
Change in outside diameter versus (a) measurement date, (b) Characterization Station number, and (c) MCTC number. There is no clear trend in any of these data; the data are scattered evenly around zero change. MCTC: Moving Cryostat Transfer Cart.

3. Contraction of a Nonpermeation-Filled Capsule

In an unrelated experiment,[7] a single GDP capsule with a 30-μm-diam hole laser-drilled in its wall was included in a permeation fill along with capsules of similar dimensions. Although not the original purpose of that experiment, the data from it can be used to evaluate if mechanical stresses from pressure gradients across the capsule are responsible for the lack of contraction of GDP capsules at cryogenic temperatures. The hole allows the GDP layer to be exposed to the same beta-decay bombardment inside and outside the capsule's wall in addition to that from tritium in solution within the wall, but without the mechanical stresses of the external pressure that enables permeation. The cold diameter was 3 μm less than a typical capsule that was permeation filled in the same batch, but this difference is not statistically significant compared with the range of changes exhibited in the ensemble of capsules shown in Fig. 151.40. A 3-μm-OD change falls within 2.5× the standard deviation from the nearly zero average OD change; if the sample of capsules was normally distributed, 98.8% of the OD-change values would also lie within 2.5 standard deviations from the mean.

Conclusions

The outside diameters of a silicon ball and two GDP capsules were measured while varying the illumination intensity, illumination geometry, focus shift, position of the capsule along the optical axis of the imaging system, position of the capsule laterally in the field of view, the Characterization Station, and MCTC. The greatest effect on OD measurement was illumination intensity, i.e., saturation of the image around the perimeter of the capsule. In addition, if the peak brightness of the illumination does not coincide with the optical axis and capsule center, intensity variations around the perimeter can locally affect where the analysis software determines the capsule's edge. Unsaturated images reproduced the OD measurement even under low illumination. Secondly, focus does have an effect on the OD, but errors are produced only if the image is noticeably out of focus.

A systematic overestimation of the OD was revealed during this study; overall, the Characterization Station–measured OD was greater by ~3 μm than that measured at GA. The capsule data acquired during this study corrected for this offset; however, the historic data collected from our database did *not* correct for this offset since the offset had existed for some unknown time and comparison of historical data must include it. The ~13-μm lack of observed contraction was not a result of measurement error—the systematic error can account for only 3 μm; the remaining effect is real.

The OD's of three GDP capsules that had *not* been exposed to DT were measured at both room temperature and 19 K. After the data were corrected for the 3-μm systematic error, they all contracted by 13 μm, which is 1.5% of their warm OD, as expected. A database comparison of 129 DT-filled capsules revealed that they contracted by an average of 0.06±1.2 μm or 0.01±0.13%. A lack of the ~10-μm anticipated contraction and the overmeasurement of the OD by 2 to 3 μm can explain the up-to-13-μm, larger-than-expected OD's reported by the measurement software.

Radiation damage to the polymer while exposed to beta-particle bombardment during DT permeation[7] explains the lack of contraction. GDP capsules are a highly cross-linked polymer.[8] The average beta-particle energy from tritium decay is 5.7 keV—strong enough to break multiple molecular bonds in the polymer that are a few eV each. Therefore, broken carbon–carbon bonds can readily bond with the ionized hydrogen dissolved in the wall of the capsule. We postulate that the capsules, therefore, swell during permeation to a degree that is nearly compensated for by the contraction during cooling.

Conversely, polystyrene exhibits a high resistance to radiation damage: the polystyrene capsules experience less damage during permeation and contract as expected when cooled, as shown in Table 151.V. Polymers containing aromatic molecules generally are much more resistant to radiation degradation than are aliphatic polymers; this is true whether or not the aromatic group is directly in the chain backbone. Consequently polystyrenes, with a pendant aromatic group, and polyimides, with an aromatic group directly in the polymer backbone, are relatively resistant to high doses of radiation (>4000 kGy) (Refs. 9 and 10).

The GDP capsules containing thicker layers were exposed to DT for a longer period and at a higher concentration during permeation, yet there is no strong correlation of OD change with layer thickness (see Fig. 151.42). There is a possible shift in the median in the data toward less shrinkage as the layer thickness increases, but it is not a convincing trend. This would imply that damage and swelling occur early in the process and conclude quickly.

A DT-gas sample retrieved from the permeation cell following GDP capsule permeation was sent to LLNL to be analyzed with their magnetic-sector mass spectrometer.[11] Many of the constituents in the sample were light hydrocarbons as shown in Fig. 151.43. Since the DT delivery system is constructed of stainless-steel tubing joined by either welded or metal-sealed

Table 151.V: Change in OD after cooling from 293 K to 19 K for a sample of DT-filled polystyrene shells. (The cold OD was reduced by 3 μm from the actual measurement to correct for the systematic error revealed during calibration testing.) The average percent change is 1.11±0.12%, close to the 1.44% thermal contraction calculated from the coefficient of thermal expansion and the temperature change.[12]

Target Number	Outer Diameter (μm)			Warm to Cold (μm, corrected)	Percent Change (corrected)
	Warm	Cold	Cold (corrected)		
CRYO-9079-18	875.0	868.8	865.8	9.2	1.05
CRYO-9083-12	869.0	862.4	859.4	9.6	1.10
CRYO-9089-37	868.0	860.4	857.4	10.6	1.22
CRYO-9088-38	867.0	858.6	855.6	11.4	1.31
CRYO-9089-34	869.0	860.3	857.3	11.7	1.35
CRYO-9116-0021	960.2	952.8	949.8	10.4	1.08
CRYO-9114-0018	962.8	954.0	951.0	11.8	1.23
CRYO-9112-0020	963.4	956.1	953.1	10.3	1.07
CRYO-9107-0023	967.4	959.9	956.9	10.5	1.09
CRYO-9107-0017	967.4	960.7	957.7	9.7	1.00
CRYO-9080-0029	872.0	866.6	863.6	8.4	0.96
CRYO-9080-0034	872.0	865.7	862.7	9.3	1.07
CRYO-9077-0035	878.4	872.4	869.4	9.0	1.02
CRYO-9079-0042	874.8	868.5	865.5	9.3	1.06
CRYO-9080-0041	876.0	870.3	867.3	8.7	0.99
Mean±σ				10.0±1.1	1.11±0.12

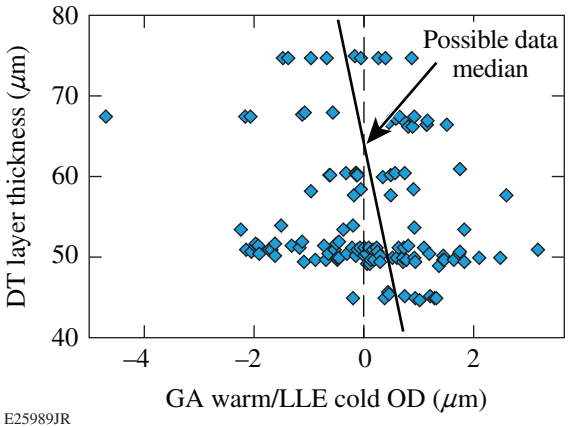

Figure 151.42
Change in outside diameter versus final layer thickness. There is no convincing trend in these data; however, a possible slanting median to the data may indicate less shrinkage with increasing DT exposure.

fittings and the target support is constructed of non-carbon-containing materials (aside from several small polymeric glue joints), total tritiated hydrocarbons in the 1000-ppm range suggest radiation-induced damage to the GDP during permeation, reinforcing the above conclusion regarding swelling prior to contraction during cooling.

ACKNOWLEDGMENT

This material is based upon work supported by the Department of Energy National Nuclear Security Administration under Award Number DE-NA0001944, the University of Rochester, and the New York State Energy Research and Development Authority.

REFERENCES

1. T. C. Sangster, R. Betti, R. S. Craxton, J. A. Delettrez, D. H. Edgell, L. M. Elasky, V. Yu. Glebov, V. N. Goncharov, D. R. Harding, D. Jacobs-Perkins, R. Janezic, R. L. Keck, J. P. Knauer, S. J. Loucks, L. D. Lund, F. J. Marshall, R. L. McCrory, P. W. McKenty, D. D.

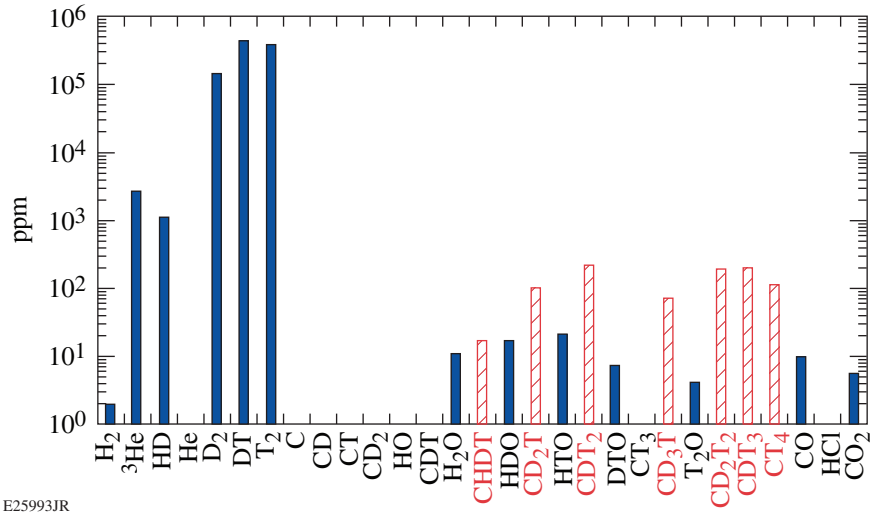

Figure 151.43
A magnetic-sector mass spectrogram of the constituents in a DT-gas sample retrieved from the permeation cell following glow-discharge plasma (GDP) capsule permeation. A significant fraction of the gas is composed of light hydrocarbons (shown in the red crosshatched bars) that have been released from the CH capsule during permeation.

Meyerhofer, P. B. Radha, S. P. Regan, W. Seka, W. T. Shmayda, S. Skupsky, V. A. Smalyuk, J. M. Soures, C. Stoeckl, B. Yaakobi, J. A. Frenje, C. K. Li, R. D. Petrasso, F. H. Séguin, J. D. Moody, J. A. Atherton, B. D. MacGowan, J. D. Kilkenny, T. P. Bernat, and D. S. Montgomery, Phys. Plasmas **14**, 058101 (2007).

2. O. A. Hurricane, D. A. Callahan, D. T. Casey, E. L. Dewald, T. R. Dittrich, T. Döppner, M. A. Barrios Garcia, D. E. Hinkel, L. F. Berzak Hopkins, P. Kervin, J. L. Kline, S. Le Pape, T. Ma, A. G. MacPhee, J. L. Milovich, J. Moody, A. E. Pak, P. K. Patel, H.-S. Park, B. A. Remington, H. F. Robey, J. D. Salmonson, P. T. Springer, R. Tommasini, L. R. Benedetti, J. A. Caggiano, P. Celliers, C. Cerjan, R. Dylla-Spears, D. Edgell, M. J. Edwards, D. Fittinghoff, G. P. Grim, N. Guler, N. Izumi, J. A. Frenje, M. Gatu Johnson, S. Haan, R. Hatarik, H. Herrmann, S. Khan, J. Knauer, B. J. Kozioziemski, A. L. Kritcher, G. Kyrala, S. A. Maclaren, F. E. Merrill, P. Michel, J. Ralph, J. S. Ross, J. R. Rygg, M. B. Schneider, B. K. Spears, K. Widmann, and C. B. Yeamans, Phys. Plasmas **21**, 056314 (2014).

3. B. A. Vermillion *et al.*, Fusion Sci. Technol. **51**, 791 (2007).

4. D. D. Meyerhofer, R. S. Craxton, L. M. Elasky, D. R. Harding, R. L. Keck, M. Pandina, W. Seka, M. D. Wittman, A. Warrick, and T. G. Brown, Bull. Am. Phys. Soc. **48**, 55 (2003).

5. APPLIED IMAGE Inc., Rochester, NY 14609.

6. G. E. Besenbruch *et al.*, in *Inertial Fusion Sciences and Applications 99*, edited by C. Labaune, W. J. Hogan, and K. Tanaka (Elsevier, Paris, 2000), pp. 921–926.

7. D. R. Harding and W. T. Shmayda, Fusion Sci. Technol. **63**, 125 (2013).

8. B. W. McQuillan *et al.*, Fusion Technol. **31**, 381 (1997).

9. Polymer Materials Selection for Radiation-Sterilized Products, Medical Device and Diagnotic Industry, http://www.mddionline.com/article/polymer-materials-selection-radiation-sterilized-products (accessed 3 August 2017).

10. D. A. Badenhorst, presented at the Ninth National Conference of the South African Section of the PRI, Johannesburg, South Africa, 22–23 October 1987 (Paper C18).

11. P. S. Ebey *et al.*, Fusion Sci. Technol. **49**, 859 (2006).

12. CryoComp 5.0 for Windows User Manual, Eckels Engineering Inc., Florence, SC 29501.

Publications and Conference Presentations

Publications

D. H. Barnak, J. R. Davies, R. Betti, M. J. Bonino, E. M. Campbell, V. Yu. Glebov, D. R. Harding, J. P. Knauer, S. P. Regan, A. B. Sefkow, A. J. Harvey-Thompson, K. J. Peterson, D. B. Sinars, S. A. Slutz, M. R. Weis, P.-Y. Chang, "Laser-Driven Magnetized Liner Inertial Fusion on OMEGA," Phys. Plasmas **24**, 056310 (2017) (invited).

E. M. Campbell, V. N. Goncharov, T. C. Sangster, S. P. Regan, P. B. Radha, R. Betti, J. F. Myatt, D. H. Froula, M. J. Rosenberg, I. V. Igumenshchev, W. Seka, A. A. Solodov, A. V. Maximov, J. A. Marozas, T. J. B. Collins, D. Turnbull, F. J. Marshall, A. Shvydky, J. P. Knauer, R. L. McCrory, A. B. Sefkow, M. Hohenberger, P. A. Michel, T. Chapman, L. Masse, C. Goyon, S. Ross, J. W. Bates, M. Karasik, J. Oh, J. Weaver, A. J. Schmitt, K. Obenschain, S. P. Obenschain, S. Reyes, and B. Van Wonterghem, "Laser-Direct-Drive Program: Promise, Challenge, and Path Forward," Matter and Radiation at Extremes **2**, 37 (2017).

J. R. Davies, D. H. Barnak, R. Betti, E. M. Campbell, P.-Y. Chang, A. B. Sefkow, K. J. Peterson, D. B. Sinars, and M. R. Weis, "Laser-Driven Magnetized Liner Inertial Fusion," Phys. Plasmas **24**, 062701 (2017).

Y. H. Ding and S. X. Hu, "First-Principles Equation-of-State Table of Beryllium Based on Density-Functional Theory Calculations," Phys. Plasmas **24**, 062702 (2017).

D. H. Edgell, R. K. Follett, I. V. Igumenshchev, J. F. Myatt, J. G. Shaw, and D. H. Froula, "Mitigation of Cross-Beam Energy Transfer in Symmetric Implosions on OMEGA Using Wavelength Detuning," Phys. Plasmas **24**, 062706 (2017).

R. Epstein, C. Stoeckl, V. N. Goncharov, P. W. McKenty, F. J. Marshall, S. P. Regan, R. Betti, W. Bittle, D. R. Harding, S. X. Hu, I. V. Igumenshchev, D. Jacobs-Perkins, R. T. Janezic, J. H. Kelly, T. Z. Kosc, C. Mileham, S. F. B. Morse, P. B. Radha, B. Rice, T. C. Sangster, M. J. Shoup III, W. T. Shmayda, C. Sorce, J. Ulreich, and M. D. Wittman, "Simulation and Analysis of Time-Gated Monochromatic Radiographs of Cryogenic Implosions on OMEGA," High Energy Density Phys. **23**, 167 (2017).

C. Fagan, M. Sharpe, W. T. Shmayda, and W. U. Schröder, "The Impact of Acid Treatments and Electropolishing Stainless-Steel Surfaces on Tritium Inventories," Fusion Sci. Technol. **71**, 275 (2017).

M. C. Gregor, D. E. Fratanduono, C. A. McCoy, D. N. Polsin, A. Sorce, J. R. Rygg, G. W. Collins, T. Braun, P. M. Celliers, J. H. Eggert, D. D. Meyerhofer, and T. R. Boehly, "Hugoniot and Release Measurements in Diamond Shocked up to 26 Mbar," Phys. Rev. B **95**, 144114 (2017).

S. X. Hu, R. Gao, Y. Ding, L. A. Collins, and J. D. Kress, "First-Principles Equation-of-State Table of Silicon and Its Effects on High-Energy-Density Plasma Simulations," Phys. Rev. E **95**, 043210 (2017).

K. Mehrotra, B. N. Taylor, A. A. Kozlov, S. Papernov, and J. C. Lambropoulos, "Nano-Indentation and Laser-Induced Damage Testing in Optical Multilayer-Dielectric Gratings," Appl. Opt. **56**, 2494 (2017).

D. T. Michel, S. X. Hu, A. K. Davis, V. Yu. Glebov, V. N. Goncharov, I. V. Igumenshchev, P. B. Radha, C. Stoeckl, and D. H. Froula, "Measurement of the Shell Decompression in Direct-Drive Inertial-Confinement-Fusion Implosions," Phys. Rev. E **95**, 051202(R) (2017).

J. F. Myatt, R. K. Follett, J. G. Shaw, D. H. Edgell, D. H. Froula, I. V. Igumenshchev, and V. N. Goncharov, "A Wave-Based Model for Cross-Beam Energy Transfer in Direct-Drive Inertial Confinement Fusion," Phys. Plasmas **24**, 056308 (2017) (invited).

J. B. Oliver, "Impact of a Counter-Rotating Planetary Rotation System on Thin-Film Thickness and Uniformity," Appl. Opt. **56**, 5121 (2017).

T. Petersen, J. D. Zuegel, and J. Bromage, "High-Average-Power, 2-μm Femtosecond Optical Parametric Oscillator Synchronously Pumped by a Thin-Disk, Mode-Locked Laser," Opt. Express **25**, 8840 (2017).

B. S. Rice, J. Ulreich, C. Fella, J. Crippen, P. Fitzsimmons, and A. Nikroo, "Permeation Fill-Tube Design for Inertial Confinement Fusion Target Capsules," High Power Laser Sci.Eng. **5**, e6 (2017).

J. S. Ross, D. P. Higginson, D. Ryutov, F. Fiuza, R. Hatarik, C. M. Huntington, D. H. Kalantar, A. Link, B. B. Pollock, B. A. Remington, H. G. Rinderknecht, G. F. Swadling, D. P. Turnbull, S. Weber, S. Wilks, D. H. Froula, M. J. Rosenberg, T. Morita, Y. Sakawa, H. Takabe, R. P. Drake, C. Kuranz, G. Gregori, J. Meinecke, M. C. Levy, M. Koenig, A. Spitkovsky, R. D. Petrasso, C. K. Li, H. Sio, B. Lahmann, A. B. Zylstra, and H.-S. Park, "Transition from Collisional to Collisionless Regimes in Interpenetrating Plasma Flows on the National Ignition Facility," Phys. Rev. Lett. **118**, 185003 (2017).

J. D. Sadler, M. Sliwa, T. Miller, M. F. Kasim, N. Ratan, L. Ceurvorst, A. Savin, R. Aboushelbaya, P. A. Norreys, D. Haberberger, A. S. Davies, S. Bucht, D. H. Froula, J. Vieira, R. A. Fonseca, L. O. Silva, R. Bingham, K. Glize and R. M. G. M. Trines, "Robustness of Raman Plasma Amplifiers and Their Potential for Attosecond Pulse Generation," High Energy Density Phys. **23**, 212 (2017).

J. D. Sadler, R. M. G. M. Trines, M. Tabak, D. Haberberger, D. H. Froula, A. S. Davies, S. Bucht, L. O. Silva, E. P. Alves, F. Fiúza, L. Ceurvorst, N. Ratan, M. F. Kasim, R. Bingham, and P. A. Norreys, "Optimization of Plasma Amplifiers," Phys. Rev. E **95**, 053211 (2017).

R. B. Spielman, D. H. Froula, G. Brent, E. M. Campbell, D. B. Reisman, M. E. Savage, M. J. Shoup III, W. A. Stygar, and M. L. Wisher, "Conceptual Design of a 15-TW Pulsed-Power Accelerator for High-Energy-Density–Physics Experiments," Matter and Radiation at Extremes **2**, 204 (2017).

C. R. Stillman, P. M. Nilson, S. T. Ivancic, I. E. Golovkin, C. Mileham, I. A. Begishev, and D. H. Froula, "Picosecond Time-Resolved Measurements of Dense Plasma Line Shifts," Phys. Rev. E **95**, 063204 (2017).

G. F. Swadling, J. S. Ross, D. Manha, J. Galbraith, P. Datte, C. Sorce, J. Katz, D. H. Froula, K. Widman, O. S. Jones, L. Divol, O. L. Landen, J. D. Kilkenny, and J. D. Moody, "Initial Experimental Demonstration of the Principles of a Xenon Gas Shield Designed to Protect Optical Components from Soft X-Ray Induced Opacity (Blanking) in High Energy Density Experiments," Phys. Plasmas **24**, 032705 (2017).

P. Tzeferacos, A. Rigby, A. Bott, A. R. Bell, R. Bingham, A. Casner, F. Cattaneo, E. M. Churazov, J. Emig, N. Flocke, F. Fiuza, C. B. Forest, J. Foster, C. Graziani, J. Katz, M. Koenig, C.-K. Li, J. Meinecke, R. Petrasso, H.-S. Park, B. A. Remington, J. S. Ross, D. Ryu, D. Ryutov, K. Weide, T. G. White, B. Reville, F. Miniati, A. A. Schekochihin, D. H. Froula, G. Gregori, and D. Q. Lamb, "Numerical Modeling of Laser-Driven Experiments Aiming to Demonstrate Magnetic Field Amplification via Turbulent Dynamo," Phys. Plasmas **24**, 041404 (2017).

Forthcoming Publications

S. X. Hu, "Continuum Lowering and Fermi-Surface Rising in Strongly Coupled and Degenerate Plasmas," to be published in Physical Review Letters.

A. Jukna, J. Gradauskas, A. Sužiedelis, A. Maneikis, K. Šliužienė, and R. Sobolewski, "Investigation of the I–V Characteristics as Asymmetry in Semiconducting Y-Ba-Cu-O Diodes," to be published in Micro and Nano Letters.

J. M. Ngoko Djiokap, A. V. Meremianin, N. L. Manakov, S. X. Hu, L. B. Madsen, and A. F. Starace, "Kinematical Vortices in Double Photoionization of Helium by Attosecond Pulses," to be published in Physical Review A.

T. Petersen, J. D. Zuegel, and J. Bromage, "Thermal Effects in an Ultrafast BiB_3O_6 Optical Parametric Oscillator at High Average Powers," to be published in Applied Optics.

J. Serafini, A. Hossain, R. B. James, M. Guziewicz, R. Kruszka, W. Słysz, D. Kochanowska, J. Z. Domagala, A. Mycielski, and R. Sobolewski, "Photoconductive and Electro-Optic Effects in (Cd,Mg)Te Single Crystals Measured in an Experiment-on-Chip Configuration," to be published in Applied Physics Letters.

Conference Presentations

L. A. Ceurvorst, N. Ratan, M. F. Kasim, J. Sadler, P. A. Norreys, H. Habara, K. A. Tanaka, S. Zhang, M. S. Wei, S. Ivancic, D. H. Froula, and W. Theobald, "Channeling Optimization of High-Intensity Laser Beams in Millimeter-Scale Plasmas," presented at the 44th IOP Plasma Physics Conference, Oxford, UK, 3–6 April 2017.

A. Shramuk, J. Serafini, and R. Sobolewski, "Superconducting Single-Photon Detectors as Smart Sensors: Photon-Energy and Photon-Number Resolution," presented at the CEIS University Technology Showcase, Rochester, NY, 13 April 2017.

Y. Yiming, R. Shrestha, G. Chen, A. Jukna, and R. Sobolewski, "Optimization Analysis for THz Time-Domain Spectroscopy of Carbon Nanotubes," presented at the Undergraduate Research Expo, Rochester, NY, 21 April 2017.

The following presentations were made at SPIE Optics and Optoelectronics 2017, Prague, Czech Republic, 24–27 April 2017:

Y. Akbas, T. Plecenik, P. Ďurina, A. Plecenik, A. Jukna, G. Wicks, and R. Sobolewski, "Ultra-High Optical Responsivity of Semiconducting Asymmetric Nano-Channel Diodes for Photon Detection."

J. Kitaygorsky, W. Słysz, R. Shouten, S. Dorenbos, E. Reiger, V. Zwiller, and R. Sobolewski, "Amplitude Distributions of Dark Counts and Photon Counts in NbN Super Conducting Single-Photon Detectors Integrated with the HEMT Readout."

W. Lang, B. Aichner, G. Zechner, F. Jausner, A. Klimov, R. Puźniak, W. Słysz, M. Guziewicz, R. Kruszka, M. Węgrzecki, and R. Sobolewski, "Superconducting Order Parameter Fluctuations in NbN/NiCu and NbTiN/NiCu Bilayer Nanostripes for Photon Detection."

J. Serafini, S. Trivedi, D. Kochanowska, M. Witkowska-Baran, A. Mycielski, J. P. Knauer, and R. Sobolewski, "(Cd,Mg)Te and (Cd,Mn)Te Single Crystals for Time-Resolved Detection of X-Ray Photons."

J. D. Zuegel, "100-PW-Class Optical Parametric Chirped-Pulse Amplification: Prospects and Challenges."

The following presentations were made at the Ninth Omega Laser Facility Users Group Workshop, Rochester, NY, 26–28 April 2017:

C. Dorrer, A. Kalb, W. Bittle, J. Bromage, R. Cuffney, E. Hill, and L. Waxer, "The Ultrafast Temporal Diagnostic Upgrade Will Provide Improved On-Target Short-Pulse Shape Predictions on OMEGA EP."

J. Katz, M. Bedzyk, D. H. Edgell, C. Rogoff, M. Sickles, J. Szczepanski, D. Turnbull, D. Wiener, and D. H. Froula, "Characterization of Ultrafast Gated Optical Imagers for the OMEGA Beamlets Diagnostic."

S. F. B. Morse, "Omega Laser Facility OLUG 2017 Update: Progress on Recommendations and Items of General Interest."

S. L. Ramesh and K. L. Marshall, "Characterization of the Electrical Properties of Contaminated Dielectric Oils for Pulsed-Power Research."

A. T. Sorce, J. D. Kendrick, R. Boni, M. C. Gregor, D. N. Polsin, B. Saltzman, B. Henderson, J. Zou, M. Couch, C. M. Rogoff, and T. R. Boehly, "Recent Work to Improve the Omega Laser Facility's VISAR and Streaked Optical Pyrometer Diagnostics."

L. H. Xiao, R. S. Craxton, D. Barnak, and J. Davies, "Simulations of Laser-Driven Magnetized Liner Inertial Fusion."

W. Theobald, "Test Results and Progress of SLOS-TRXI on OMEGA," presented at the CEA-NNSA Joint Diagnostic Meeting, Salives, France, 3–4 May 2017.

The following presentations were made at CLEO 2017, San Jose, CA, 14–19 May 2017:

S.-W. Bahk, C. Dorrer, and J. Bromage, "Two-Dimensional Characterization of Spatiotemporal Coupling of Ultrashort Pulses Based on Chromatic Diversity."

C. Dorrer and J. Hassett, "High-Accuracy, Model-Based Laser Near-Field Beam Shaping."

C. Dorrer, A. Kalb, G. Gibney, A. Sharma, and S.-W. Bahk, "An Apodized-Imaged Hartmann Mask for Quantitative Wavefront Measurements in Laser Systems."

P. B. Radha, "Importance of Validated Equation-of State Models for Direct-Drive Inertial Confinement Fusion Designs," presented at the EOS Workshop, Rochester, NY, 31 May–2 June 2017.

The following presentations were made at the Sixth International Conference on High Energy Density Physics, Shirahama, Japan, 5–9 June 2017:

A. B. Sefkow, "Adventures in ICF and HEDP with Magnetic Fields."

A. B. Sefkow, J. M. Koning, M. R. Gomez, S. B. Hansen, K. Cochrane, C. Thoma, D. R. Welch, and M. M. Marinak, "Unprecedented Stability in Z-Pinch Implosions Due to Magnetic Fields and Plasma Physics."

The following presentations were made at the 47th Annual Anomalous Absorption Conference, Florence, OR, 11–16 June 2017:

S. Bucht, D. Haberberger, J. Bromage, and D. H. Froula, "Transforming the Idler to Seed Raman Amplification."

A. Davies, S. Bucht, J. Katz, D. Haberberger, J. Shaw, D. Turnbull, I. A. Begishev, S.-W. Bahk, J. Bromage, J. D. Zuegel, D. H. Froula, J. Sadler, P. A. Norreys, R. Trines, and R. Bingham, "Picosecond Thermal Dynamics in an Underdense Plasma Measured with Thomson Scattering."

Y. H. Ding and S. X. Hu, "A First-Principles Equation-of-State Table of Beryllium for High-Energy-Density Plasma Simulations."

D. H. Edgell, R. K. Follett, I. V. Igumenshchev, J. F. Myatt, J. G. Shaw, and D. H. Froula, "Three-Dimensional Modeling of Cross-Beam Energy Transfer and Its Mitigation in OMEGA Implosions."

R. K. Follett, D. H. Edgell, D. H. Froula, V. N. Goncharov, I. V. Igumenshchev, J. G. Shaw, and J. F. Myatt, "Comparisons Between Ray- and Wave-Based Calculations of Cross-Beam Energy Transfer."

E. C. Hansen, D. H. Barnak, J. R. Davies, R. Betti, A. B. Sefkow, J. Peebles, V. Yu. Glebov, J. P. Knauer, E. M. Campbell, S. P. Regan, A. Harvery-Thompson, K. J. Peterson, D. B. Sinars, S. A. Slutz, A. Birkel, and C. K. Li, "Experiments and Simulations of Laser-Driven Magnetized Liner Inertial Fusion."

M. J. Rosenberg, A. A. Solodov, W. Seka, J. F. Myatt, P. Michel, S. P. Regan, M. Hohenberger, R. Epstein, A. V. Maximov, T. J. B. Collins, V. N. Goncharov, R. W. Short, D. Turnbull, R. K. Follett, D. H. Froula, P. B. Radha, T. Chapman, J. D. Moody, L. Masse, C. S. Goyon, J. W. Bates, and A. J. Schmitt, "Planar Laser–Plasma Interaction Experiments at Direct-Drive Ignition-Relevant Scale Lengths at the National Ignition Facility."

A. B. Sefkow, "Adventures in ICF and HEDP with Magnetic Fields."

A. B. Sefkow, J. M. Koning, M. R. Gomez, S. B. Hansen, K. Cochrane, C. Thoma, D. R. Welch, and M. M. Marinak, "Unprecedented Stability in Z-Pinch Implosions Due to Magnetic Fields and Plasma Physics."

W. Seka, J. F. Myatt, P. Michel, M. J. Rosenberg, A. A. Solodov, T. Chapman, S. P. Regan, R. W. Short, D. T. Michel, and R. K. Follett, "Observation of Stimulated Raman Scattering and Two-Plasmon–Decay Instabilities on OMEGA and the National Ignition Facility."

R. W. Short, A. V. Maximov, and W. Seka, "Absolute Stimulated Raman Sidescattering in Direct-Drive Irradiation Geometries."

A.A. Solodov, M. J. Rosenberg, J. F. Myatt, W. Seka, R. Epstein, R. W. Short, S. P. Regan, D. H. Froula, P. B. Radha, V. N. Goncharov, J. W. Bates, A. J. Schmitt, P. Michel, M. Hohenberger, T. Chapman, and J. D. Moody, "Hot-Electron

Generation at the Direct-Drive Ignition-Relevant Plasma Conditions at the National Ignition Facility."

D. Turnbull, D. H. Froula, T.J. Kessler, D. Haberberger, J. L. Shaw, A. Davies, S. Bucht, P. Michel, C. Goyon, G. E. Kemp, B. B. Pollock, T. Chapman, D. Mariscal, L. Divol, J. S. Ross, S. Patankar, J. D. Moody, E. Tubman, and N. Woolsey, "Plasma-Based Photonic Devices: Wave Plates, Polarizers, and Amplifiers."

The following presentations were made at the 16th International Superconductive Electronics Conference, Sorrento, Italy, 12–16 June 2017:

J. Kitaygorsky, R. Shouten, S. Dorenbos, E. Reiger, V. Zwiller, W. Słysz, and R. Sobolewski, "Photon-Energy and Photon-Number Resolution Capabilities of NbN Superconducting Single-Photon Detectors."

W. Lang, B. Aichner, G. Zechner, F. Jausner, R. Puzniak, A. Klimov, W. Słysz, M. Guziewicz, R. Kruszka, M. Wegrzecki, and R. Sobolewski, "Superconducting Fluctuations and Magnetic Properties of NbN/NiCu and NbTiN/NiCu Bilayer Nanostructures for Photon Detection."

C. R. Stillman, P. M. Nilson, S. T. Ivancic, I. E. Golovkin, C. Mileham, I. A. Begishev, and D. H. Froula, "Picosecond Time-Resolved Observations of Dense Plasma Shifts," presented at the Stewardship Science Graduate Fellowship Program Review, Albuquerque, NM, 18–23 June 2017.

S.-W. Bahk, C. Dorrer, and J. Bromage, "Two-Dimensional Single-Shot Characterization of Spatiotemporal Coupling of Ultrashort Pulses Using Chromatic Diversity," presented at OSA Imaging and Applied Optics Congress, San Francisco, CA, 26–29 June 2017.

J. F. Myatt, R. K. Follett, J. G. Shaw, A. A. Solodov, I. V. Igumenshchev, V. N. Goncharov, D. H. Edgell, D. H. Froula, T. J. Kessler, W. Seka, R. Betti, T. R. Boehly, M. J. Bonino, E. M. Campbell, T. J. B. Collins, R. S. Craxton, A. K. Davis, J. A. Delettrez, R. Epstein, C. J. Forrest, V. Yu. Glebov, D. R. Harding, S. X. Hu, R. T. Janezic, J. H. Kelly, T. Z. Kosc, S. J. Loucks, J. A. Marozas, F. J. Marshall, R. L. McCrory, P. W. McKenty, D. T. Michel, P. B. Radha, M. Rosenberg, W. T. Shmayda, A. Shvydky, S. Skupsky, C. Stoeckl, W. Theobald, F. Weilacher, B. Yaakobi, P. Michel, T. Chapman, L. Masse, C. S. Goyon, J. E. Ralph, J. D. Moody, M. A. Barrios, O. A. Hurricane, M. Hohenberger, M. M. Marinak, R. Nora, M. Tabak, J. Bates, J. Weaver, M. Karasik, A. J. Schmitt, S. P. Obenschain, J. Hund, N Petta, M. Farrell, M Schoff, A. Greenwood, M. Schmitt, and R. Shah, "The Scaling of Laser–Plasma Instabilities in Direct-Drive Inertial Confinement Fusion from OMEGA to the National Ignition Facility," presented at the 44th EPS Conference on Plasma Physics, Belfast, Northern Ireland, 26–30 June 2017.


1850
MELIORA
UNIVERSITY of
ROCHESTER